

AD-A146 420

PULSED ELECTRIC DISCHARGE LASER TECHNOLOGY ELECTRON  
BEAM WINDOW FOIL MATE. (U) AVCO EVERETT RESEARCH LAB  
INC EVERETT MA M W MCGEOCH ET AL. JAN 84

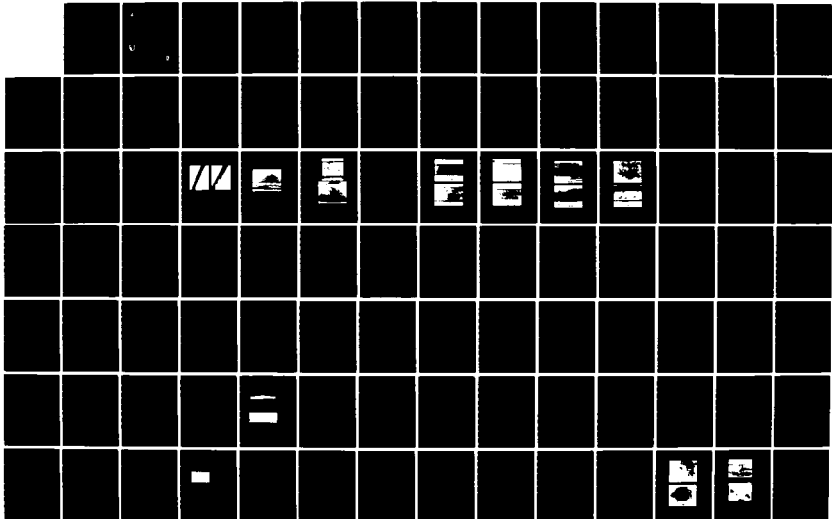
1/2

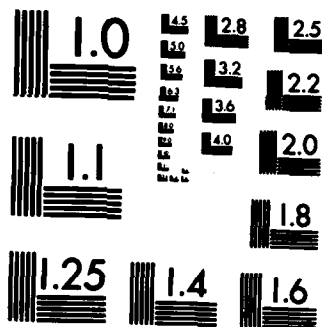
UNCLASSIFIED

DRSMI/RH-CR-84-13 DAAH01-82-D-A013

F/G 20/5

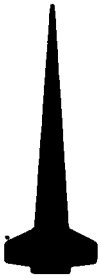
NL





COPY RESOLUTION TEST CHART

AD-A146 420



TECHNICAL REPORT RH-CR-84-13



**PULSED ELECTRIC DISCHARGE LASER TECHNOLOGY -  
ELECTRON BEAM WINDOW FOIL MATERIAL**

Malcolm W. McGeoch  
Anthony J. DeFuria  
Charles T. Pike  
Avco Everett Research Laboratory, Inc.  
2385 Revere Beach Parkway  
Everett, MA 02149

Prepared for:  
Directed Energy Directorate  
US Army Missile Laboratory  
US Army Missile Command  
Redstone Arsenal, AL 35898

JANUARY 1984



**U.S. ARMY MISSILE COMMAND**

*Redstone Arsenal, Alabama 35898*

Cleared for public release; distribution is unlimited.

DTIC FILE COPY

**DTIC**  
**ELECTE**  
OCT 03 1984  
**S** **D**  
**E**

84: 10: 02 072

#### **DISPOSITION INSTRUCTIONS**

**WHEN THIS REPORT IS NO LONGER NEEDED, DEPARTMENT OF THE ARMY ORGANIZATIONS WILL DESTROY IT IN ACCORDANCE WITH THE PROCEDURES GIVEN IN AR 380-5.**

#### **DISCLAIMER**

**THE FINDINGS IN THIS REPORT ARE NOT TO BE CONSTRUED AS AN OFFICIAL DEPARTMENT OF THE ARMY POSITION UNLESS SO DESIGNATED BY OTHER AUTHORIZED DOCUMENTS.**

#### **TRADE NAMES**

**USE OF TRADE NAMES OR MANUFACTURERS IN THIS REPORT DOES NOT CONSTITUTE AN OFFICIAL INDORSEMENT OR APPROVAL OF THE USE OF SUCH COMMERCIAL HARDWARE OR SOFTWARE.**

**PULSED ELECTRIC DISCHARGE LASER TECHNOLOGY –  
ELECTRON BEAM WINDOW FOIL MATERIAL**

**Malcolm W. McGeoch  
Anthony J. DeFuria  
Charles T. Pike**

**AVCO EVERETT RESEARCH LABORATORY, INC.  
2385 Revere Beach Parkway  
a Subsidiary of Avco Corporation  
Everett, MA 02149**

**January 15, 1984  
Final Report for Period January 28, 1983 – January 15, 1984**

**DISTRIBUTION UNLIMITED.**

**Prepared for  
U.S. ARMY MISSILE COMMAND  
Redstone Arsenal, AL 35898**



Accession For	
NTIS GRA&I	<input checked="" type="checkbox"/>
DTIC TAB	<input type="checkbox"/>
Unannounced	<input type="checkbox"/>
Justification	
By _____	
Distribution/	
Availability Codes	
Dist	Avail and/or Special
<b>A-1</b>	



UNCLASSIFIED

SECURITY CLASSIFICATION OF THIS PAGE(When Data Entered)

(20)

foil fatigue under these conditions is documented. The stresses in pressure-loaded foil windows were calculated by the finite element method, both for static and dynamic loading. The shape of the foil support rib was optimized to minimize the foil stresses. A correlation was performed between the computed stress cycling under pulsed loading and the measured fatigue strength in uniaxial tension. As a check on the pulse simulation, the actual movement of an electron-beam foil window was measured by interferometry. A speckle interferometer which allows measurement of the movement of unpolished foil surfaces is described.

UNCLASSIFIED

SECURITY CLASSIFICATION OF THIS PAGE(When Data Entered)

## TABLE OF CONTENTS

<u>Section</u>		<u>Page</u>
	List of Illustrations	3
	List of Tables	7
1.0	INTRODUCTION	8
2.0	FOIL PROPERTIES	10
	2.1 Selection of Ti Alloys	10
	2.2 Tensile Tests on Foil Material	12
	2.3 Fatigue Tests on Foil Material	19
	2.4 Crystal Structure of Foil Materials	19
3.0	MODELING OF STRESS DISTRIBUTION IN LOADED FOIL WINDOWS	34
	3.1 Introduction	34
	3.2 Use of the NASTRAN Structural Code	34
	3.3 Elastic Foil Stress Results	41
	3.4 Deformable Foil Stress Results	51
	3.5 Dynamic Response of Foils to Laser Pressure Pulse	57
4.0	BIAXIAL STRENGTH OF FOILS	64
	4.1 Definition of Biaxial Loading	64
	4.2 Burst Test and Results	66
	4.3 Modeling of Burst Test Using Uniaxial Strength	70
	4.4 Tentative Design Method	74
5.0	CYCLIC PRESSURE SIMULATION	75
	5.1 Introduction	75
	5.2 Design of Pressure Pulse Rig	76
	5.3 Performance of Pressure Pulse Rig	79
	5.4 Foil Tests on the Cyclic Pressure Rig	87
6.0	INTERFEROMETRIC MEASUREMENT OF FOIL MOVEMENT	97

<u>Section</u>		<u>Page</u>
7.0	SINGLE PULSE MEASUREMENT OF FOIL MOTION	102
	7.1 Introduction	102
	7.2 Experimental Arrangement	102
	7.3 Measurements of Foil Movement	105
	7.4 Calculation of Foil Movement	107
	7.5 Conclusion	109
8.0	SUMMARY	110

## LIST OF ILLUSTRATIONS

<u>Figure</u>		<u>Page</u>
1	Drawing for tensile and fatigue test coupons	13
2	Typical stress-strain records for (a) CP Ti(4), (b) Ti 3-2.5, (c) Ti 15-3-3-3 as rolled and strand annealed, (d) Ti 15-3-3-3 aged 800°F, 8 hrs	18
3	High cycle axial fatigue data for Ti 15-3-3-3 as rolled, and aged 1000°F, 8 hr	21
4	High cycle axial fatigue data for Ti 3-2.5 at 75°F, and 600°F	22
5	High cycle axial fatigue data for Ti 15-3-3-3, aged 800°F, 8 hrs at 75°F and 600°F	23
6	Scanning electron micrographs of CP Ti(4), 0.5 mil and 1 mil foils	25
7	Scanning electron micrograph of Ti 3-2.5, 0.6 mil foil	26
8	Scanning electron micrographs of Ti 15-3-3-3, 0.65 mil foil, as rolled and strand annealed: (a) grain structure in polished section (b) fracture surface of the same material	27
9	Scanning electron micrographs of Ti 15-3-3-3, 0.65 mil foil (a) aged 800°F, 4 hr and (b) aged 800°F, 8 hr	29
10	Scanning electron micrographs of Ti 15-3-3-3, 0.65 mil foil (a) aged 900°F, 1 hr. and (b) aged 900°F, 4 hrs	30
11	Scanning electron micrographs of Ti 15-3-3-3, 0.65 mil foil (a) aged 1000°F, 1 hr and (b) 1000°F, 4 hrs	31
12	Scanning electron micrographs of Ti 15-3-3-3, 0.65 mil foil aged 1000°F, 4 hrs: (a) magnification increased and (b) fracture surface	32
13	Schematic of foil movement constraints in model	36
14	Material options in NASTRAN	37
15	Plastic deformation model in NASTRAN	38

<u>Figure</u>		<u>Page</u>
16	Detail of foil beam model for the case of a circular rib profile, 0.5 cm rib spacing and 0.3 cm slot	40
17	Generic foil support rib contours	42
18	Stress distribution in 0.5 mil elastic Ti foil at 7 atm	43
19	Stress distribution in 0.5 mil elastic Ti foil at 7 atm	44
20	Distribution of peak stress in 0.5 mil elastic Ti foil at 5 atm	46
21	Distribution of peak stress in 1.0 mil elastic Ti foil at 5 atm	47
22	Peak stress as a function of ellipticity, showing optimum rib profile for 0.5 mil and 1.0 mil elastic Ti foils loaded to 5 atm	48
23	Peak stress at rib and midspan as a function of loading for 0.5 mil elastic Ti foil, 0.2 cm rib, 0.5 cm slot, and rib ellipticity 6	49
24	Peak stress at rib and midspan as a function of loading for 0.5 mil elastic Ti foil, 0.2 cm rib, 0.5 cm slot, and rib ellipticity 10	50
25	Peak deflection as a function of loading for 0.5 mil elastic Ti foil, 0.2 cm 6:1 ellipse rib, 0.3 cm slot	52
26	Stress-strain curve assumed for deformable material example	53
27	Peak stress as a function of loading for 0.5 mil deformable Ti example	54
28	Peak stress on first and second loading cycles for 0.5 mil deformable Ti example	56
29	Qualitative view of pressure history in a pulsed laser	58
30	Dynamic response of 0.5 mil elastic Ti foil to 1 $\mu$ sec, 1 atm pressure jump, 0.3 cm slot	60
31	Peak stresses relating to the dynamic response of Figure 30	61
32	Dynamic response of 0.5 mil elastic Ti foil to 12 $\mu$ sec, 2 atm pressure jump, 0.3 cm slot	62
33	Illustration of uniaxial and biaxial stresses	65

<u>Figure</u>		<u>Page</u>
34	Plan showing test frame slot geometries: (a) 0.3 cm slot, (b) 0.5 cm slot	67
35	Comparison of measured and ideal rib contours for (a) 6:1 ellipse, 0.3 cm slot frame, and (b) radiussed flat, 0.3 cm slot frame	68
36	Computed stresses using measured properties of 0.6 mil Ti 3-2.5, 0.3 cm slot, rib ellipticity 6	71
37	Vertical section of cyclic test rig	77
38	Horizontal section of cyclic test rig	78
39	Circuit of cyclic test rig modulator	80
40	Current and voltage waveforms on test rig	81
41	Measured foil displacement as a function of current	82
42	Measured foil displacement as a function of time, 0.3 cm slot	84
43	Measured foil displacement as a function of time, 0.5 cm slot	85
44	Foil displacement as a function of pulse repetition frequency	86
45	Scanning electron micrograph of a typical fatigue spot: (a) pressure side, (b) rib side, showing alumina particles	89
46	(a) Fatigue-induced crack on one of the two probable stress-corrosion cases, showing feather-like growth	90
47	Position of the crack in Figure 46 relative to the rib edges, which show corrosion lines	92
48	Goodman plot of test data on 0.65 mil, as-rolled Ti 15-3-3-3, showing the biaxial strength enhancement applied to measured properties	95
49	Schematic of interferometer	98
50	Illustration of curvature and tilt matching in the interferometer	100
51	Initial part of interferometer output used to plot Figure 43, showing the first quarter cycle	101

<u>Figure</u>		<u>Page</u>
52	Schematic of electron gun used in single pulse experiment	103
53	Illustration of single pulse pumping geometry, showing blocked regions	104
54	Optical path layout for single pulse experiment	106
55	Measured and calculated foil peak-to-peak movement for 75 psi Ne single pulse experiment	108

LIST OF TABLES

<u>Table</u>		<u>Page</u>
1	Bulk Properties of Ti Alloys	11
2	75°F Tensile Properties of Ti Foil Samples	15
3	600°F Tensile Properties of Ti Foil Samples	16
4	Foil Material Properties	17
5	Matrix of Fatigue Tests	20
6	Burst Pressures and Biaxial Strength Enhancement	69
7	Cyclic Pressure Tests on 6:1 Ellipse, 0.3 cm Slot, Frame	88
8	Cyclic Pressure Tests on 6:1 Ellipse, 0.5 cm Slot, Frame	93

## 1.0 INTRODUCTION

The electron-beam window in electron-beam-pumped excimer lasers is a critical component that has to be thin ( $< 1 \times 10^{-3}$  inch) to transmit the electron beam, and strong enough to support static pressures of up to  $\sim 100$  psi relative to the vacuum of the electron gun. In addition, the window foil must withstand the repetitive pressure pulse caused by heating of the laser gas, and simultaneously, the rapid heating caused by the passage of the electron beam. Such a demanding list of requirements eliminates all but Ti alloy foils from practical consideration.

In the present program, we have measured the mechanical strength of Ti foils and correlated this with the foil performance under simulated laser load cycling. The objective has been to develop an accurate method for the mechanical design of foil windows. In the course of this work, we have made a number of surprising observations on the strength of rolled Ti foils compared to bulk material strength, and shown that, indeed, the optimized performance of foil windows is far in excess of previous expectations.

The present report begins with a description of the choice of Ti alloy foils, the measurement of their tensile and fatigue strengths and the examination of their crystal structure. In the first approximation, these results should be used, in conjunction with stress calculations, to predict foil performance in the laser application. The details of such calculations are presented in Section 3.0. However, a static burst test that measured the membrane, or biaxial, foil strength showed a discrepancy with the predicted burst strength. This is discussed in Section 4.0, along with an analysis of the biaxial strength enhancement. Section 4.0 concludes with a tentative prescription for foil design, as a basis for comparison with the subsequent experiments.

Section 5.0 describes the design and operation of a laser pressure cycle simulator that was used to test foil performance. The movement of foils on this rig was measured in real time using a novel interferometer, which is described in Section 6.0.

The measurement of foil movement in real laser conditions is described in Section 7.0, and the results compared with theoretical expectation.

Conclusions are drawn in Section 8.0 regarding the status of foil mechanical design at the end of this program. Recommendations are made for future work.

## 2.0 FOIL PROPERTIES

### 2.1 SELECTION OF Ti ALLOYS

Because repetitive laser pulsing leads to substantial heat loads in the foil ( $10 > 100 \text{ W cm}^{-2}$ ), the foil typically operates at a temperature well above ambient and, depending on the method chosen for cooling the foil, may operate between  $100^\circ\text{C}$  and  $400^\circ\text{C}$  ( $200^\circ\text{F}$  to  $750^\circ\text{F}$ ). Ideally, we would select a high-strength, high-temperature Ti alloy. However, the very structures that are needed - stable ( $\alpha + \beta$ ) phase alloys such as Ti 6-4 (6% Al, 4% V) are those that are most difficult to cold roll.

In order to cover the broadest range of Ti properties a short list of alloys was drawn up (Table 1). Of these, it was found impossible to obtain Ti 6-4 in  $< 1$  mil thickness, at least without entering an open-ended development contract. The possibility of rolling  $< 1$  mil Ti 6-4 had been demonstrated in previous work,<sup>(1)</sup> but difficulties had been encountered which made further work with this alloy for large-area foils appear relatively unattractive. The first entry in Table 1 is an example of a single-phase ( $\alpha$ ) alloy, containing 0.4 percent oxygen. Its high temperature strength is low because it does not contain an interlocking  $\beta$  structure to stabilize the grain boundaries. However, it is not difficult to cold roll to 0.5 mil in large areas, pinhole-free. The second entry in Table 1 is an example of a widely used intermediate strength alloy, containing 3 percent Al + 2.5 percent V. It, too, is readily rolled to 0.5 mil.

The last item in Table 1 is different<sup>(2)</sup> in that its high Vanadium content stabilizes the  $\beta$  phase as the alloy is cooled from  $1400^\circ\text{F}$ , its " $\beta$  transus temperature," so that the alloy is almost pure  $\beta$  phase at room temperature. In the  $\beta$  phase, it can be rolled at room temperature in good-quality, large-area strips (up to 14 in. wide at least), down to 0.5 mil thickness. Reductions of up to 40 percent per pass are used, down to the smallest

1. Private communication, Hamilton Precision, Inc.
2. H. W. Rosenberg, review article in *Journal of Metals*, Nov. 1983.

TABLE 1. BULK PROPERTIES OF Ti ALLOYS

Alloy and Main Alloy Additions (WT.PCT.)	Tensile Strength (k.s.i.)				Remarks
	R.T.	400°F	600°F	800°F	
CP Ti Grade 4 0.4 Oxygen	80	-	44	34	Corrosion Resistant Ti, Pure Alpha
Ti-3-2.5 3 Al-2.5V	90	-	65	55	Alpha + Beta Alloy Moderate Strength Easy to Form
Ti-6-4 6 Al-4V	130	-	100	90	Alpha + Beta. The Most Commonly Used Alloy For Low and Moderate Temps. Difficult to Roll
Ti-15-3-3-3 15V-3Cr-3Sn-3Al	165	153	144	-	Near Beta Alloy. Readily Rolled. Aged After Rolling To Develop Full Strength

thickness.<sup>(3)</sup> In order to develop the full alloy strength, Ti 15-3-3-3 may be "aged" at intermediate temperatures (800°F to 1000°F) so that an  $\alpha$  phase precipitates within the material. Once aged, the material strength is higher than during rolling, and subsequent rolling is not possible unless the material is 'reset' to the  $\beta$  phase by rapid cooling from 1400°F. A consequence of the  $\beta$  metastability of Ti 15-3-3-3 is that it is essentially a low-temperature alloy (< 800°F) on account of its aging behavior above this temperature. However, its temperature range is adequate for the laser application.

Foils procured for the purpose of testing are listed below:

<u>Alloy</u>	<u>Nominal mils Thicknesses</u>	<u>Ribbon Width</u>
CP Ti (4)	0.5, 1.0	6 in.
Ti-3-2.5	0.5, 1.0	6 in.
Ti-15-3-3-3	0.6, 0.75	14 in.

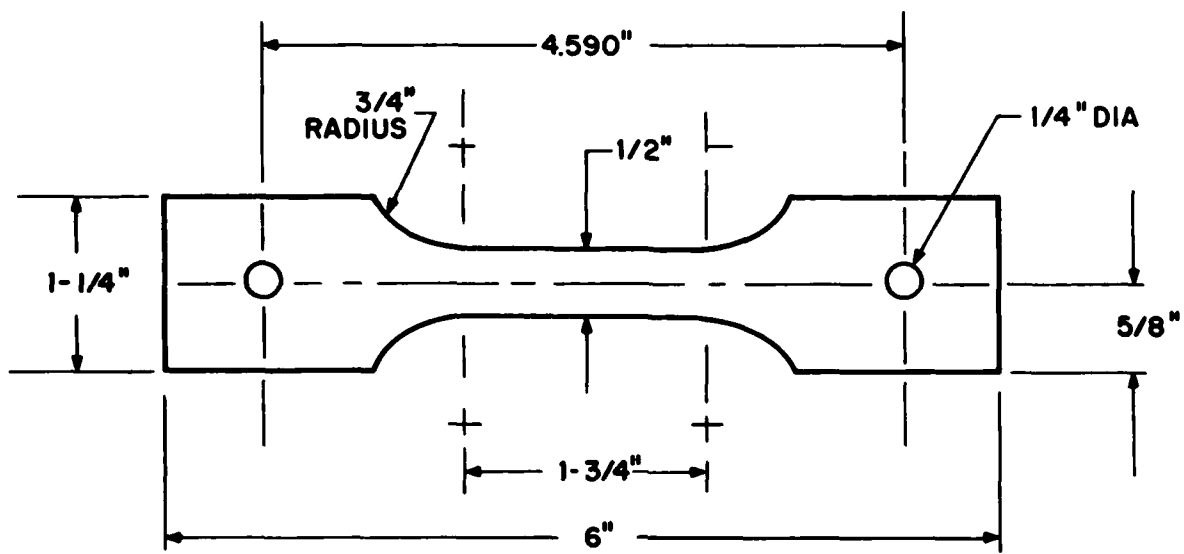
The condition of the Ti 15-3-3-3 was "as rolled and strand-annealed" referring to the practice of passing the foil through an oven at > 1400°F for < 3 min on the final rolling pass. All foils were procured from Arnold Engineering.

## 2.2 TENSILE TESTS ON FOIL MATERIAL

The testing of < 1 mil metal foils is a specialized business that we assigned to Metcut Research Associates, Inc., of Cincinnati, Ohio, because of their prior experience and their ability to perform 600°F tensile and fatigue testing of foils under good vacuum. It was considered necessary to have < 10<sup>-5</sup> torr conditions, particularly for the high-cycle fatigue testing, which could take up to four days per sample, risking oxidation in a normal atmosphere or in a contaminated argon buffer.

Test coupons were identical for both tensile and fatigue testing, and conformed to the dimensions shown in Figure 1. The coupons were prepared in a stack, sandwiched between 1/4 in. plates, which was ground to the correct

3. Private communication, Arnold Engineering, Inc.



L2708

Figure 1. Drawing for tensile and fatigue test coupons.

contour. Typically, 50 to 100 samples were prepared simultaneously in a stack. After grinding, the edges of the stack were polished with a series of papers (240, 400, 600) to give a high polish, following standard practice on 1/4 in. bar fatigue samples. During preparation and testing, the foil samples were handled with rubber gloves and cleaned when necessary with acetone. This precaution was taken to avoid sodium or hydrocarbon contamination, which could have influenced foil fatigue performance.

Initial testing was with samples cut parallel and perpendicular to the rolling direction (longitudinal or transverse), but no significant difference was obtained in the two tensile strengths and subsequent work was with a mixture of longitudinal and transverse specimens.

The tensile tests were performed on a closed-loop, servo-controlled hydraulic system of 20,000 lb capacity (LCF No. 26-2), which applied strain at the rate of 0.005 in/in/min. For each specimen the stress-strain curve was recorded, and was analyzed to give the 0.2 percent Yield Strength (YS) and the Ultimate Tensile Strength (UTS). After fracture, the foil pieces were placed together to obtain an estimate of the elongation. Because of foil puckering, this elongation estimate was not very reliable, but the results are quoted in order to show the extent of ductility reduction in foils.

Tests were performed at 75°F and 600°F. The high temperatures were obtained by RF induction heating of the foil ribbon samples. Temperatures were measured by thermocouple probe in contact with reference foils. It was found necessary to employ an extremely fine (12  $\mu$ m diameter) chromel alumel probe wire in order not to perturb the foil temperature at the point of probe contact.

The test data at 75°F is summarized in Table 2, in which the standard errors refer to the mean of three tests for each material. The 600°F data is presented in Table 3. The comparison between data at different temperatures and bulk material data is shown in Table 4.

Examples of the stress-strain curves are shown in Figure 2. In this figure, the 0.2 percent yield line is drawn parallel to the initial slope. As may be seen from the abrupt termination of some of these curves, the foil ductility is generally very low.

The elastic modulus, E, of the foil material is also presented in Tables 2 and 3. The moduli are in agreement with bulk material measurements at 75°F, apart from Ti 15-3-3-3 aged at 800°F for 8 hours, which has ~ 25 percent higher modulus than expected.

TABLE 2. 75°F TENSILE PROPERTIES OF Ti FOIL SAMPLES

Material	Thickness (10 <sup>-3</sup> inch)	Ultimate Tensile Strength (UTS) (k.s.i.)	Yield Strength 0.2 (Y.S.) (k.s.i)	Elastic Modulus E (10 <sup>6</sup> psi)	Elongation (Percent)
CPTi(4)1	1.0	148±1	142±1	15.8	1.0±1.0
Ti 3-25	0.60	142±1	132±1.4	12.4	2.9±0.3
Ti 15-3-3-3 As rolled and strand annealed	0.65	113±4	111±3	11.6	1.3±0.4
Ti 15-3-3-3 Aged 1000°F 8 hr	0.65	192±3	185±1.5	14.8	1.1±0.4
Ti 15-3-3-3 Aged 800°F 8 hr	0.65	194±7	194±7	20.4	1.5±1.4

TABLE 3. 600°F TENSILE PROPERTIES OF Ti FOIL SAMPLES

Material	Thickness (10 <sup>-3</sup> inch)	Ultimate (UTS) (ksi)	Yield Strength 0.2 (YS) (ksi)	Elastic Modulus E (10 <sup>6</sup> psi)	Elongation (Percent)
CPTi(4)1	1.0	66±2	65±1.5	10.3	1.9±1.1
Ti 3-2.5	0.60	93±6	86±6	9.6	6.0±1.4
Ti 15-3 As Rolled	0.65	96.5±0.6	89.6±2.2	10.2	0.2±0.2
Ti 15-3 Aged 1000°F 8 hr	0.65	153.2±2.1	143.9±1.4	14.4	0.5±0.4
Ti 15-3 Aged 800°F 8 hr	0.65	183±3	175±2	14.9	1.1±0.5

TABLE 4. FOIL MATERIAL PROPERTIES

Specimen Thicknesses 0.5 mil to 1.0 mil

Test Geometry 0.5 Inch Ribbon with Polished Edges

Material		Bulk Material U.T.S. (ksi)	Foil U.T.S. (ksi)	Foil 0.2 Y.S. (ksi)	Foil 10 <sup>7</sup> Cycle Fatigue* (ksi)
C.P. Ti(4)	75°F	80	148	142	-
	600°F	44	66	65	-
Ti 3-2.5	75°F	90	143	132	58
	600°F	65	93	86	50
Ti 15-3-3-3 As Rolled (Strand Annealed)	75°F	115	113	111	55
	600°F	92	96	90	-
Ti 15-3-3-3 Aged 1000°F, 8 Hr.	75°F	165	192	185	80
	600°F	144	153	144	-
Ti 15-3-3-3 Aged 800°F, 8 Hr.	75°F	180	194	194	113
	600°F	-	183	175	60

\*30 Hz Sinusoidal Load Peak: Min = 10:1

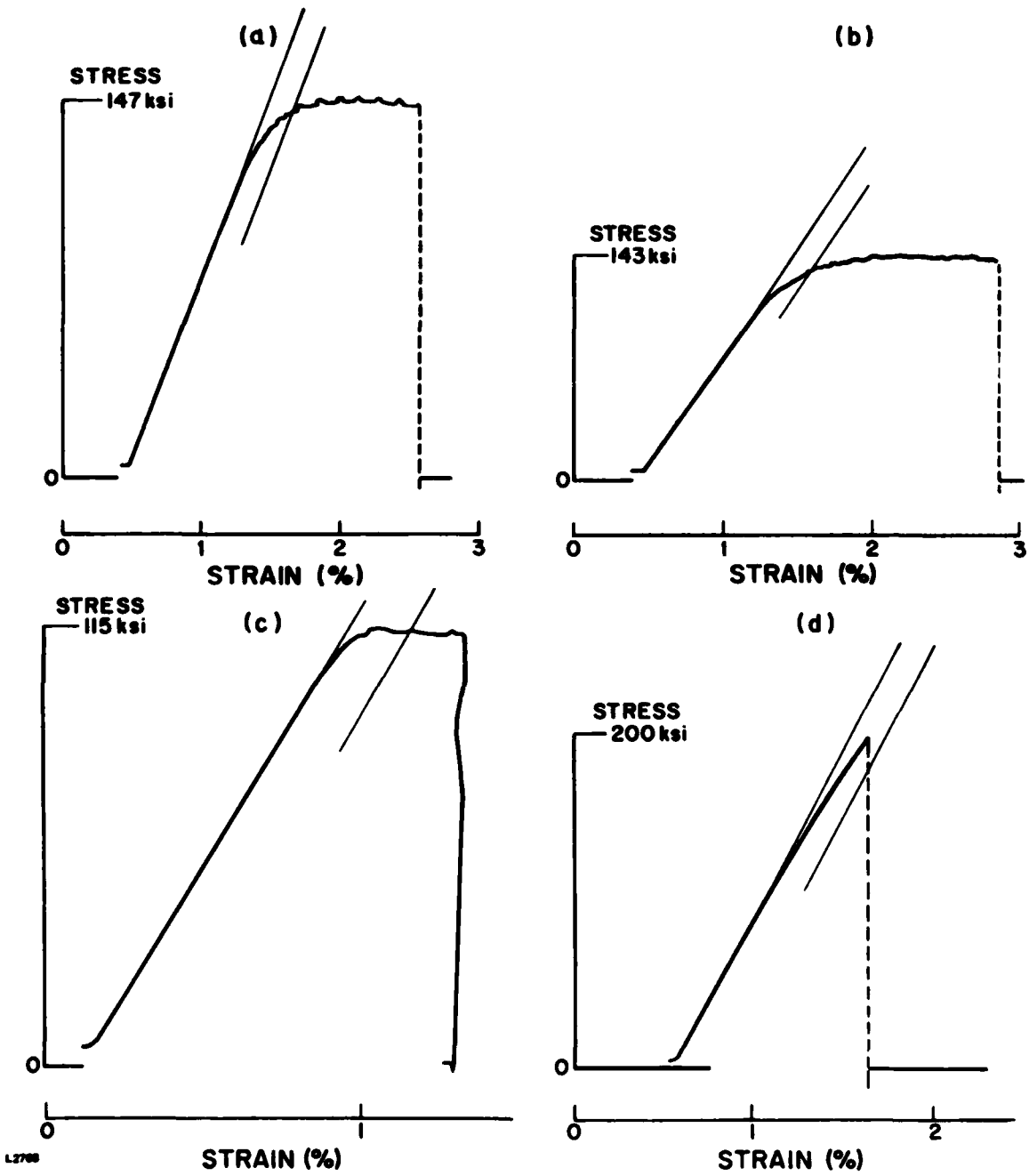


Figure 2. Typical stress-strain records for (a) CP Ti(4), (b) Ti 3-2.5, (c) Ti 15-3-3-3 as rolled and strand annealed, (d) Ti 15-3-3-3 aged 800°F, 8 hrs.

## 2.3 FATIGUE TESTS ON FOIL MATERIAL

Foil samples prepared in coupons as described in the previous section were submitted to high-cycle axial fatigue testing, at both 75°F and 600°F. The test conditions were:

Frequency:	30 Hz
Waveform:	Sinusoidal
Machine:	Closed-loop, servo-controlled hydraulic system, 20,000 lb capacity (LCF no. 26-2)
"A" Ratio:	0.81 (ratio of cyclic stress amplitude to average stress)
Vacuum:	$< 1 \times 10^{-5}$ torr for 600°F data
Runout:	$10^7$ cycles
"R" Value:	0.1 (ratio of minimum stress to maximum stress)

Because of time and cost limitations, each fatigue curve was generated from six points only. In some cases, the curves were regular, but in other cases it would have been more desirable to have twice as many points. The matrix of fatigue tests is shown in Table 5.

The test points are plotted in Figures 3, 4 and 5, in which qualitative lower bounds have been drawn. As anticipated for Ti, the loss of strength is greatest below  $10^4$  cycles. In the case of Ti 15-3-3-3 aged 800°F, 8 hr. (Figure 3), the room temperature data follows a very flat curve between  $10^4$  and  $10^7$  cycles. However, there is an unusual behavior in the 600°F test for this material, probably due to the effect of ageing during the fatigue test.

In general the  $10^7$  cycle strength is between 40 and 50 percent of the U.T.S. although, in the 75°F case of Ti 15-3-3-3 aged 800°F, 8 hr. it is 56 percent. This ratio is very similar to that for bulk material.<sup>(4)</sup>

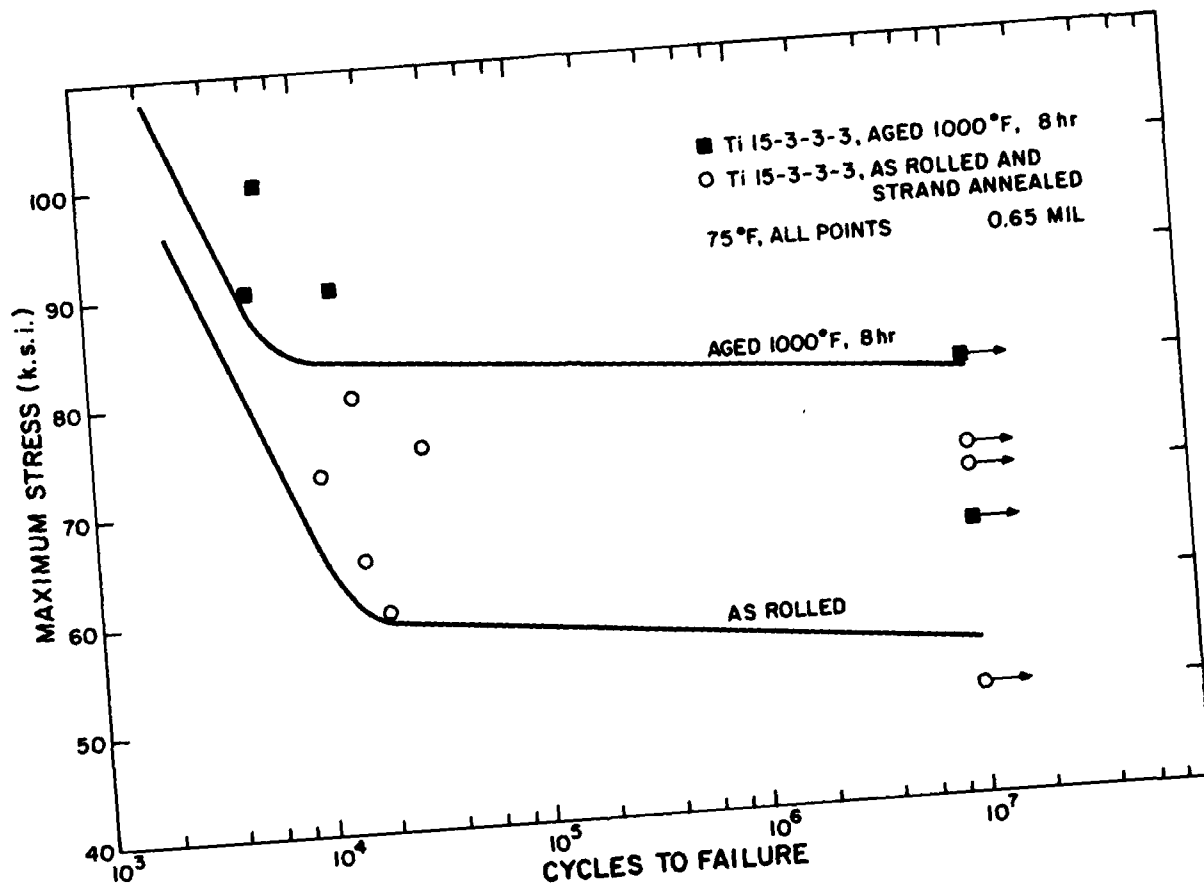
## 2.4 CRYSTAL STRUCTURE OF FOIL MATERIALS

The size and disposition of  $\alpha$  and  $\beta$  grains within the foil materials were determined by Scanning Electron Microscopy of polished and etched samples.

4. "Cold Formable Ti Sheet," Report AFWAL-TR-82-4174.

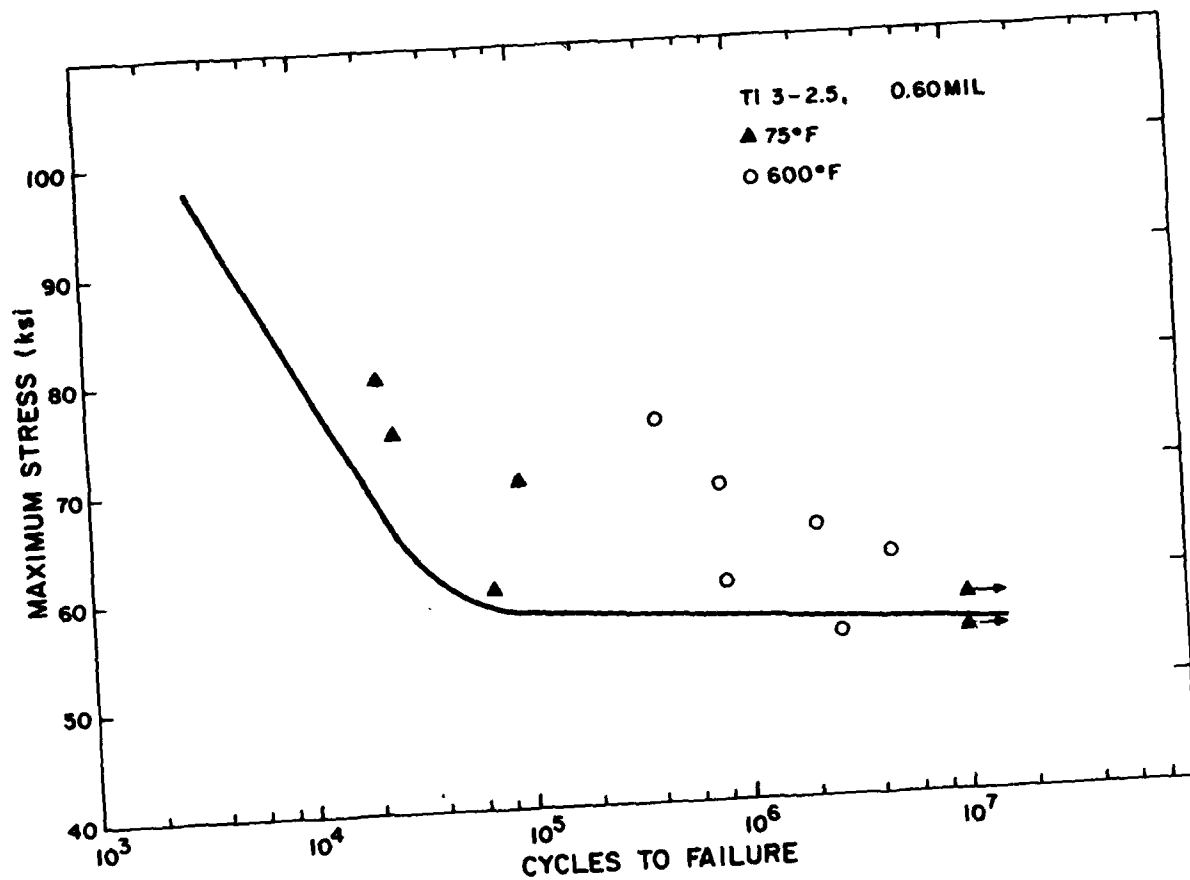
TABLE 5. MATRIX OF FATIGUE TESTS

<u>Material</u>	<u>Thickness</u> ( $10^{-3}$ in.)	<u>Temperatures</u> (°F)
CP Ti (4)	-	-
Ti 3-2.5	0.60	75; 600
Ti 15-3-3-3 As rolled and strand annealed	0.65	75
Ti 15-3-3-3 (Aged 1000°F, 8 hr)	0.65	75
Ti 15-3-3-3 (Aged 800°F, 8 hr)	0.65	75; 600



K9996

Figure 3. High cycle axial fatigue data for Ti 15-3-3-3 as rolled, and aged 1000°F, 8 hr. The data points with arrows at 10<sup>7</sup> cycles indicate test runouts.



K9997

Figure 4. High cycle axial fatigue data for Ti 3-2.5 at 75°F, and 600°F.

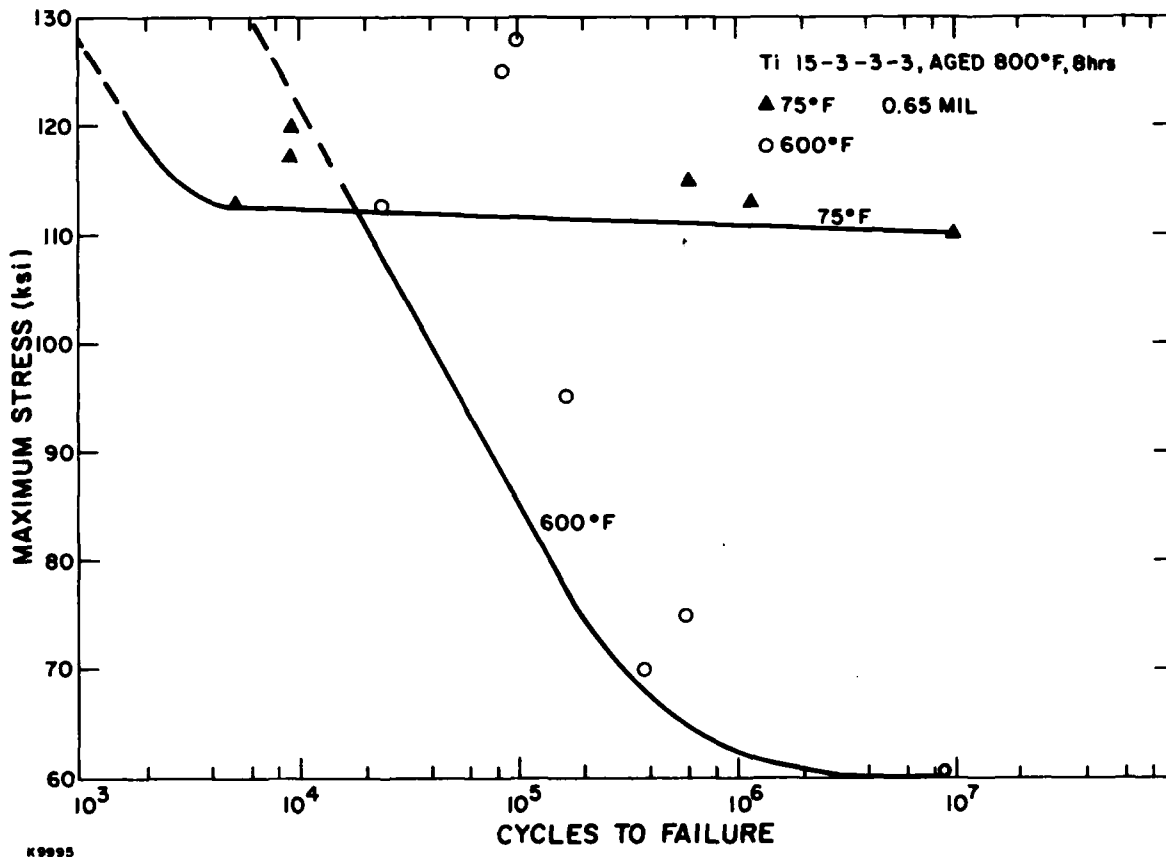


Figure 5. High cycle axial fatigue data for Ti 15-3-3-3, aged 800°F, 8 hrs. at 75°F and 600°F.

All foil samples were mounted in bakelite, using a Buehler "Met-Klip" for edge support. The face of the mount was polished with successively smaller grits down to 6  $\mu\text{m}$  and given a final polish on a Buehler "microcloth" with a slurry of 0.05 gamma alumina and distilled water.

In the case of Ti 3-2.5, etching was performed with standard Kroll's etch and, in the case of Ti 15-3-3-3 with ~ 1 percent HF in a saturated oxalic acid solution.

The structures will be discussed separately for each material:

- a) CP Ti (4), 0.5 mil and 1.0 mil. Examples of the structure are shown in Figure 6, in which it is seen that the  $\alpha$  grains (which make up all of the material) are elongated in the plane of the foil and have a thickness not much less than that of the foil. On average, there are about three grains in the thickness of the foil. The small circular features in Figure 6 are very probably etch pits caused by the heavy etching necessary to reveal the  $\alpha$ - $\alpha$  boundaries. It appears that the process of rolling from 1 mil down to 0.5 mil does not change the number of  $\alpha$  grains in the foil thickness, but further distorts them. The thinnest rolled foils are highly anisotropic in structure.
- b) Ti 3-2.5, 0.6 mil. Microscopy on this  $\alpha$ - $\beta$  alloy reveals a very fine grain structure with about 15 grains in the foil thickness (Figure 7). The grains are long and narrow and well interleaved. The Kroll's etch preferentially attacks  $\alpha$  material and, hence, we may suppose that the lighter crystal features, which correspond to raised areas, are probably the  $\beta$  grains. This structure resembles the Ti 3-2.5 structure observed by Hoffmar.<sup>(5)</sup>
- c) Ti 15-3-3-3, 0.65 mil, as rolled and strand annealed. In this condition, the foil is mostly in the  $\beta$  phase. In the bulk material, rapid cooling from 1450°F results in pure  $\beta$  phase. However, in very highly worked material such as the present foil, a very fine  $\alpha$  precipitate is observed throughout the volume of the  $\beta$  grains, whose boundaries are clearly seen in Figure 8(a). On average, there are only two  $\beta$  grains in the foil thickness and in many places only one. The  $\beta$  grains are not elongated after strand-annealing, but show a more equiaxed appearance.

5. C. G. Hoffman, Proc. IEEE Int'l. Pulsed Power Conference, IEEE, pp. III C-2-1, 12 (1976).



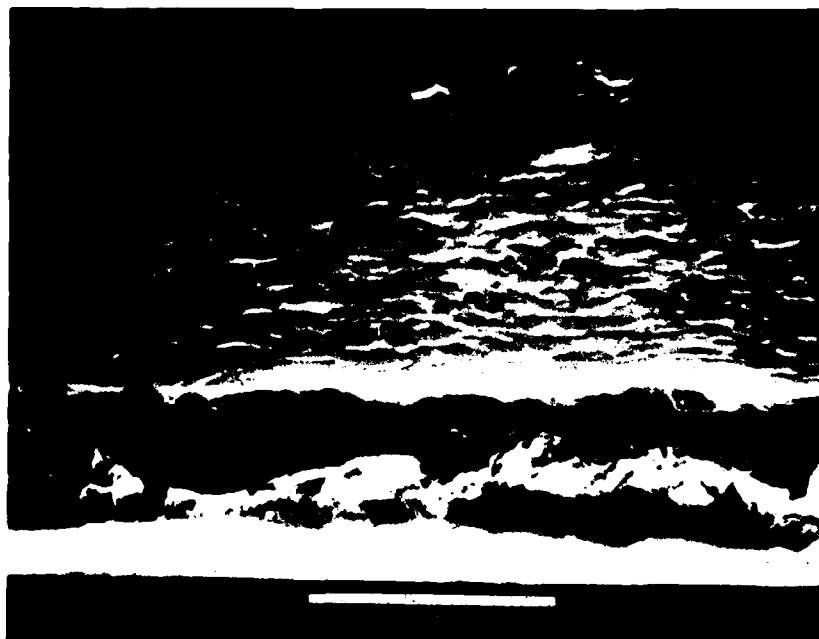
(a) 0.5 mil



(b) 1.0 mil

K9982

Figure 6. Scanning electron micrographs of CP Ti(4), 0.5 mil and 1 mil foils.



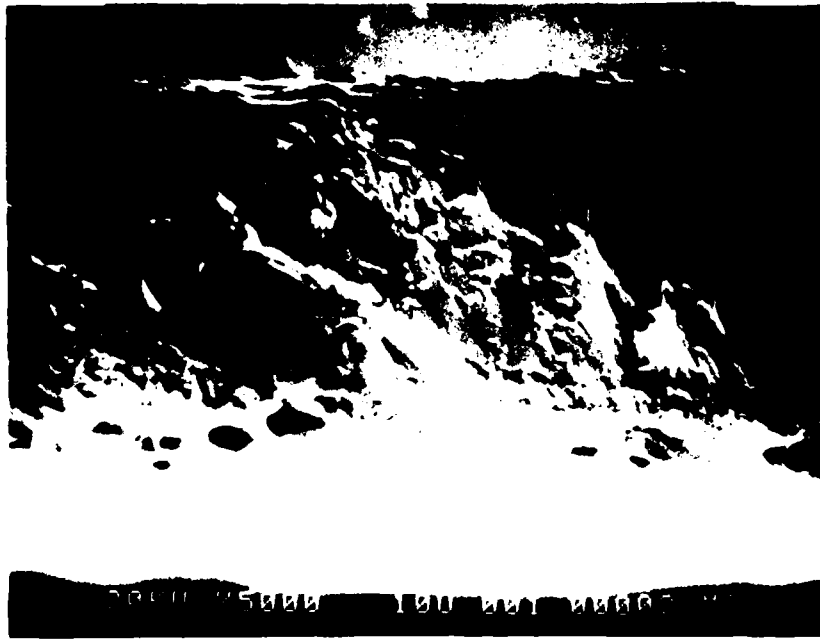
K9447

Figure 7. Scanning electron micrograph of Ti 3-2.5, 0.6 mil foil.

(a)



(b)



K9445

Figure 8. Scanning electron micrographs of Ti 15-3-3-3, 0.65 mil foil, as rolled and strand annealed: (a) grain structure in polished section (b) fracture surface of the same material.

A different view of the same material is afforded by scanning microscopy of its fracture surface, generated by tearing the foil [Figure 8(b)]. The fracture reveals  $\beta$  grain boundaries in which small  $\alpha$  grains are embedded. Such a structure has the potential to be very strong because of  $\alpha$  pinning of the  $\beta$  boundaries.

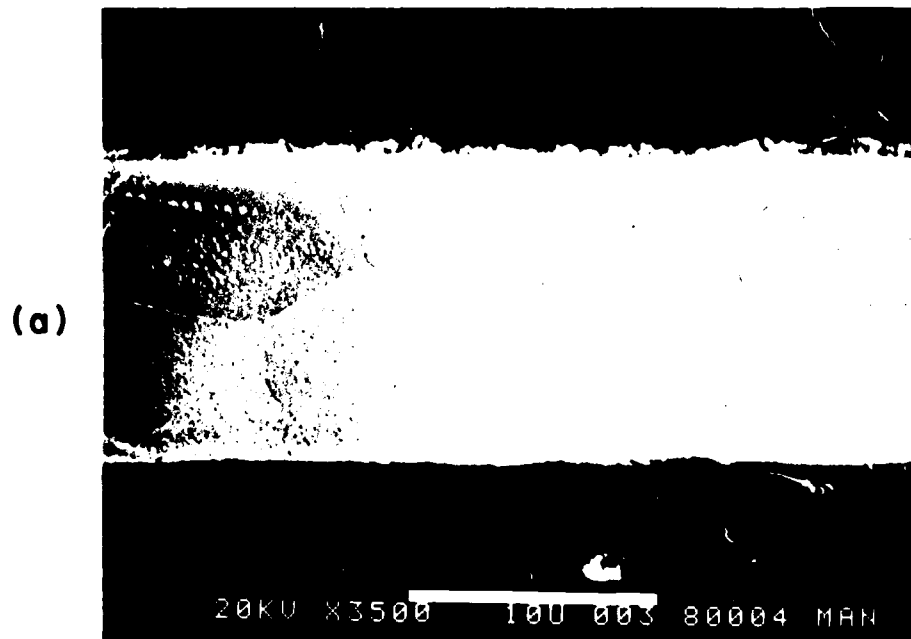
- d) Ti 15-3-3-3, 0.65 mil, aged foils. Ti 15-3-3-3 bulk material reaches its maximum strength after an "ageing" of  $\sim 8$  hr at  $1000^\circ\text{F}$ . However, in view of the presence of a finely distributed  $\alpha$  phase in the as-rolled and strand-annealed foil, it was thought that to develop the highest strength in a foil might not require so much ageing as in the bulk material. The tensile strength measurements recorded above do indeed show that a greater strength is achieved with lower temperature ageing, particularly the  $600^\circ\text{F}$  tensile data (Tables 2 and 3).

In order to generate reference structural data, a set of different ageing conditions were used on samples of Ti 15-3-3-3. Ageing was performed for 1 hr, 4 hr and 8 hr at each of  $800^\circ\text{F}$ ,  $900^\circ\text{F}$  and  $1000^\circ\text{F}$ . A vacuum of  $< 10^{-6}$  torr was used throughout.

Figure 9 shows the structures obtained for 4 hr and 8 hr ageing at  $800^\circ\text{F}$ . The  $\alpha$  phase develops from  $\alpha$  nuclei already present in the as-rolled foil, with the development being more rapid at the  $\beta$  boundaries.

Figure 10 shows the structures obtained by ageing at  $900^\circ\text{F}$  for 1 hr and 4 hrs. After 1 hr of ageing at  $900^\circ\text{F}$ , the structure is developed to the degree exhibited by  $\sim 4$  hr at  $800^\circ\text{F}$ .

Figure 11 shows the results of ageing at  $1000^\circ\text{F}$  for 1 hr and 4 hr. At 1 hr, the  $\alpha$  phase has already developed beyond the 8-hr,  $800^\circ\text{F}$  state, and at 4 hr, the general appearance is dominated by extensive  $\alpha$  plate development. More detail of this structure is shown in Figure 12(a), and the  $\alpha$  plates are more strikingly revealed in a fracture surface as illustrated in Figure 12(b). By examination of the fracture surface, we may speculate that the weak points in the material are the  $\alpha$  plates (smooth conchoidal fracture surfaces), and that already with  $1000^\circ\text{F}$ , 4-hr ageing, the  $\alpha$  phase is overdeveloped.



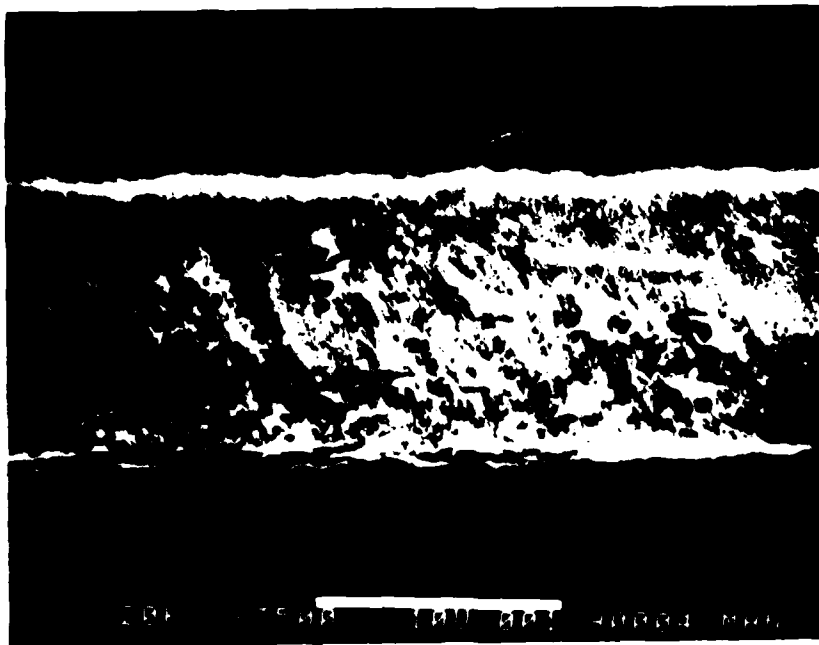
K9752

Figure 9. Scanning electron micrographs of Ti 15-3-3-3, 0.65 mil foil (a) aged 800°F, 4 hr. and (b) aged 800°F, 8 hr.

(a)



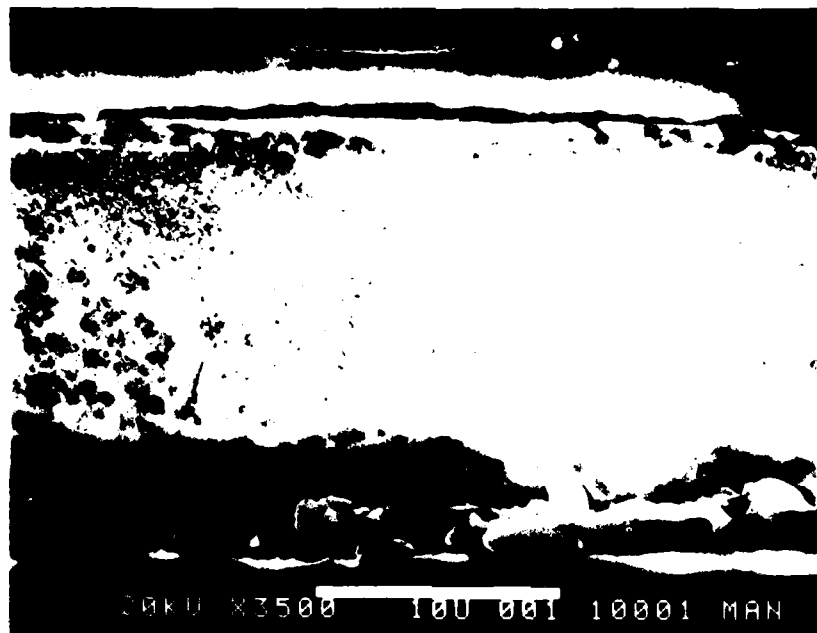
(b)



K9749

Figure 10. Scanning electron micrographs of T1 15-3-3-3, 0.65 mil foil (a) aged 900°F, 1 hr. and (b) aged 900°F, 4 hrs.

(a)



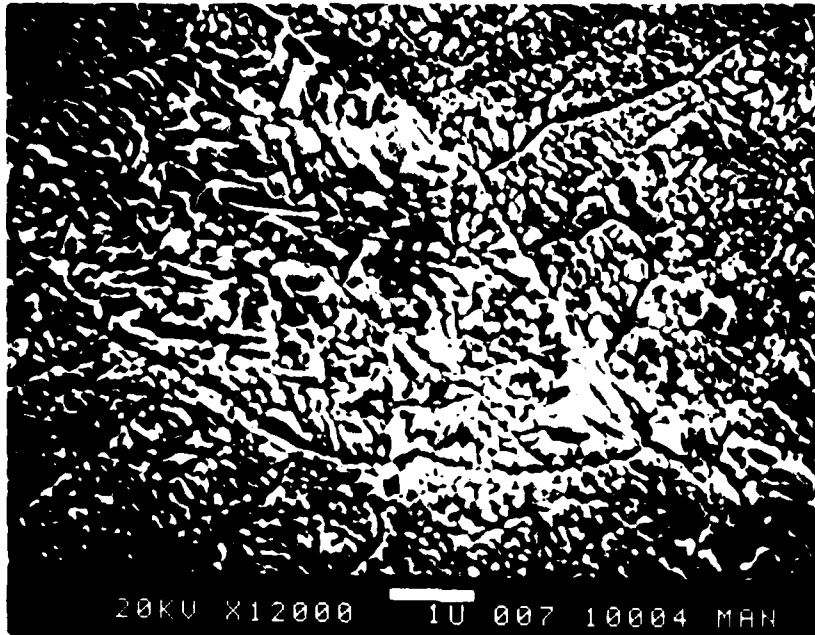
(b)



K9751

Figure 11. Scanning electron micrographs of T1 15-3-3-3, 0.65 mil foil (a) aged 1000°F, 1 hr. and (b) 1000°F, 4 hrs.

(a)



(b)



K9750

Figure 12. Scanning electron micrographs of Ti 15-3-3-3, 0.65 mil foil aged 1000°F, 4 hrs.: (a) magnification increased and (b) fracture surface.

Examination of these structures leads to the choice of 800°F, 8 hr ageing for the more detailed tensile and fatigue analyses recorded above. Although the room temperature tensile strength does not differ greatly between 800°F, 8-hr and 1000°F, 8-hr ageing, the R.T. fatigue data in Figures 3 and 5 shows a very much better high-cycle fatigue strength (110 ksi) for the 800°F ageing than for the 1000°F ageing (80 ksi). Unfortunately, we did not have the resources to compare 600°F fatigue data for these two ageing conditions. As the data of Figure 5 shows, there is an atypical decrease in fatigue strength of the 200°F, 8-hr material at the elevated fatigue temperature. Because the degree of ageing at 600°F during  $5.10^5$  cycles (4.6 hrs) would not be very significant according to this survey of structures, it is speculated that this decrease in fatigue strength might be caused by transient local stresses occasioned by the small degree of phase transformation that is occurring at 600°F. Further work is needed on the elevated temperature fatigue aged Ti 15-3-3-3 foils to clarify this issue.

### 3.0 MODELING OF STRESS DISTRIBUTION IN LOADED FOIL WINDOWS

#### 3.1 INTRODUCTION

Present-day techniques in the finite element modeling of plastic materials allow a complete description of the foil stresses once the material properties are known. Stress-strain curves for the candidate foil materials have been presented in Section 2.2 so that, in principle, the burst pressure and fatigue life of foil windows can be predicted. As we shall see in Section 4.0, the issue is not straightforward because we have measured burst pressures substantially higher than a model using the measured uniaxial strength would predict. In fact, we have to invoke a substantial biaxial strength enhancement in order to account for the burst data. This, in turn, implies that the Ti foil windows remain elastic to much higher stress levels than the quoted uniaxial 0.2 percent YS levels of Section 2.2. In order to retain generality we first discuss the broad features of foil stress distribution for an assumed elastic Ti foil material (Section 3.3), specializing to a particular model of inelastic material in Section 3.4. In the latter section, we demonstrate reduced peak stress caused by material yield above the support rib, and also show that high pressure pre-forming can, in principle, reduce the peak foil stress during laser operation at a lower pressure. In Section 3.3, the stresses in foils over an elliptical rib are computed as a function of ellipticity and a stress minimum is demonstrated for ellipticity  $\sim 8$  in a 60 percent transmitting rib structure.

#### 3.2 USE OF THE NASTRAN STRUCTURAL CODE

NASTRAN is a general-purpose digital computer program designed to analyze the behavior of continuous structures under a range of loading and boundary conditions using a finite-element approach. The finite-element formulation embodies a discrete or lumped element idealization of a continuous physical system. This discrete system is represented by a finite number of sub-structural elements interconnected at a finite number of grid points.

Further details of the formulation are given in the MacNeal-Schwendler Corporation Report, MSR-40, the Nastran-Theoretical Manual, December 1972.

NASTRAN provides non-linear analysis for structures having both geometric and material non-linearities. The geometric non-linearities include the geometric stiffening effects caused by large displacements such as encountered when a thin membrane is loaded normally and stressed in tension. The material non-linearities include options for plastic yield, flow, hardening effects, and non-linear elastic functions.

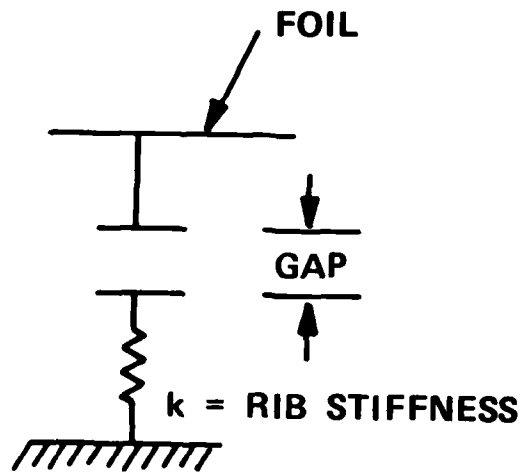
At the finite element level, a gap element, a plastic hinge for beam elements and plate elements have been provided. The gap element provides for spaces in the structure which can close, open and slide such as between the foil plane and the curved rib support surface. As the foil deforms under a load, it moves freely until it makes contact with the rib surface. Upon contact, the rib structure provides large resistance to further foil movement at the contact locations, as shown schematically in Figure 13.

The plastic hinge for beam elements is accounted for automatically. The beam cross section is divided into eight equal sub-areas. The sub-areas are analyzed as individual rods with elasto-plastic material properties.

The material non-linearity provides for two broad categories; non-linear elastic and plasticity, as shown in Figure 14. For the non-linear elastic relation, the unloading follows the stress-strain curve, whereas elastic unloading occurs in the plastic analysis.

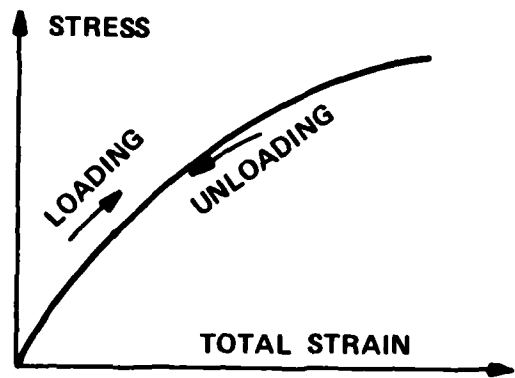
Four yield function options and three Bauschinger effect options are provided. The yield criteria are based on the following theories: von Mises, Tresca, Mohr-Coulomb and Drucker-Prager. The Bauschinger effects describe the material-hardening behavior of a plastically deformed specimen when it is unloaded, as depicted in Figure 15. Three hardening rules are provided: kinematic, isotropic and combined. The stress-strain relations by Pradt and Reuss are employed for elastic-plastic materials. For further details, see Section 2.14 of the MSC/NASTRAN Application Manual.

The non-linear solution algorithm for statically applied loads is based on iteration techniques, with the load divided into incremental steps. See the Application Manual for details since the algorithm is complex and too lengthy to describe here. The algorithm employs three error criteria in the iteration process: the unbalanced displacement vector, the unbalanced force

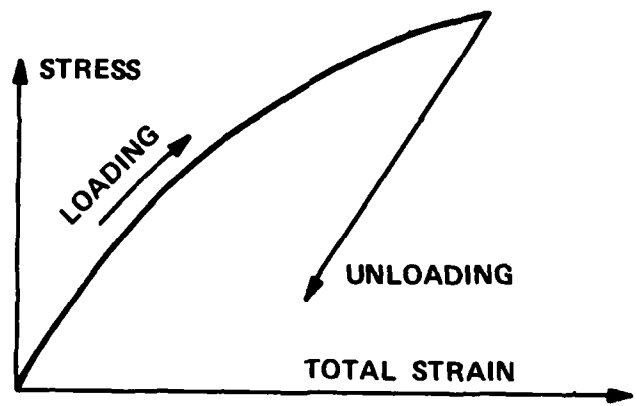


K9991

Figure 13. Schematic of foil movement constraints in model.



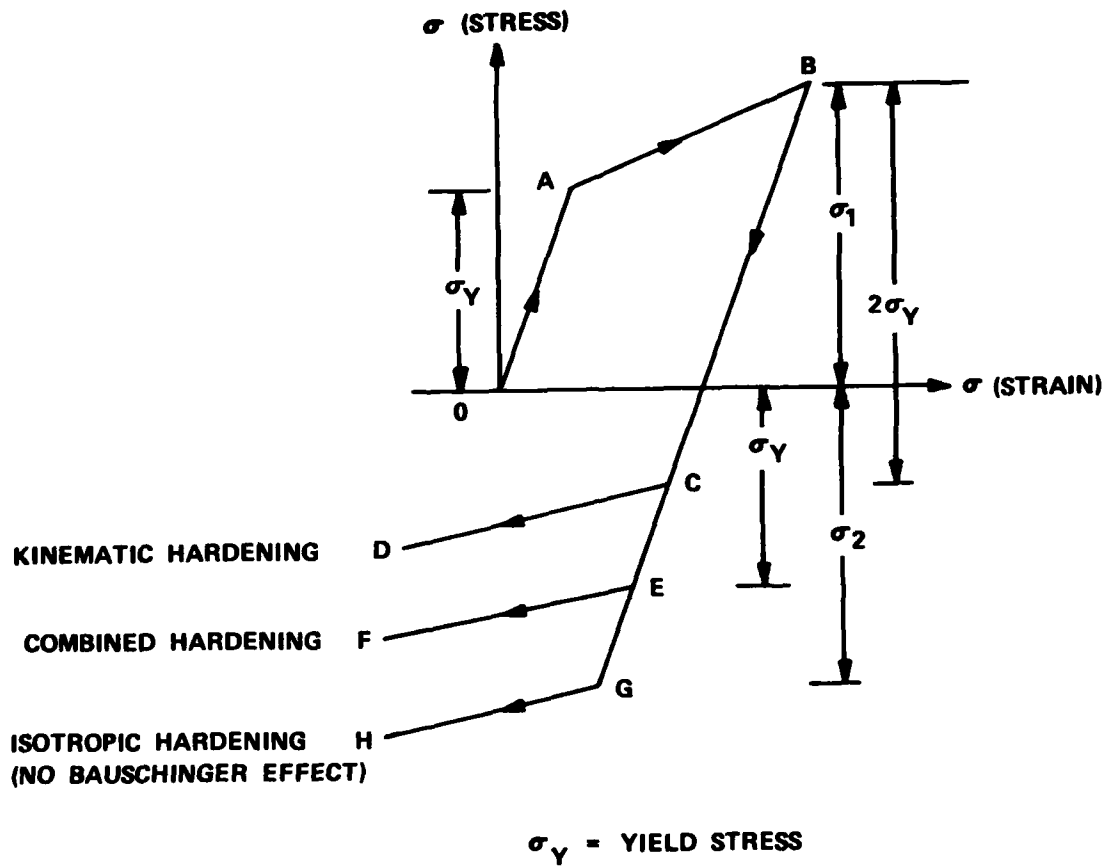
(a) NONLINEAR ELASTIC



(b) PLASTIC

K9992

Figure 14. Material options in NASTRAN.



K9993

Figure 15. Plastic deformation model in NASTRAN.

vector and the energy error fraction. The Newton-Raphson iteration method is included in the algorithm. Element stiffness updates are provided automatically or at iteration intervals as specified by the user, based on the material tangent modulus at the current load.

Transient analysis of non-linear structure with dynamically applied loads is performed utilizing the numerical techniques for static loads with time steps replacing load steps. The Newmark Beta Method is employed for transient integration combined with the Newton's Method for non-linear solutions.

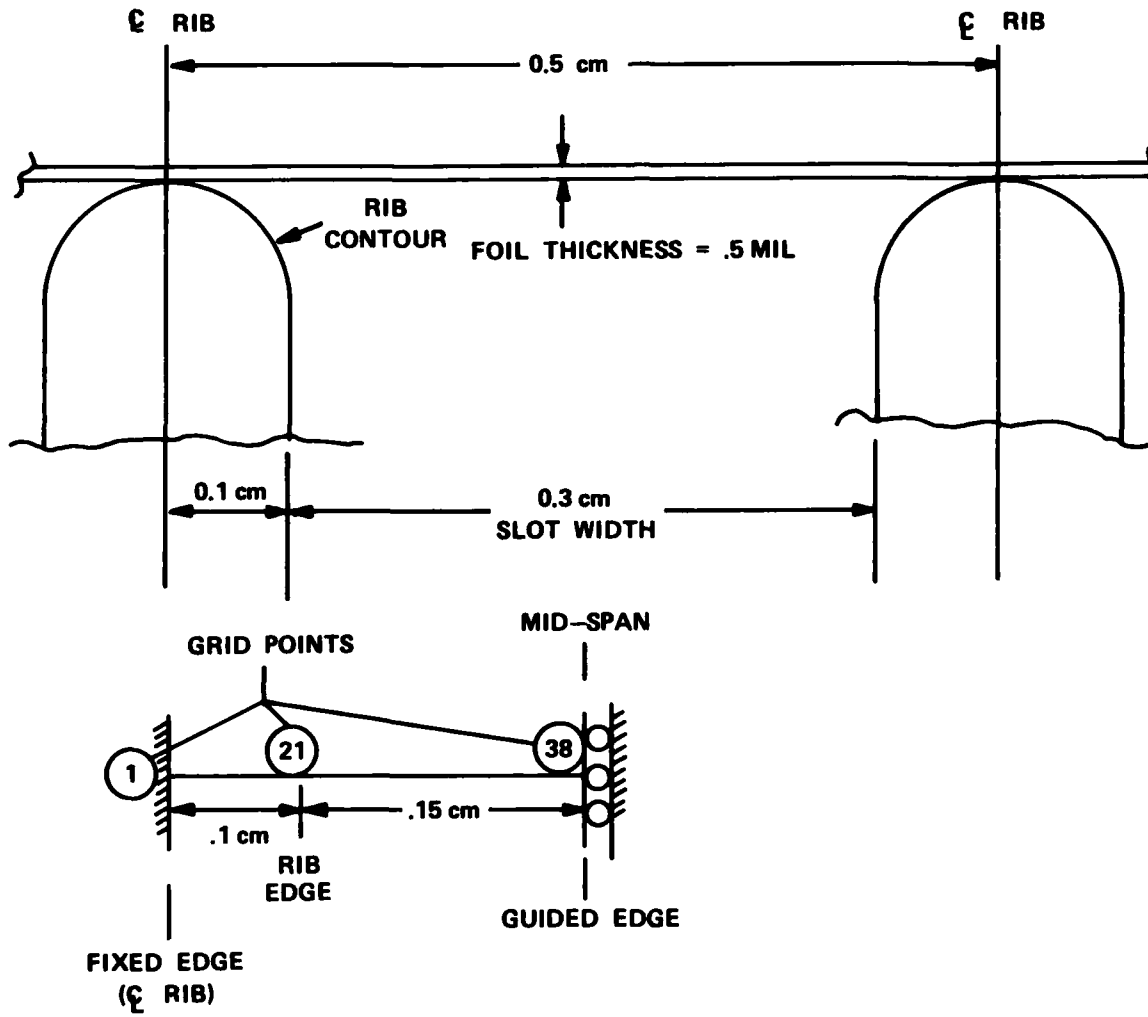
NASTRAN has a restart capability for both the static and transient analysis. The stress-strain data at any specified load can be stored in a data file and the problem can be restarted from the last load condition and continued with the loading history. Transient analysis can be performed on restart from a static load condition. This is useful in the foil analysis as it is initially loaded statically, after which the dynamic pressure pulse load is applied during a laser firing.

The foil is modeled as a beam with a unit width between two rib supports, as shown in Figure 16. As the foil is stretched over several ribs, the slope at the rib centerlines is zero because of a pressure load. Hence, only one half of the foil span is modeled because of symmetry. The slope at the foil mid-span between rib supports is zero but deflection is allowed at that point.

The foil model consists of 38 grid points, with 21 grid points for the rib support surface. Ten equally spaced gap elements are included to describe the normal gap between the foil and the rib surface. Each gap element allows the foil to move freely under load until it contacts the gap surface. When contact occurs, the rib stiffness resistance is applied to the foil to prevent further motion at that location. The rib thickness is 0.2 cm and the slot width between ribs is 0.3 cm in the example of Figure 16.

Use of a typical friction coefficient shows that the foil will tend to slip in the tangent direction to the support rib surface because the friction forces are greatly exceeded by the membrane forces. In the model, we have used a zero coefficient of friction.

Several rib contours were considered in the trade-off study: a circular contour, ellipse contours with 6 to 1, 10 to 1 and 15 to 1 aspect ratios, and a flat surface with a corner radius.



K9994

Figure 16. Detail of foil beam model for the case of a circular rib profile, 0.5 cm rib spacing and 0.3 cm slot.

### 3.3 ELASTIC FOIL STRESS RESULTS

The stress in the pressure-loaded foil is composed of a membrane stress term with a superimposed bending term. The peak stress occurs at a point on the pressure side of the foil above the support rib. This is caused by the additive effects of membrane and bending stress. The position and magnitude of the stress maximum depend sensitively on the contour of the support rib, the foil thickness and applied load.

In this modeling study and in the experiments to be discussed later, we have used two different generic support shapes, illustrated in Figure 17. In all of the modeling, we have used a rib width of 0.2 cm, but we have varied the slot width, using slots of either 0.3 cm or 0.5 cm, corresponding to geometric transmissions of 60 percent and 71 percent, respectively.

In the present section, where purely elastic material is considered, an elastic modulus  $E = 15 \times 10^6$  psi is used throughout, as being representative of Ti alloy foils (Section 2.2).

Examples of computed stress distributions for a 0.5 mil foil, 0.5 cm slot and 7 atm load are shown in Figures 18 and 19. The region of high peak stress on the pressure side is complemented by a low stress region on the rib side where the bending stress cancels some of the membrane stress. In the mid-span region, the membrane stress is the mean of the two curves, and its value depends to first order on the length of unsupported foil between the ribs. A good approximation to the membrane force  $P$  (lb/in.) and mid-span deflection  $Y_{MAX}$  (in.) is given by the following formulae<sup>(6)</sup> for flexible cables, modified to represent a loaded ribbon of thickness  $t$ . (in.):

$$Y_{MAX} = l \left( \frac{3p l}{64Et} \right)^{1/3} \quad (1)$$

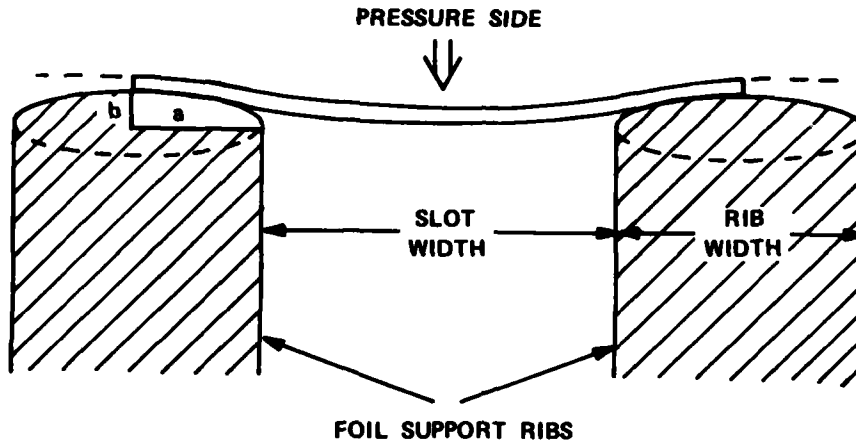
and

$$P = \frac{p l^2}{8Y_{MAX}} \quad (2)$$

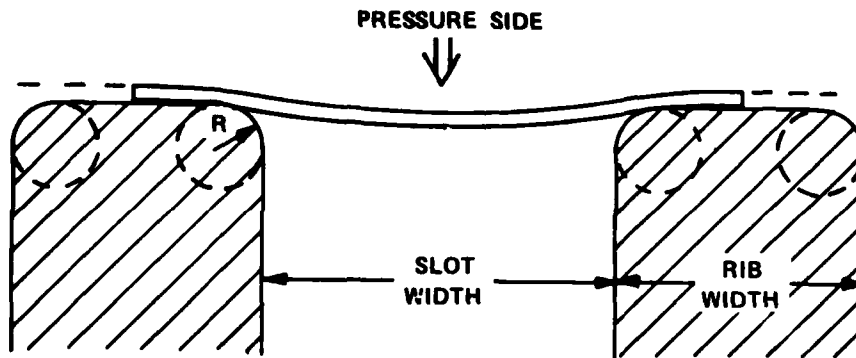
6. Formulas for Stress and Strain, Roark and Young, 5th Edition, McCraw Hill

(a) ELLIPTICAL SUPPORT

ELLIPTICITY =  $a/b$

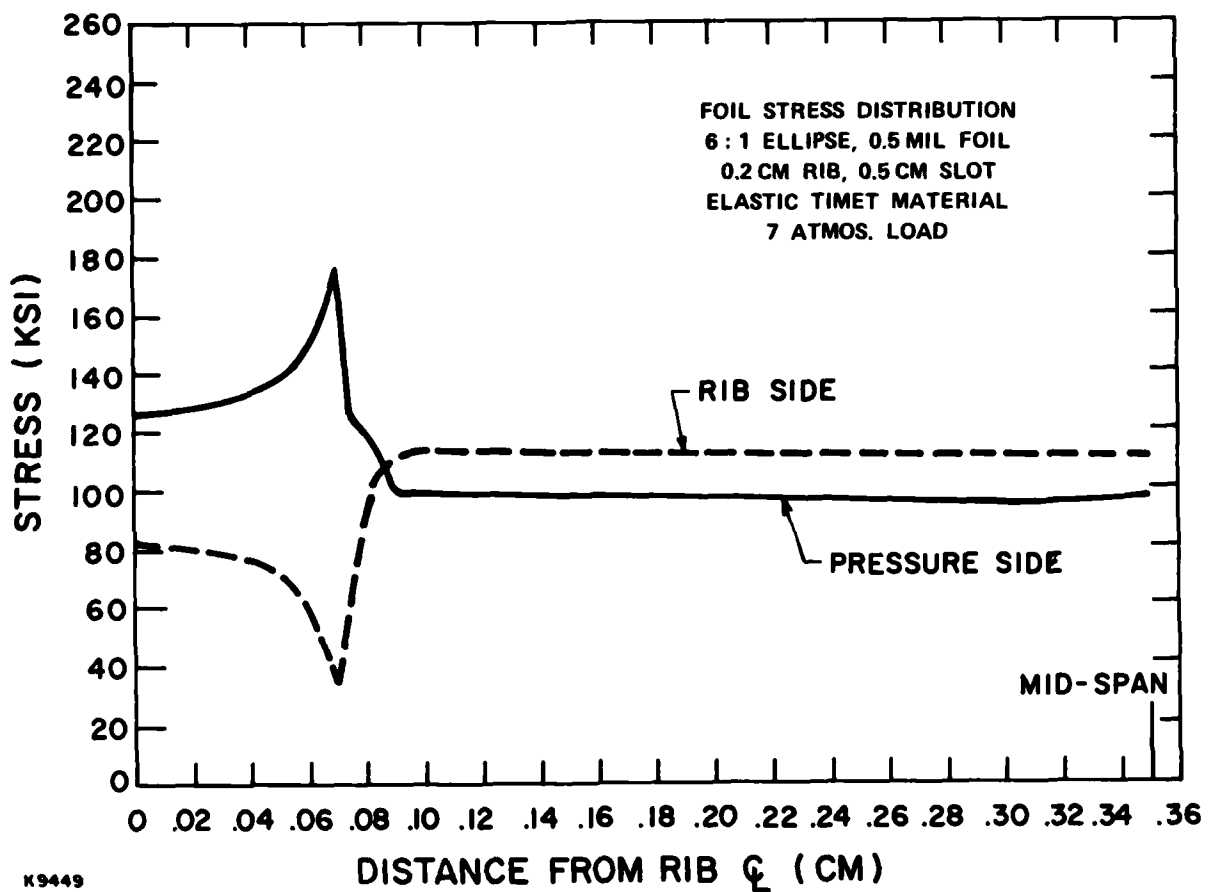


(b) RADIUSED FLAT SUPPORT



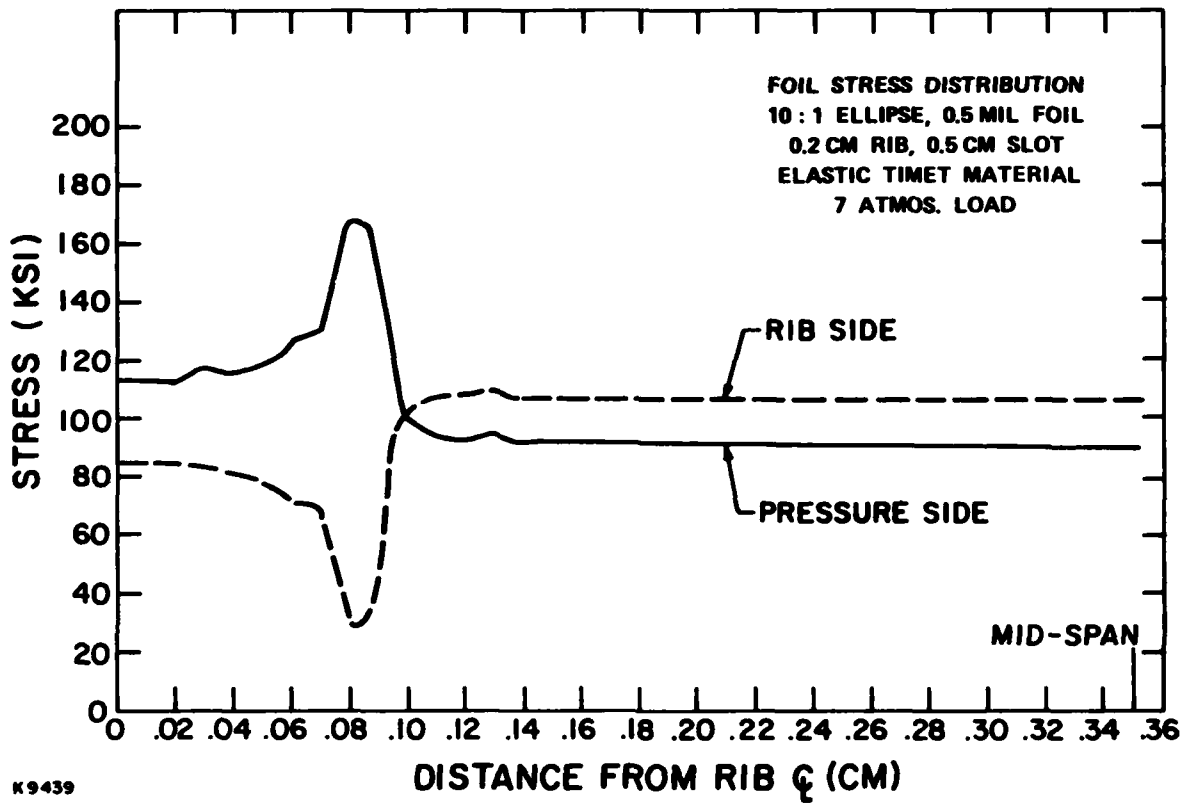
K9990

Figure 17. Generic foil support rib contours.



K9449

Figure 18. Stress distribution in 0.5 mil elastic Ti foil at 7 atmospheres. 6:1 elliptical rib, 0.5 cm slot.



K9439

Figure 19. Stress distribution in 0.5 mil elastic Ti foil at 7 atmospheres. 10:1 elliptical rib, 0.5 cm slot.

in which  $E$  is the material elastic modulus (psi),  $\ell$  is the free span (in.), and  $p$  is the applied pressure load (psi). In the case of 5 atm loads on elliptical support ribs of ellipticity  $6 > 10$ , the free span is approximately equal to the slot width plus 20 percent of the rib width. The NASTRAN calculations give membrane stress values within 5 percent of the above expressions.

The magnitude of the bending stress depends strongly on the exact support rib profile. In a comparison between the two generic support shapes (Figure 17) it was found that the stress maximum for the ellipse could be made  $\sim 0.8$  times that for the radiused flat, when cases of optimized ellipticity were compared with cases of optimized radius. For this reason, the remainder of the modeling is of elliptical supports, although a radiused flat was used in some of the experiments to be discussed.

Figures 20 and 21 show the peak stress distribution in 0.5 mil and 1.0 mil elastic foils for ellipticities 1, 6 and 10. Ellipticity 1 implies a circular rib profile. It presents very high peak stresses near to the rib centerline because the free span is long and the foil is curved sharply over the contact region. Between Figures 20 and 21, we note that doubling the foil thickness has a relatively small effect on the membrane stress [cf, formula (1) above]. It also does not significantly change the bending stress, so that doubling the foil thickness only decreases the peak foil stress by  $\sim 25$  percent for ribs of ellipticity  $6 > 10$ .

A further calculation at ellipticity 15 showed peak stresses  $> 500$  ksi, indicating that the least stress optimum lay between 6 and 10, as shown in Figure 22 for 0.5 mil and 1.0 mil foils. Because of the expense of this computation (\$200 per point on average), we did not perform optimization for the 0.5 cm slot, or other cases. However, the result appears to be similar, judging from the data points we have; that is, the optimum support ellipticity is  $\sim 8$ . Although the ellipse is a very promising profile, which is simple to tool for (as demonstrated below), the present calculations do not exclude the existence of even better shapes, although the margin for improvement diminishes as the bending stress becomes small relative to the membrane stress.

The ratio of peak stress on the rib to peak stress at the mid-span is explored in Figures 23 and 24, which relate to 0.5 mil foil, a 0.2 cm rib and a 0.5 cm slot at ellipticities 6 and 10, respectively. The most important

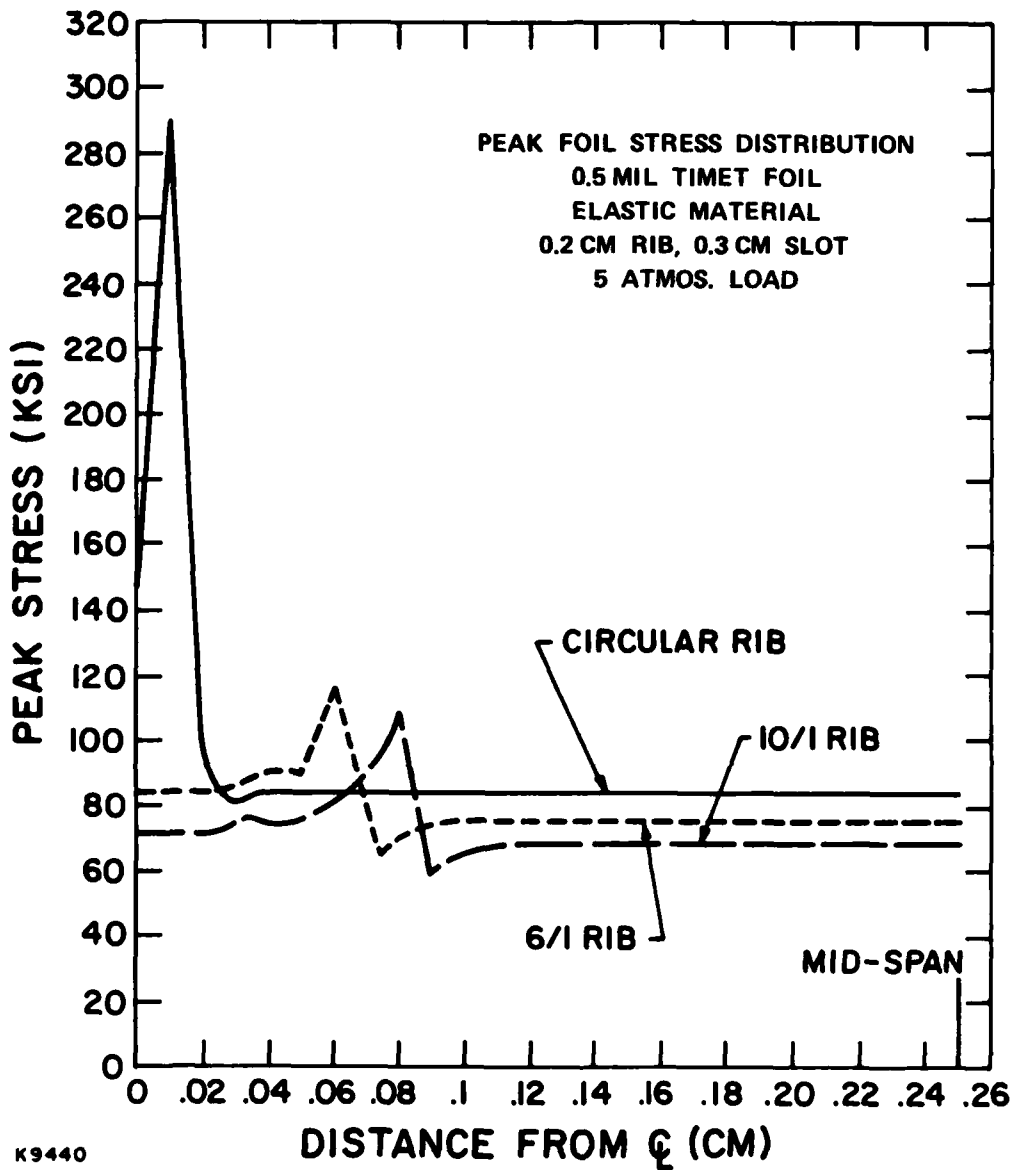
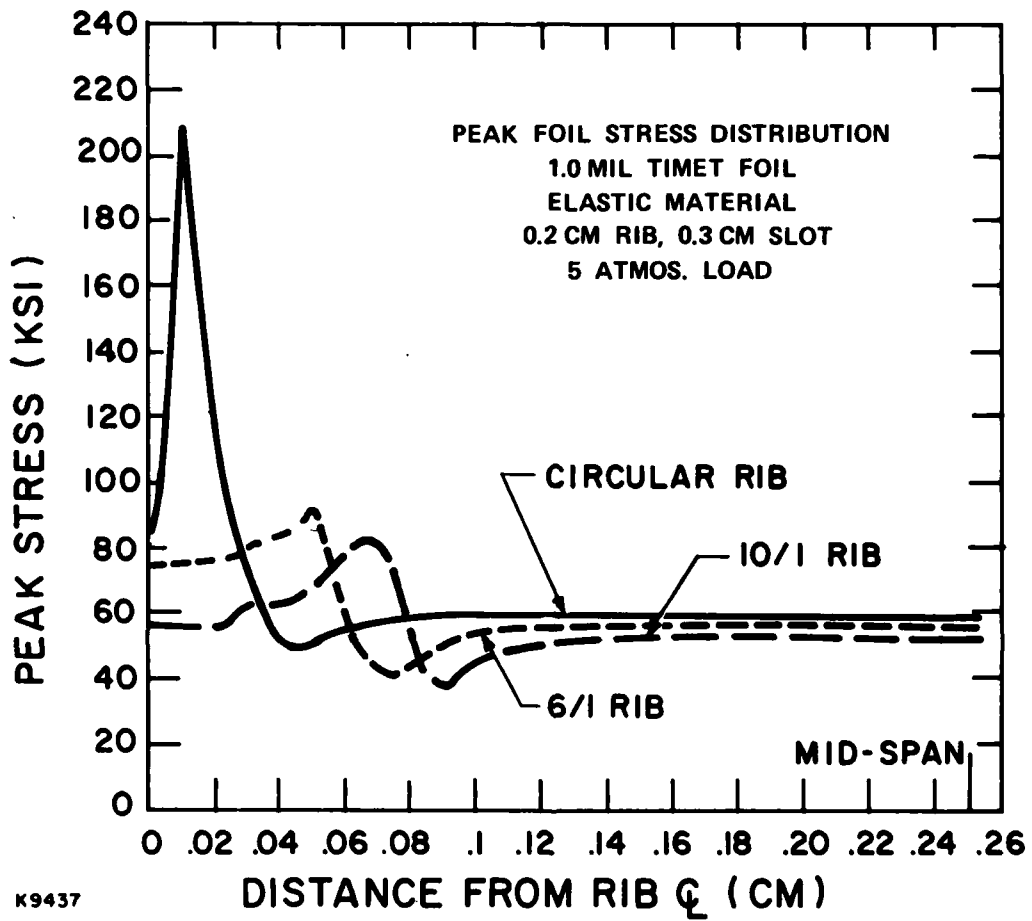
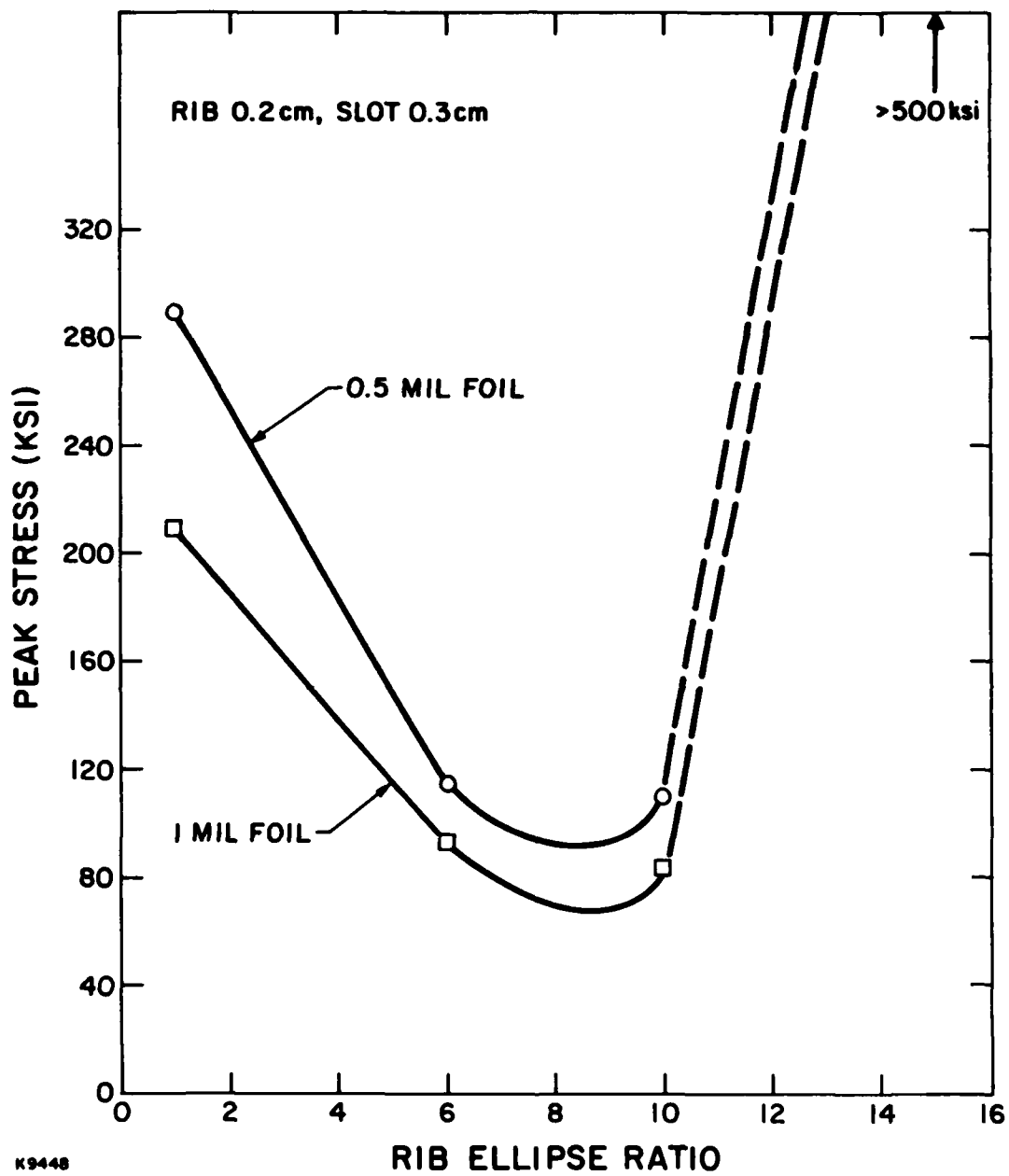


Figure 20. Distribution of peak stress in 0.5 mil elastic Ti foil at 5 atmospheres. 0.3 cm slot, rib ellipticities 1, 6 and 10.



K9437

Figure 21. Distribution of peak stress in 1.0 mil elastic Ti foil at 5 atmospheres. 0.3 cm slot, rib ellipticities 1, 6 and 10.



K9448

Figure 22. Peak stress as a function of ellipticity, showing optimum rib profile for 0.5 mil and 1.0 mil elastic Ti foils loaded to 5 atmospheres.

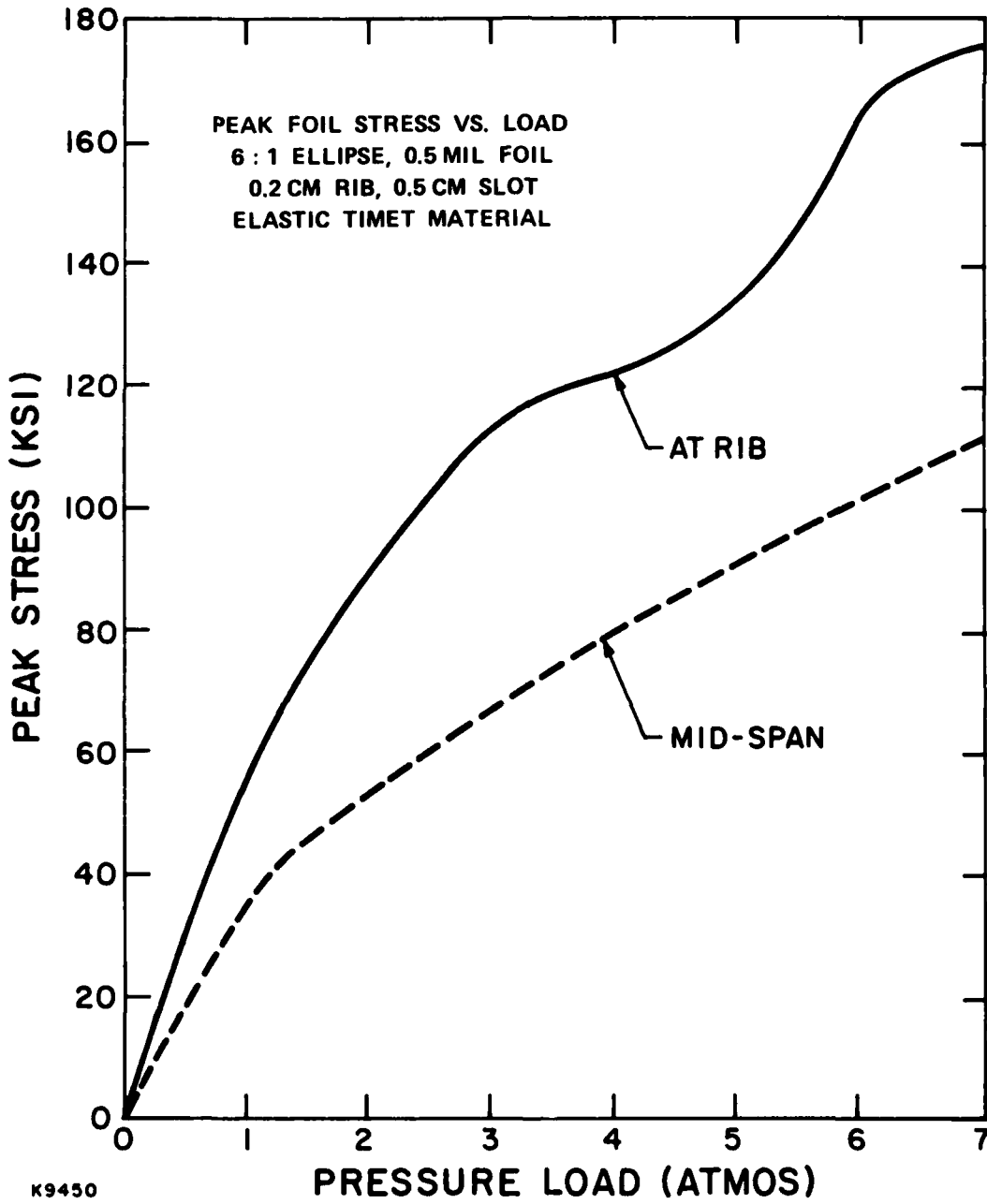
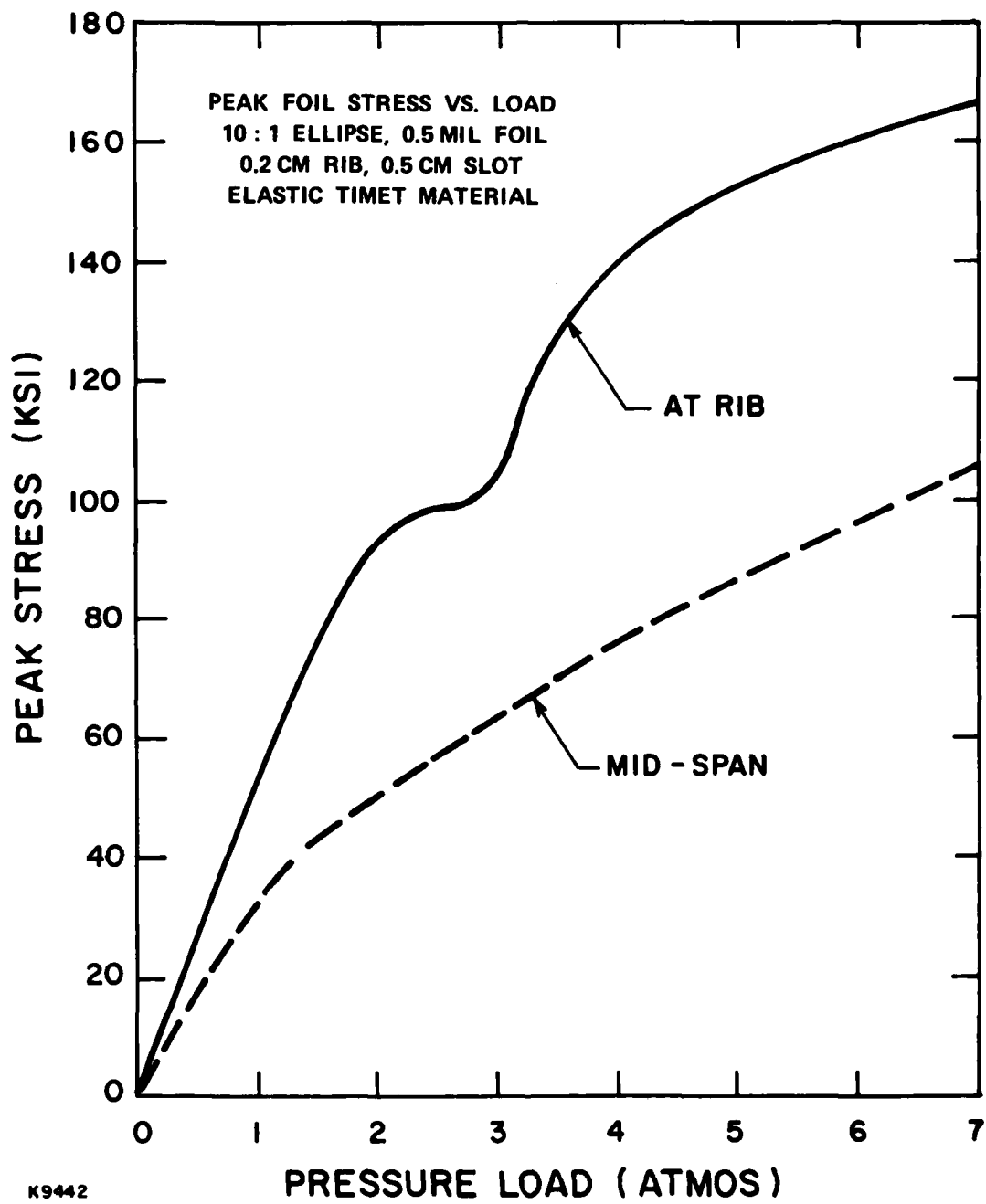


Figure 23. Peak stress at rib and midspan as a function of loading for 0.5 mil elastic Ti foil, 0.2 cm rib, 0.5 cm slot, and rib ellipticity 6.



K9442

Figure 24. Peak stress at rib and midspan as a function of loading for 0.5 mil elastic Ti foil, 0.2 cm rib, 0.5 cm slot, and rib ellipticity 10.

aspect of this data is the roughly constant ratio of peak rib to mid-span stress ( $\sim 1.5$ ) which may be used to estimate peak rib stress at these ellipticities once the membrane stress has been calculated from formulas (1) and (2).

Also noteworthy is the dip in the peak rib stress curve, which shows that, for a constant ellipticity, the stress is optimized relative to the applied load at only one loading. This is a different aspect of the shape optimization at constant loading discussed above.

The foil deflected shape is a catenary near the mid-span, but has an inflexion point very close to the first point of contact with the rib, so that the reversed curvature of the rib surface can be accommodated. The inflexion point may be read from a plot of the peak stress, because the local zero in bending stress gives a minimum in the total stress at that point. For example, in Figure 20, the 6:1 ellipse rib has its stress minimum at 0.075 cm from the rib centerline. Examination of the deflected shape shows that this is, within error, the position where the foil ends its contact with the rib.

The mid-span deflection of the foil accords with formula for  $y_{\max}$  to within 5 percent accuracy once the appropriate value of  $l$ , the free span, is inserted. An example of the peak deflection as a function of pressure load is given in Figure 25.

### 3.4 DEFORMABLE FOIL STRESS RESULTS

Above a certain loading all real foils undergo plastic deformation, according to the stress-strain curves in question. As discussed in Section 3.2, the NASTRAN code can handle arbitrary material properties, but using a particular stress-strain curve deprives the results of much of their generality. We, therefore, present only a limited number of calculations for deformable material and, in the present section, limit ourselves to a qualitative discussion only.

For the purpose of discussion we consider a material with  $E = 15 \times 10^6$  psi up to 120 ksi, deforming linearly above this stress as shown in Figure 26.

In Figure 27 we show the computed stress at different loadings on a 6:1 ellipse rib. At 5 atm pressure (75 psi), the peak stress has nowhere exceeded 120 ksi and, hence, no deformation has taken place. At 7 atm, the material

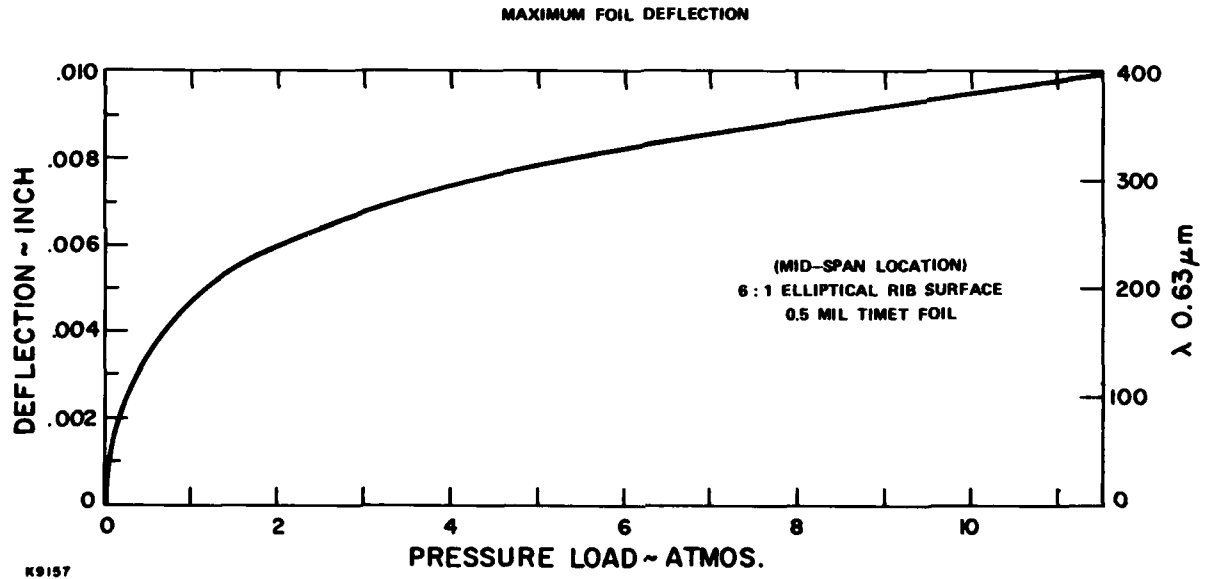


Figure 25. Peak deflection as a function of loading for 0.5 mil elastic Ti foil, 0.2 cm 6:1 ellipse rib, 0.3 cm slot.

**ASSUMED PLASTIC FOIL MATERIAL PROPERTIES**

**MATERIAL: TITANIUM ALLOY (EXAMPLE)**

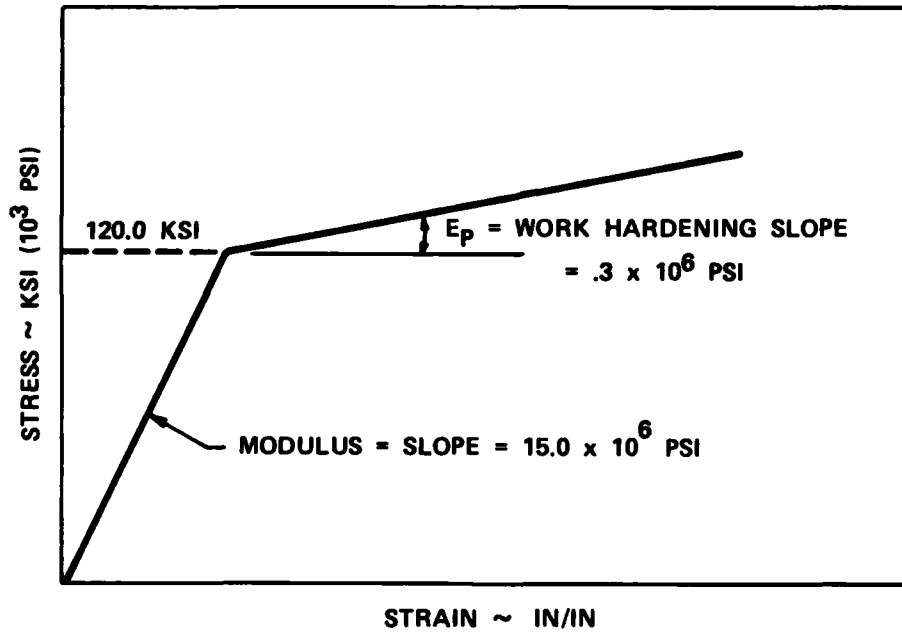
**DENSITY = 0.172 LB/IN<sup>3</sup>**

**MODULUS = 15.0 x 10<sup>6</sup> PSI AVERAGE**

**POISSON'S RATIO = 0.32**

**YIELD STRENGTH = 120,000 PSI (.2% YIELD)**

**STRESS-STRAIN CURVE USED FOR NASTRAN CODE**



**ASSUMED PLASTICITY FOR UNLOADING, ASSUMING COMBINED ISOTROPIC & KINEMATIC HARDENING RELATION. (TENSILE & COMPRESSIVE YIELD STRENGTH ARE INDEPENDENT AND  $\sigma_Y$  (COMP.) = -  $\sigma_Y$  (TENSION) ).**

**K9987**

**Figure 26. Stress-strain curve assumed for deformable material example.**

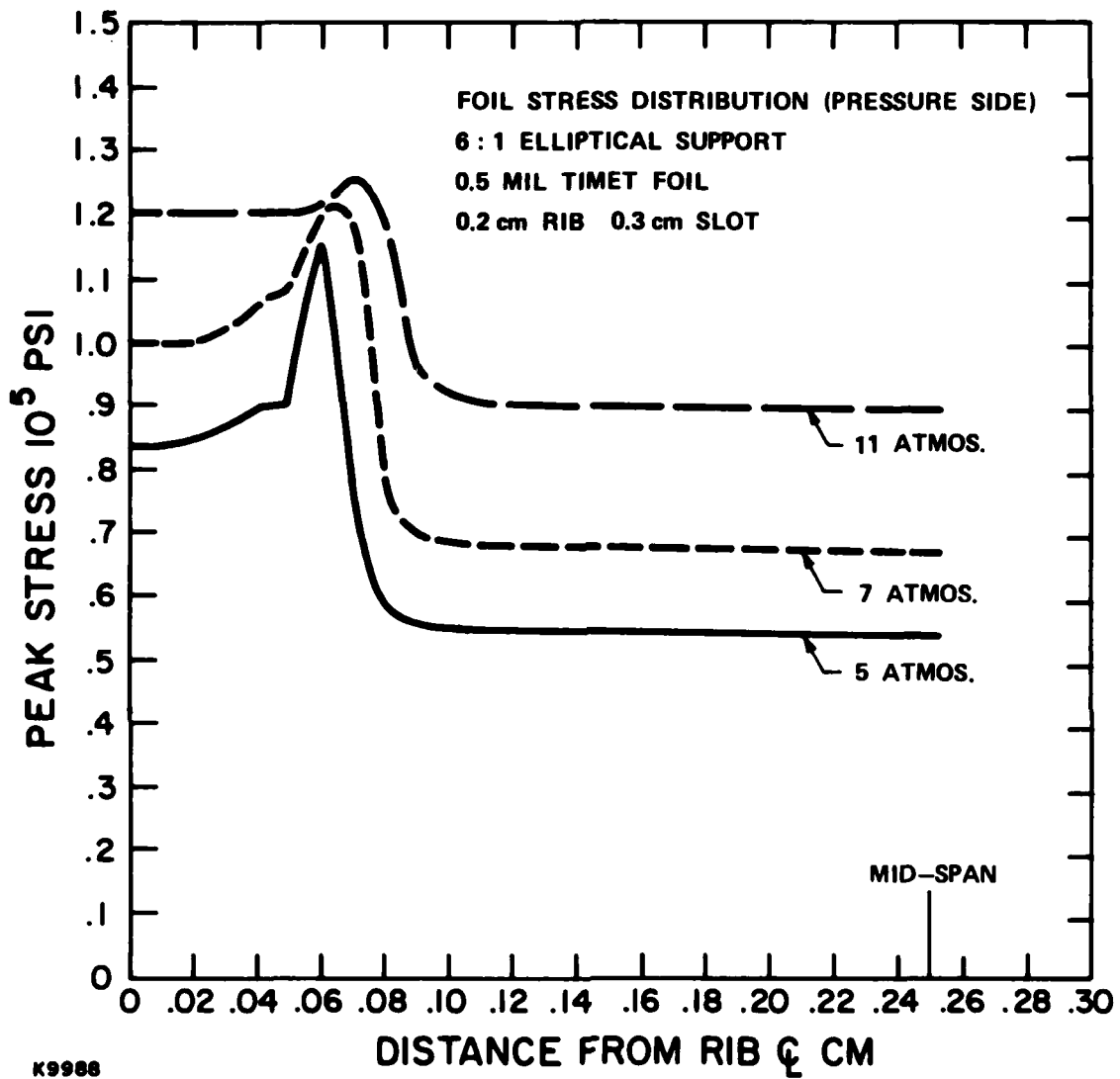


Figure 27. Peak stress as a function of loading for 0.5 mil deformable T1 example.

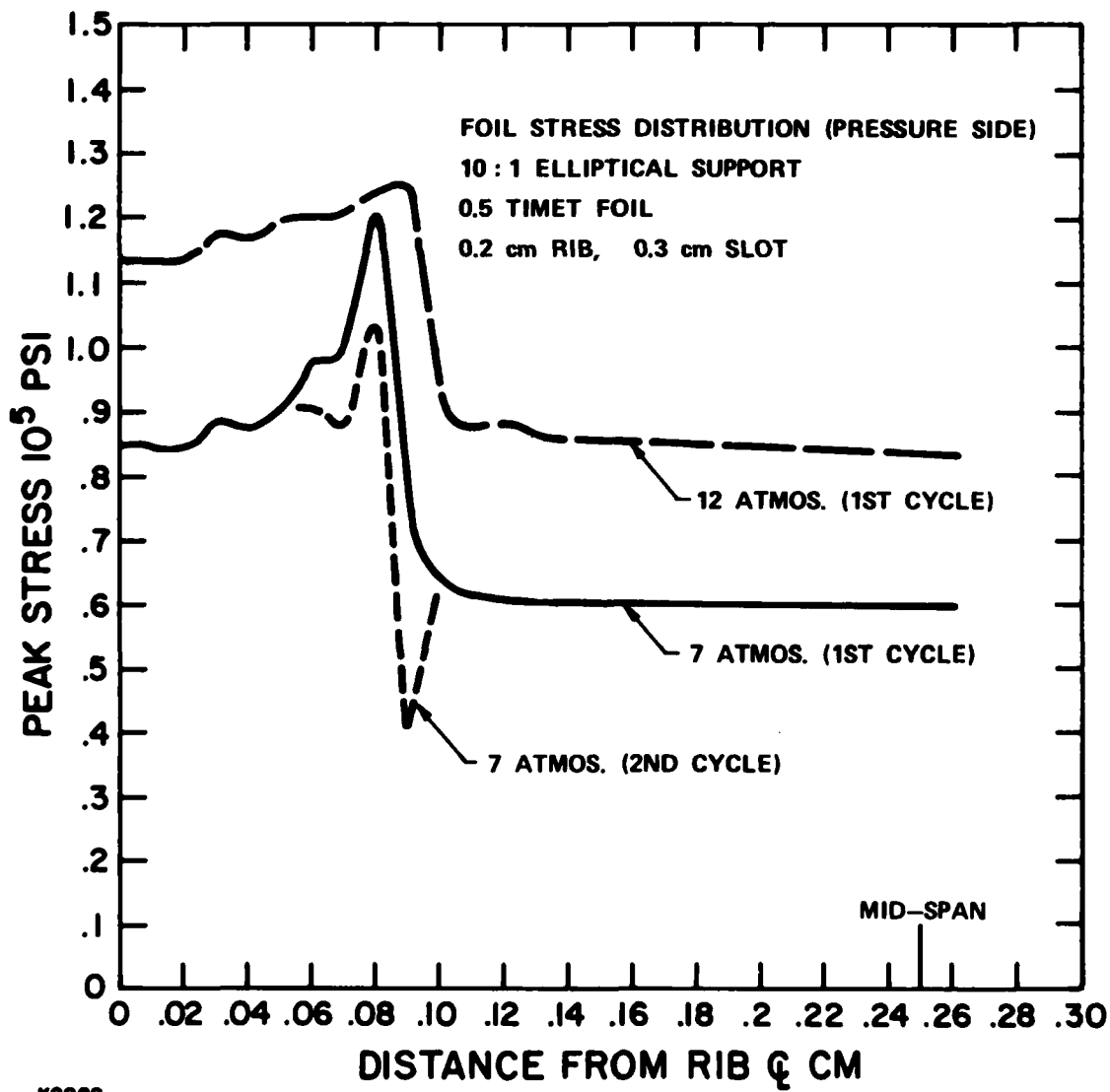
has begun to yield on the pressure side near the edge of the region of support. At 11 atm, the region of deformation has spread to cover the entire contact area with the rib support. However, only at the peak stress point has the foil material yielded throughout its whole thickness.

Once yield has occurred, the foil retains a dimpled structure on unloading, which is familiar to the experimentalist who has ever removed a foil after use. The pressure at which deformation is first observed is an important parameter test of this modeling, and more will be said on this subject in Section 4.4.

A possible method of reducing the foil bending stress is pre-forming of the foil by application of sufficient pressure to induce a permanent bend in the foil before use at a lower pressure. This technique depends upon the foil material retaining its strength in the process of cold forming, which is a reasonable first approximation for small deformations. The process was investigated on the computer using the example of deformable material given in Figure 26. An initially flat foil was loaded to 12 atm, unloaded to 1 atm, and re-loaded to 7 atm. On the second time at 7 atm, the peak stress had been reduced from 121 ksi to 106 ksi, a reduction of 12 percent (Figure 28). It was not found easy to maintain convergence if complete unloading was attempted after foil deformation because of internal stresses remaining within the foil, which tended to pucker the foil near the rib centerline. The residual stresses were as high as 85 ksi. From this exercise, we conclude that pre-forming can indeed reduce peak foil stresses but that, in practice, the foil should always have positive pressure after pre-forming to avoid loss of position by puckering. Another disadvantage of pre-forming is the need for much additional strength in the foil support ribs, or additional support for these ribs while the pre-forming pressure is applied.

In practice, the strongest foils tend to have extremely low ductility (Section 2.2), so that the margin for deformation without loss of strength is very small indeed. In order to achieve the 12-percent reduction in peak stress discussed above, the maximum deformation was actually 1.6 percent, which exceeds the total ductility of Ti 15-3-3-3 foil (Section 2.2).

A further computation with measured foil material properties will be discussed in Section 4.3, where it is shown that the properties measured in a uniaxial geometry are not appropriate for the biaxial stress loading in a real foil application.



K9989

Figure 28. Peak stress on first and second loading cycles for 0.5 mil deformable Ti example.

### 3.5 DYNAMIC RESPONSE OF FOILS TO LASER PRESSURE PULSE

Immediately following the passage of the electron beam pulse through the foil two separate effects change the stress distribution in the foil:

- a) Electron energy loss in the foil causes a temperature jump in the free-span region of the foil, which is unshielded by the ribs, leading to a change of foil deflection because of thermal expansion.
- b) The electron beam energy deposited in the gas causes a temperature jump in the gas, which is initially at constant volume. The resultant pressure jump has a duration determined by the acoustic transit time of the inbound relaxation wave from unpumped regions of gas.

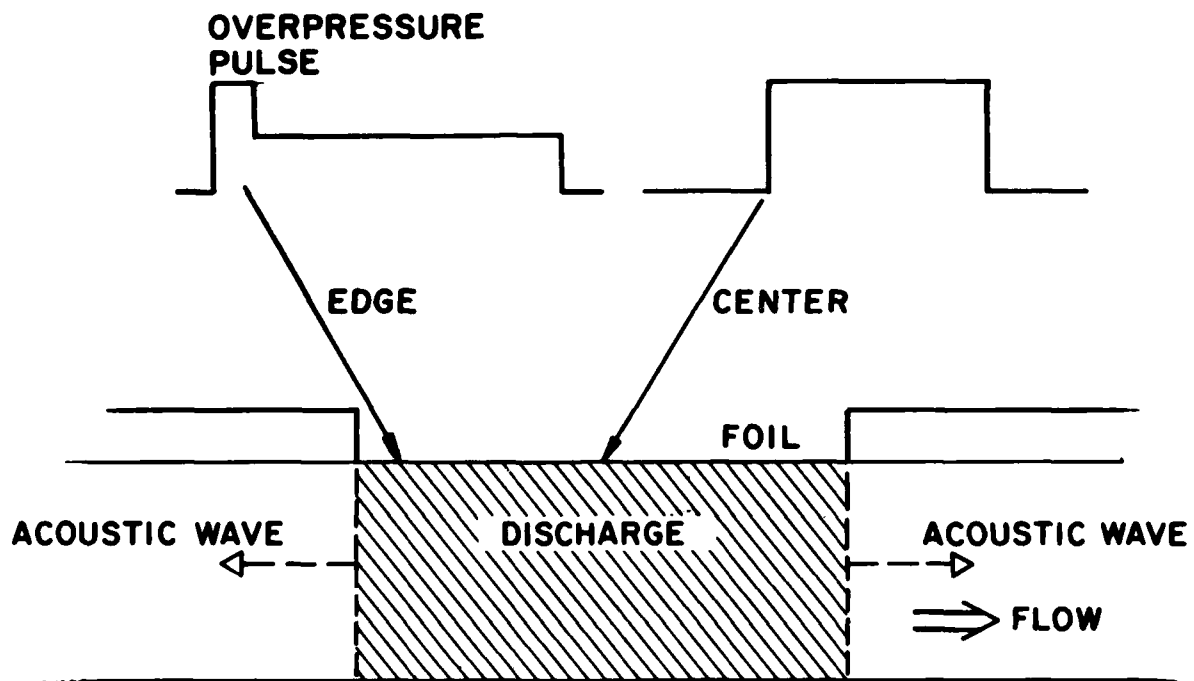
Of these two effects the biggest changes in stress are caused by (b). Although the increased foil deflection caused by (a) works to increase the bending stress, it is typically only  $< 0.3$  of the deflection because of the pressure pulse, and is not accompanied by an increase in membrane stress. In the remainder of this section, we discuss only effect (b), but an example of (a) will be described in the single-pulse movement measurement of Section 7.0.

The duration of the pressure overpulse and its time history depend on the foil location, as shown schematically in Figure 29. At an acoustic velocity of  $5 \times 10^4 \text{ cm sec}^{-1}$ , the pressure pulse clears a 10-cm foil face completely in 200  $\mu\text{sec}$ . However, the natural period of foil oscillation is  $\sim 20 \mu\text{sec}$  for typical foil spans and loadings, so that the foil executes at least 10 ringing cycles while the overpressure is present. Even after the pressure drops, the foil continues to ring, with a damping time determined primarily by the radiation of acoustic energy into the gas.

The sudden application of pressure causes the foil to move to a new equilibrium position, and an overshoot occurs if the pressure rises in a time  $\tau < T$ , the oscillation period. Classical theory for a linear single mode model<sup>(7)</sup> predicts that, for the following linear ramp load function,

$$\xi(t) = \begin{cases} \xi_c t/\tau & , 0 \leq t \leq \tau \\ \xi_c & , t \geq \tau \end{cases}$$

7. "Shock and Vibration Handbook," Vol. I, Chapter 8, Harris and Crede, (McGraw Hill, 1961).



K3116

Figure 29. Qualitative view of pressure history in a pulsed laser.

the response is

$$\frac{v_M}{\epsilon_C} = 1 + \left| \frac{T}{\pi \tau} \sin \frac{\pi T}{\tau} \right| \quad (3)$$

in which  $v_M/\epsilon_C$  is the ratio of peak deflection to equilibrium deflection (reached after late-time damping).

As an example, we have used the NASTRAN dynamic option to follow the application of a 1 atm, 1  $\mu$ sec linear ramp load increase to a foil loaded statically at 5 atm. The computed motion is shown in Figure 30, and the corresponding stresses in Figure 31. Here, because  $\tau/T \ll 1$ , the foil overshoots dynamically to a displacement which corresponds closely to that for a static 7 atm load, before executing oscillations with a period of 13  $\mu$ sec about the equilibrium 6 atm displacement.

The classical single mode theory predicts a ratio  $v_M/\epsilon_C = 2.0$  for this case, whereas the computed motion yields  $v_M/\epsilon_C = 2.14$ . This difference is caused by either the nonlinear constraints in the problem (foil-surface contact) or the presence of higher-order modes of oscillation. In an examination of the code output the presence of significant (> 10 percent) amplitude in higher modes was not detected.

In the application of a greater pressure impulse for 12  $\mu$ sec ( $\cong$  the ring period), slightly non-sinusoidal waveforms were observed (Figure 32), indicating that the problem becomes more non-linear for larger amplitude movements.

In a real situation, the foil oscillation frequency may be affected by the mass of gas adjacent to the foil, if it becomes significant relative to the foil mass. We may estimate when this effect is important by comparing the mass of gas over the foil free span out to 1 span depth, with the mass of the foil. For 0.5 mil Ti foil and Ne at 5 amagats, the mass ratio gas:foil = 0.23, for a 0.3-cm free span. This would be expected to increase the oscillation period by  $\sim$  11 percent, at a first estimate.

The last important parameter of foil movement is the damping constant. For movement in the elastic material regime, damping can occur by (a) acoustic radiation to the gas, and (b) acoustic radiation into the support rib structure, followed by damping at the ends of the ribs. Mechanism (a) alone leads to quite high rates of damping, and it probably dominates in practical situations.

FOIL TRANSIENT RESPONSE PLOT

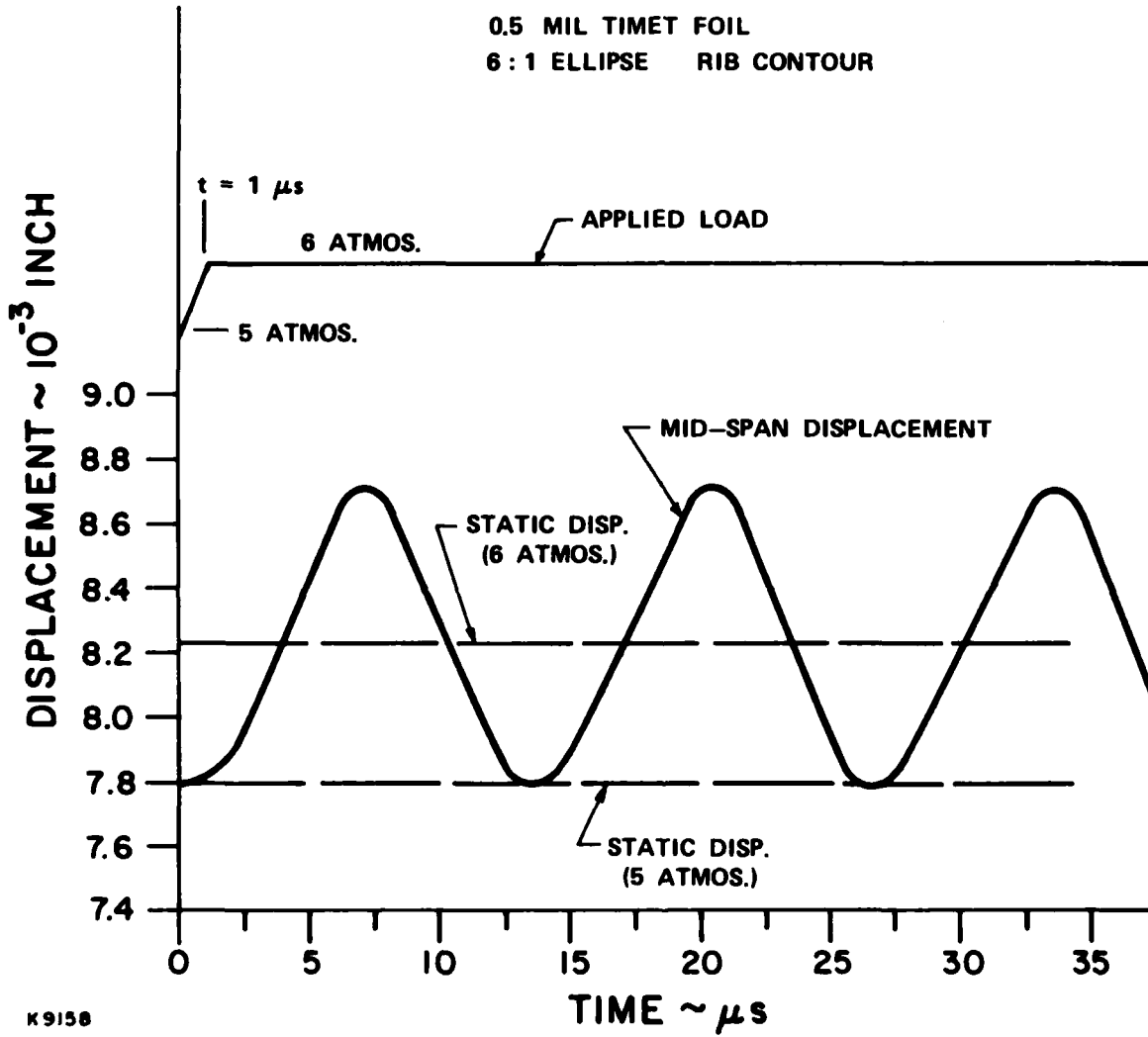


Figure 30. Dynamic response of 0.5 mil elastic Ti foil to  $1 \mu\text{sec}$ , 1 atmosphere pressure jump, 0.3 cm slot.

FOIL TRANSIENT RESPONSE

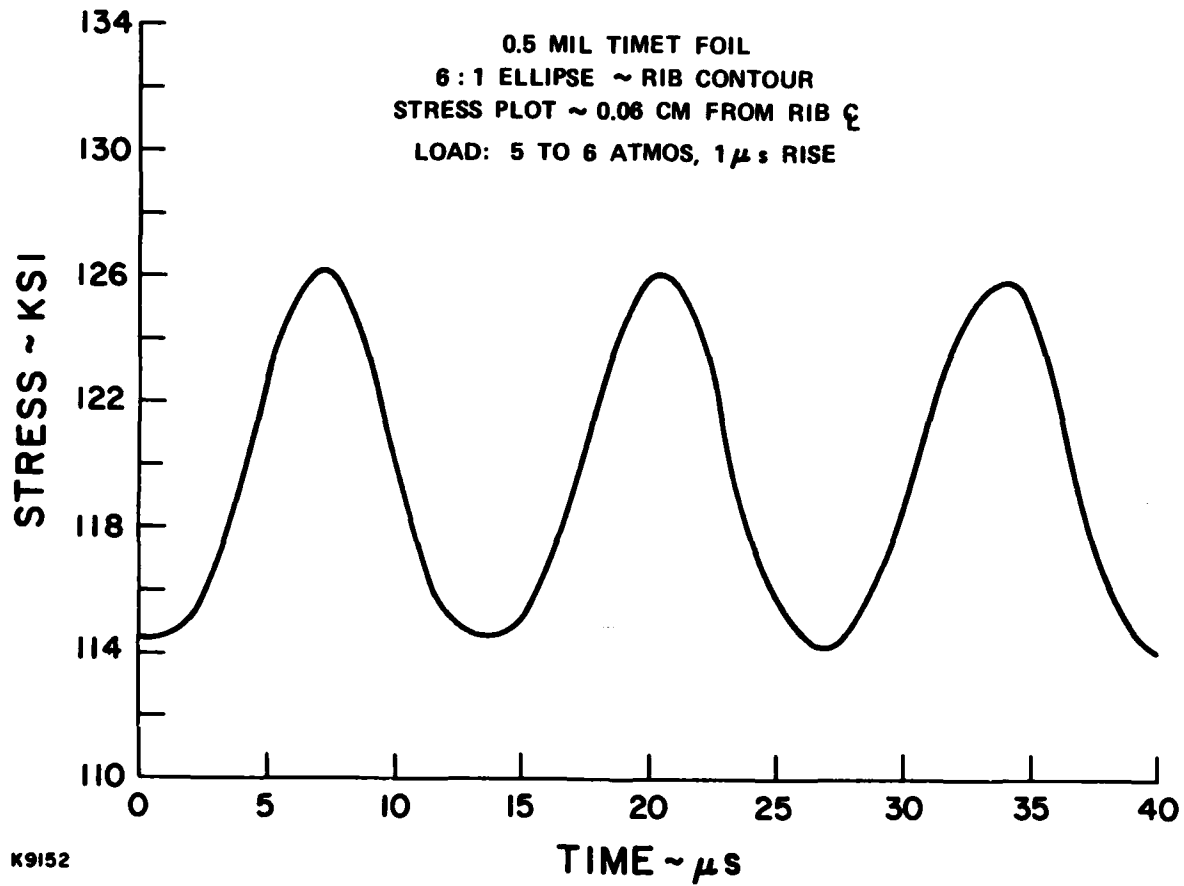
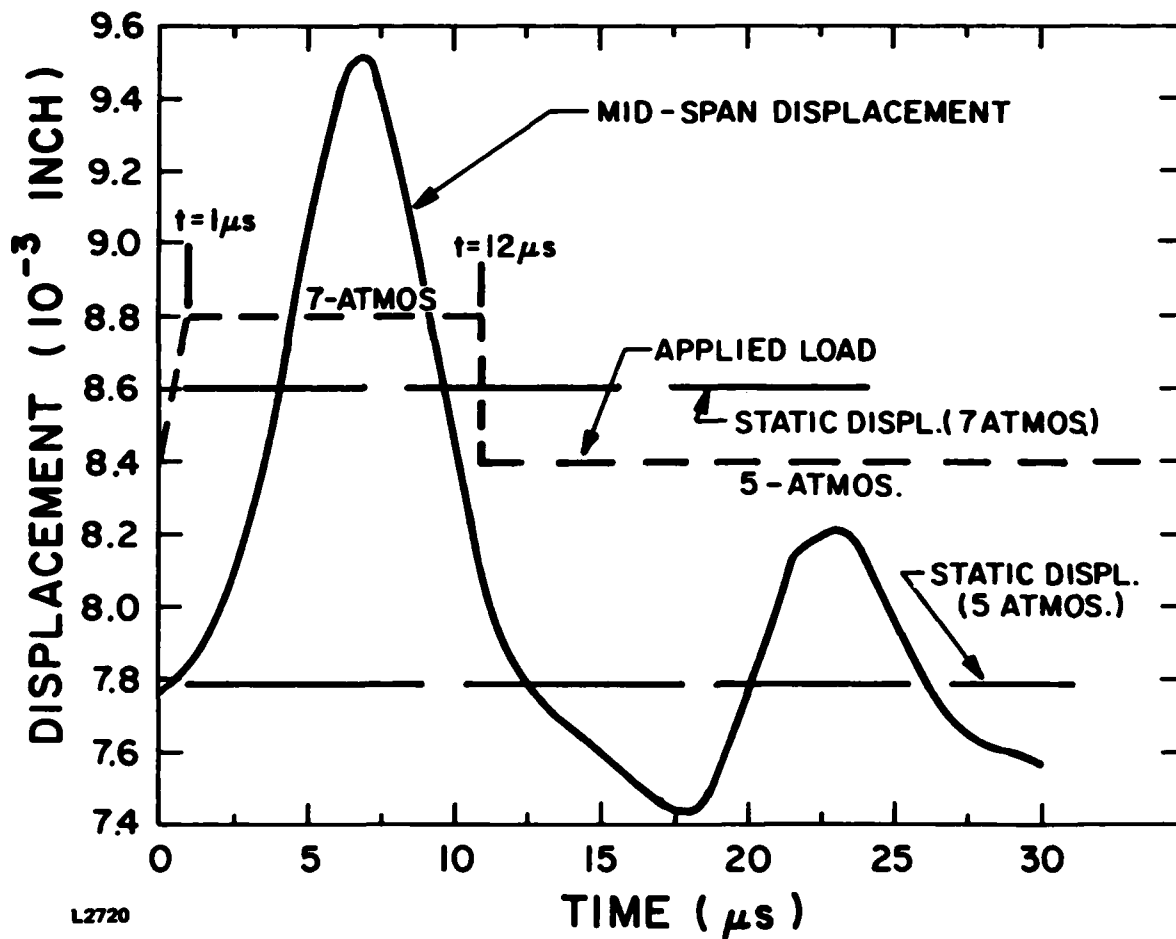


Figure 31. Peak stresses relating to the dynamic response of Figure 30.



L2720

Figure 32. Dynamic response of 0.5 mil elastic Ti foil to 12 $\mu$ sec, 2 atmosphere pressure jump, 0.3 cm slot.

The radiated acoustic power per unit area of a piston of peak speed  $u_0$  is

$$P_r = \frac{1}{2} \rho_c u_0^2 a_c \quad (4)$$

where  $a_c$  is the acoustic velocity in gas of density  $\rho_c$ , whereas the energy of oscillation of a foil of thickness  $w$  per unit area is

$$E_0 \cong \frac{1}{2} \rho w u_0^2 \quad (5)$$

The foil, therefore, radiates its energy in a characteristic time

$$\tau_r = E_0/P_r = \frac{\rho w}{\rho_c a_c} \quad (6)$$

For example, with Ne at 1 amagat and 0.5 mil foil  $\tau_r = 146 \mu\text{sec}$  and the acoustic damping for this case occurs in  $\sim 11$  foil oscillation periods.

To conclude this section on the dynamic modeling of foils, we note the following points:

- a) The foil overshoot in typical examples is well modeled by single mode, linear classical theory, as in (3) above.
- b) The foil oscillation is damped by acoustic radiation in a characteristic time given by (6) above.

## 4.0 BIAxIAL STRENGTH OF FOILS

### 4.1 DEFINITION OF BIAxIAL LOADING

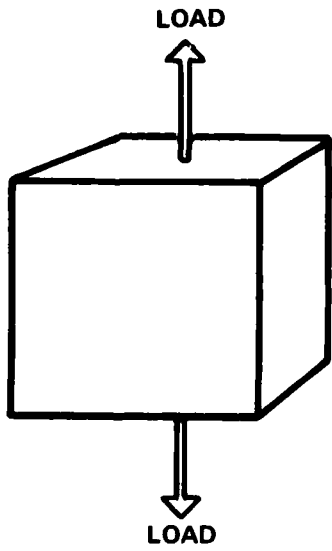
Figure 33 shows the application of uniaxial and biaxial stresses to a sample. Under uniaxial stress, the material can contract in thickness and in width whereas, under biaxial stress, the material can contract only in the thickness direction

For isotropic material, the application of equal biaxial stress components results in a  $\sqrt{2}$  increase in the yield strength whereas, for cylinder loading (two-to-one biaxial stress field), yield occurs at 1.15 times the uniaxial yield strength.

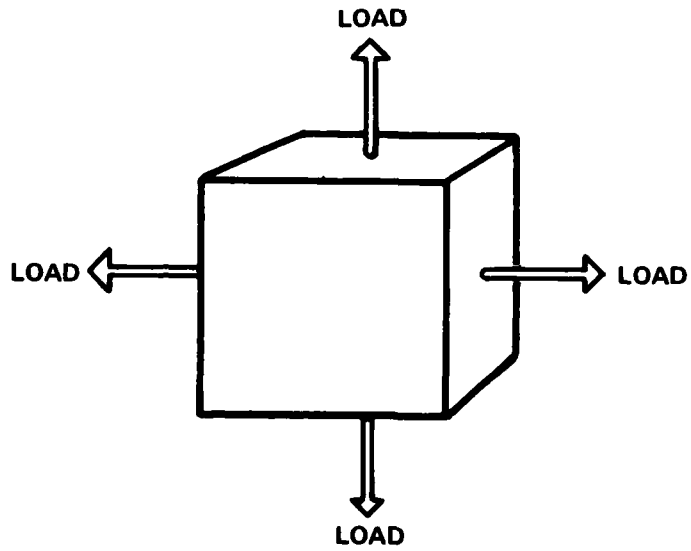
In previous work with rolled Ti alloys,<sup>(8)</sup> strong anisotropy has been observed in the thickness direction (i.e., the direction of compression during rolling). In measurements of the biaxial tensile ultimate strength (BTU) on 6 Ti alloys,<sup>(8)</sup> ratios of BTU/UTS of between 1.09 and 1.42 were measured, depending on the alloy, in 2:1 biaxial loading. The highest ratios were obtained for  $\alpha$ -type alloys and the lowest for  $\beta$ -type.

It is to be expected from the anisotropy of the foil crystal structure (Section 2.3) that substantial biaxial strength enhancement will occur in the CP Ti(4) and Ti 3-2.5 materials. The 15-3-3-3 material has a much more isotropic appearance, but is different from the other materials in that it has very few crystals (1-3) in its thickness and, therefore, might not have the freedom to deform in the thickness direction. As we shall see below, all the foil materials studied showed a large biaxial strength enhancement. This phenomenon was discovered in the course of a routine membrane burst test that was designed to correlate measured membrane failure with a prediction based on the stress calculations and measured material properties.

8. Deformation and Recrystallization of Ti and Ti Alloys, S.R. Seagle and H.D. Kessler, ASM/MEI Publication C27L5 (1968).



UNIAXIAL STRESS



BIAXIAL STRESS

K9985

Figure 33. Illustration of uniaxial and biaxial stresses.

## 4.2 BURST TEST AND RESULTS

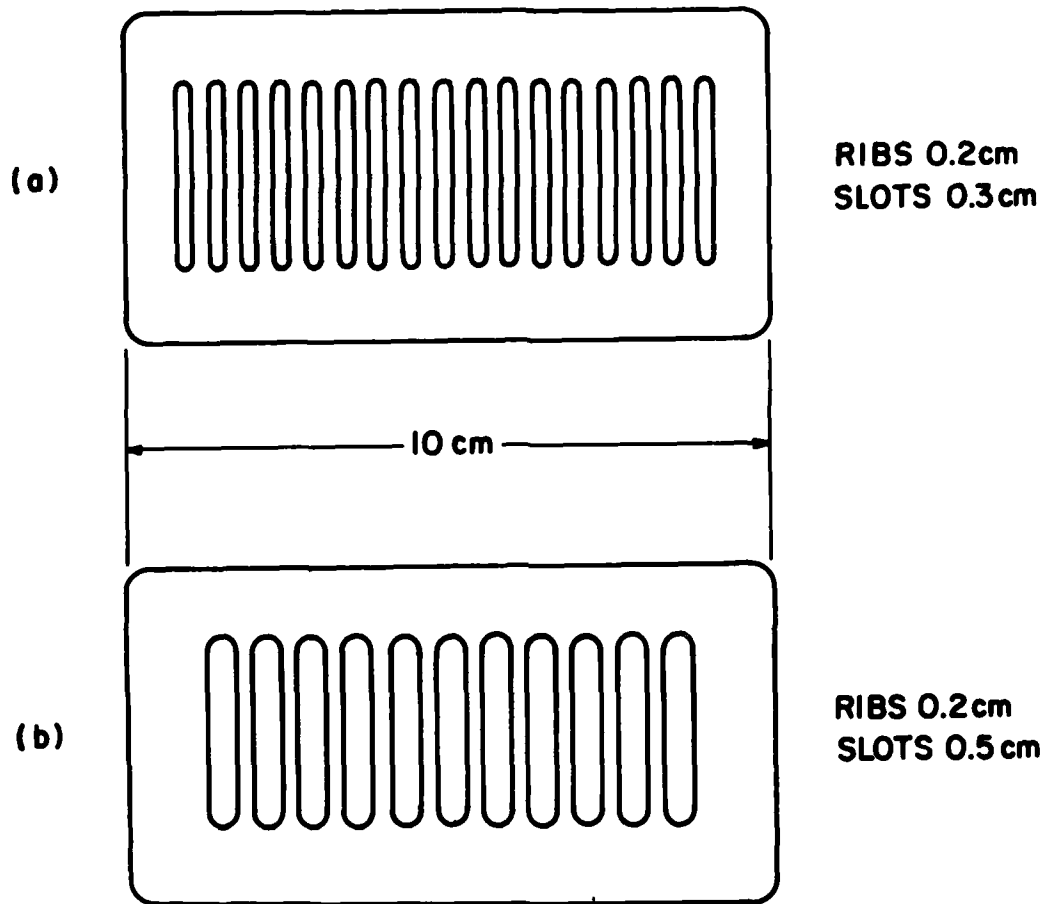
In the present tests foil material was held over a slotted frame that had a rib contour belonging to one or other of the generic shapes (Figure 17). The slot geometry is shown in Figure 34(a). Also shown in Figure 34(b) is the wider slot geometry used in later fatigue testing, but not used in the burst test. Rib contours were the 6:1 ellipse and the flat, radiused 0.05 cm.

The frames were machined out of stainless steel, special tools being cut for the contoured rib surface. As a test on the final rib surface shape impressions were taken of the ribs in either soft Al or butyl rubber, sectioned and examined under low magnification. Results for the 6:1 ellipse and radiused flat are shown in Figure 35. Other than a light rub with the finest emery cloth, these surfaces were used in the as-machined state. The elliptical contour was a good match to the design shape; however, the radiused flat had more gentle corners than the ideal shape (Figure 35). This is attributed to an error in the tool cutting, probably caused by lack of resolution at that scale size.

The slotted frame rested on a shallow steel box fitted with an O-ring seal, so that the foil on its frame formed the sixth side of the box. A static load of 10,000 lbs was applied to the box and frame by a hydraulic press so that the Ti foil sample was held at the edges by a load of ~ 1,200 lbs/in. This pressure was required to prevent any small degree of slippage, which could increase foil deflection and hence decrease the membrane stress for a given load. [The burst pressures showed a small increase (< 10 percent) if < 4,000 lbs of loading was applied.]

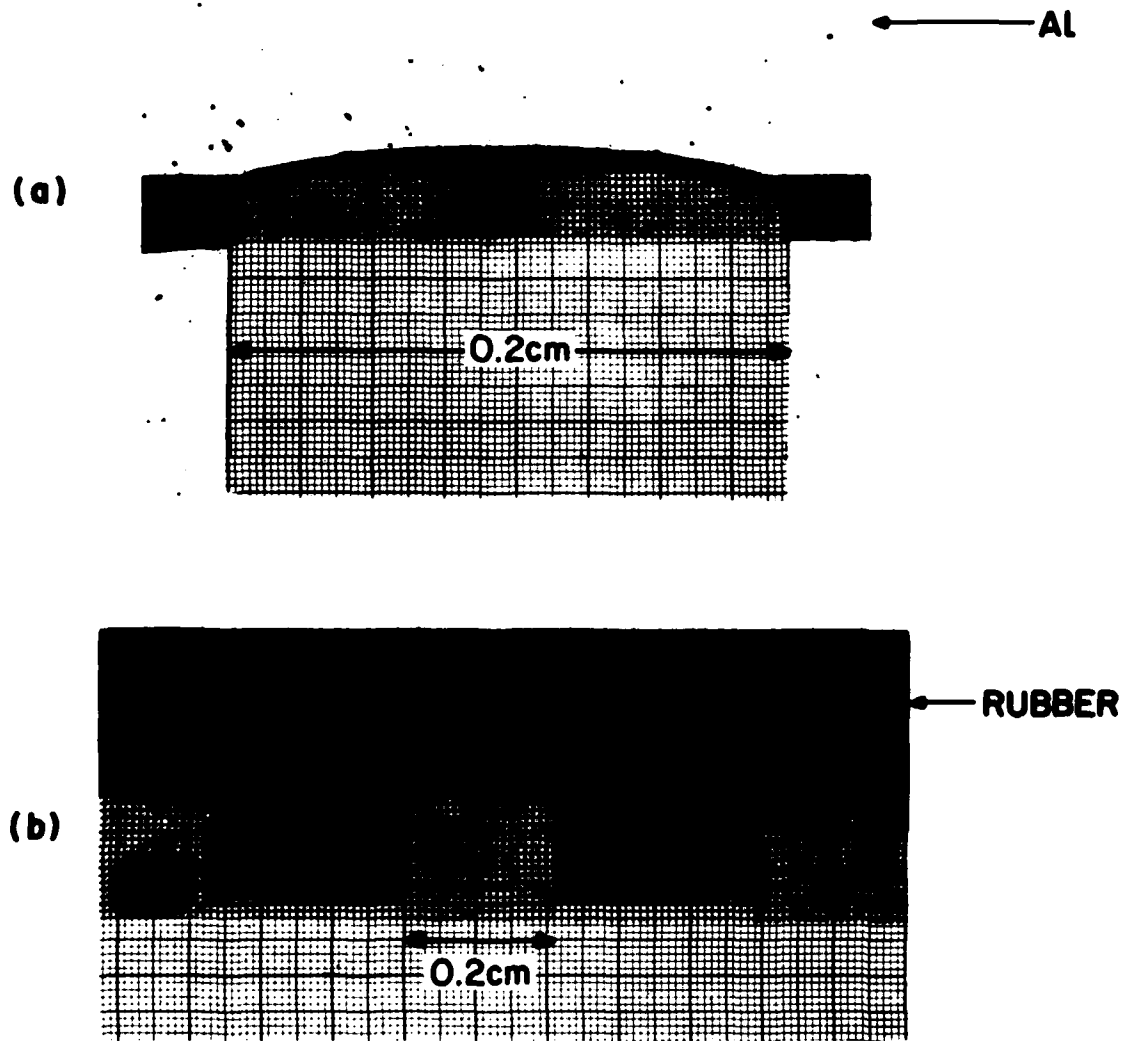
The foil loading was increased at the rate of  $< 2 \text{ psi sec}^{-1}$  by a gas line entering the box. The pressure of rupture was recorded. Gas loading was chosen because the anticipated burst pressures were < 400 psi, and the heavy press surrounding the test box would deaden the burst noise. Unfortunately the enhanced foil strength gave rather higher burst pressures than anticipated (400 to 600 psi), so that rather loud reports issued from some of the bursts. With hindsight, hydraulic loading would have been preferable.

Results from the burst tests are given in Table 6. Typically tests were performed on 6 samples, or more. The only foil material that gave really reproducible burst pressures was Ti 15-3-3-3 as rolled and strand annealed.



K9984

Figure 34. Plan showing test frame slot geometries: (a) 0.3 cm slot, (b) 0.5 cm slot.



K9983

Figure 35. Comparison of measured and ideal rib contours for (a) 6:1 ellipse, 0.3 cm slot frame, and (b) radiussed flat, 0.3 cm slot frame.

TABLE 6. BURST PRESSURES AND BIAXIAL STRENGTH ENHANCEMENT

Burst Pressures (psi)	Material			
	Cp Ti(4) 0.5 mil	Ti 3-2.5 0.6 mil	Ti 15-3-3-3 as Rolled 0.65 mil	Ti 15-3-3-3 aged 1000°F, 8 hr, 0.65 mil
6:1 ellipse 0.2cm rib, 0.3cm slot	560 ± 29 n=6	566 ± 16 n=9	551 ± 7 n=6	593 ± 65 n=4
radiused flat 0.05cm radius 0.2cm rib, 0.3cm slot	398 ± 67 n=10	423 ± 54 n=7	431 ± 15 n=8	520 ± 88 n=4
6:1 ellipse Calculated burst pressure based on uni- axial strength	343	421	291	615
Biaxial strength en- hancement factor	1.63	1.34	1.89	0.96

The least reproducible material was Ti 15-3-3-3 aged 1000°F, 8 hr. All of the failures were catastrophic with the exception of two samples (one CP Ti (4) and one Ti 3-2.5), which began to leak but did not burst. Each of the latter failures was at the low end of the range of burst pressures and seemed to be caused by material defects.

Also given in Table 6 are the computed burst pressures using the uniaxial material strengths measured in Section 2.0. The details of this calculation are given in the following section.

#### 4.3 MODELING OF BURST TEST USING UNIAXIAL STRENGTH

Modeling of the burst pressure is complicated by the entry of the material into the plastic regime well before the peak stress exceeds the UTS. One approach that was attempted was to use the NASTRAN code with real material (uniaxial) properties and ever-increasing loading. The other approach, which was more successful, was to model the material deformation by an effective modulus of elasticity in formulas (1) and (2) above, where the effective modulus refers to the stress and strain at the breaking point.

The NASTRAN code was used to model an actual burst test with, Ti 3-2.5, which was chosen because of its reproducible burst results and moderate ductility. As seen in Table 2, at 75°F this material had a 0.2 percent yield strength of  $132 \pm 1.4$  ksi (uniaxial measurement) and  $UTS = 142 \pm 1$  ksi. Its measured thickness was 0.60 mil. The burst test frame had a 6:1 ellipse rib of width 0.2 cm with a slot of 0.3 cm. Computed peak stresses at the rib and midspan location are shown in Figure 36. The average midspan stress, or membrane stress, is also shown. From this data, we note that, at the peak stress point (on the pressure side above the rib) the stress exceeds the material UTS at 14 atm, whereas the measured burst pressure is 37.7 atm. Once the UTS has been exceeded locally, the foil is expected to rupture catastrophically because an increasingly thin cross section has to support the full load. This prediction of 14-atm burst pressure follows from the use of the uniaxial strength. In order to predict a burst pressure of 37.7 atm, a higher material strength has to be assumed. Furthermore, assumptions have to be made regarding both the yield strength and the ultimate tensile strength. Because of the cost involved, we did not run the NASTRAN code with other sets of assumed

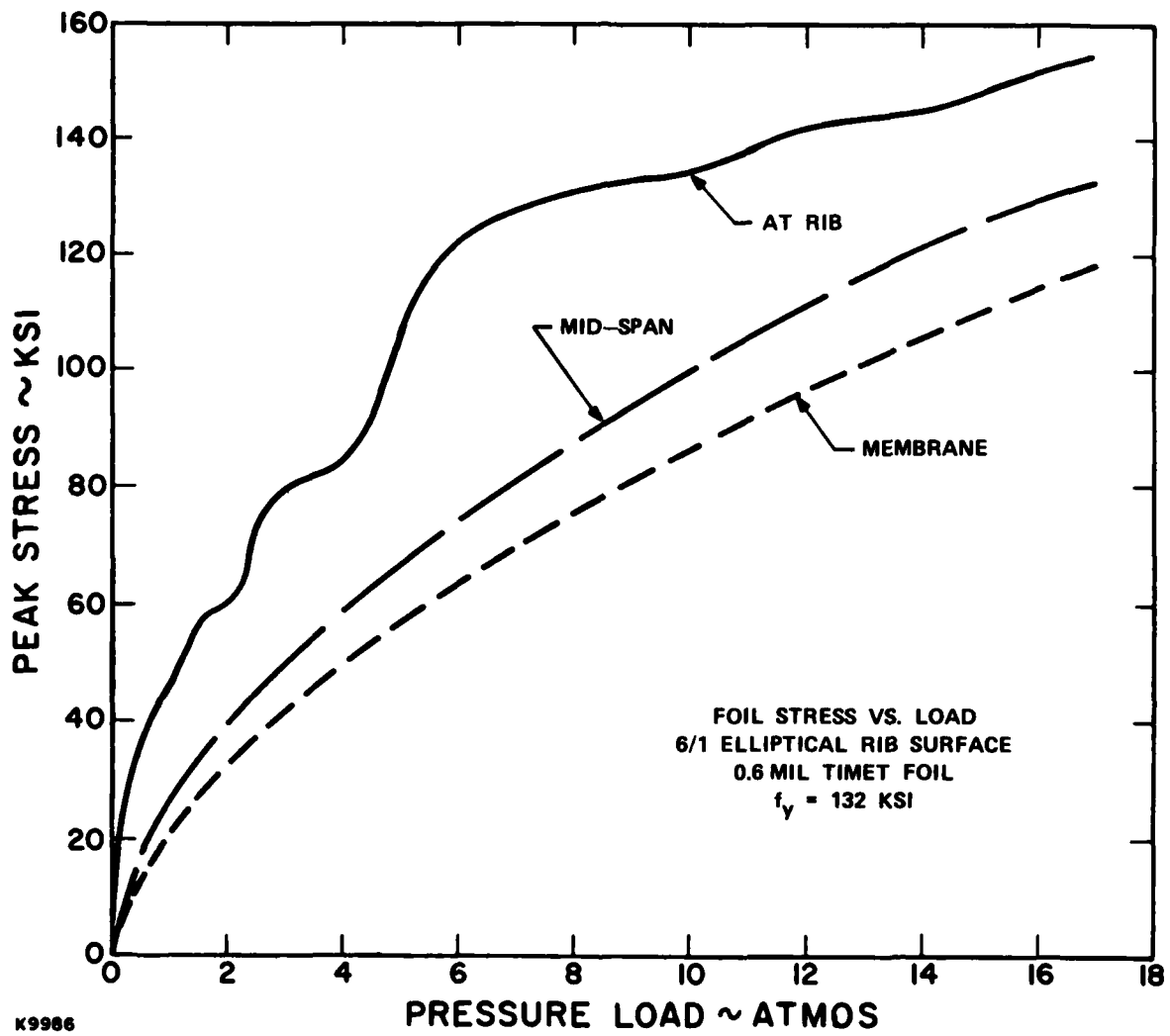


Figure 36. Computed stresses using measured properties of 0.6 mil Ti 3-2.5, 0.3 cm slot, rib ellipticity 6.

material parameters. However, an extrapolation was made from the data in Figure 36. If we considered the peak stress at the rib to be linear with load between 8 and 17 atm, then the peak stress at 37.7 atm loading was 210 ksi, and the implied biaxial strength enhancement was  $210/142 = 1.48$ . This extrapolation suffers from the implicit assumption that the 0.2 percent yield strength is 132 ksi, and, therefore, probably underestimated the strength enhancement.

A separate estimate of the strength enhancement was obtained from a calculation of the actual membrane stress. Because the membrane stress is critically dependent on the extent of material deformation, it is not enough merely to use the elastic deformation from formulas (1) and (2). If we approximate that the bending stress may be ignored relative to the membrane stress, and employ an effective elasticity given by

$$E_{\text{eff}} = \frac{\text{ultimate tensile stress}}{\text{strain at ultimate tensile stress}} \quad (7)$$

then we may derive the following expression for the burst pressure from (1) and (2),

$$P(\text{burst}) = \frac{4.9F^{3/2}}{\ell} \left( \frac{1}{E_{\text{eff}}t} \right)^{1/2} \quad (8)$$

in which  $F$  is the membrane force (lbs) at rupture, (i.e.  $F = \text{UTS}$ ,  $t$  is the foil thickness (in.) and  $\ell$  is the free span (in.).

From Eq. (8), we generate the line of computed burst pressures in Table 6, using the measured uniaxial  $F$  and  $E_{\text{eff}}$  values from the data in Section 2.0. With one exception, we note that the computed burst pressure is much less than the measured one. Furthermore, the use of (7) gives a high value for the computed burst pressure, because bending stresses do make a contribution, and the allowable membrane stress is therefore not as great as the UTS, which was the assumption.

Clearly the use of uniaxial strength data does not describe the measured burst pressures. We, therefore, ask: what modification is necessary to material properties to explain the data? On the assumption that material rupture

is related to strain we give equal strain to the uniaxial and the biaxial ultimate stress point. In formula (8), therefore, the effective modulus  $E_{eff}$  is proportional to the ultimate tensile strength,  $F$ , and the burst pressure scales linearly with  $F$ . The bottom line in Table 6 gives the pressure enhancement ratio, which, in the light of the above, we interpret as the ratio of biaxial ultimate tensile stress to uniaxial ultimate tensile stress.

For the highly anisotropic structures of CP Ti (4) and Ti 3-2.5 the enhancements are similar in magnitude to those obtained in reference (8). However, the as-rolled Ti 15-3-3-3 shows an extraordinary enhancement of 1.9, which is not obviously related to anisotropy when the crystallography of Section 2.0 is considered. By contrast, the aged Ti 15-3-3-3 shows no enhancement but its very high burst pressure has a large variability, which indicates that some other factor is at play - possibly the extremely low material ductility causing high stress at localized contact points with the rib. The other very low ductility material, CP Ti (4), also showed a large scatter.

At present, we can only speculate that the biaxial strength enhancement in as-rolled Ti 15-3-3-3 is related to its large  $\beta$  crystal scale relative to the foil width, which is in some way conferring on the foil some of the strength that would be found in single crystal material. Further investigation is needed.

Although we have referred to biaxial strength, we are not able to compute the biaxial stress ratio in foil-loading without a 3-D model. The present NASTRAN simulations are 2-D and it is apparent that the cost of going to 3-D would be very high. For slots with rounded ends, like those we have used, the analogy with a cylinder with spherical endcaps would suggest that the biaxial stress ratio is  $\sim 2:1$ , with the greatest stress perpendicular to the ribs.

In conclusion, measurements of the biaxial strength of Ti foils by means of a static burst test have shown considerable stress enhancements over the uniaxial foil strengths measured in Section 2.0. Already, as seen in Table 4, the foil uniaxial strengths substantially exceed bulk material strengths in most cases, so that total strength enhancements (over bulk material) are, at 75°F,

CP Ti (4)	3.0
Ti 3-2.5	2.1
Ti 15-3-3-3 (as-rolled)	1.8
Ti 15-3-3-3 (aged 1000°F, 8 hr)	1.1

#### 4.4 TENTATIVE DESIGN METHOD

In the following section, an experiment is described in which foils are loaded by a static pressure and subjected to repetitive overpressure pulses in a simulation of laser conditions. The stresses in the test foils can be modeled using the biaxial material properties of the previous section, which apply at 75°F. The 0.2 percent yield strength and the ultimate tensile strength values of Table 2 should be multiplied by the biaxial strength enhancement factors of Table 6, and used in the usual NASTRAN calculation. Because the enhanced yield strengths are so high, many useful foil load conditions do not even begin to yield the foil material.

A sensitive indicator of the accuracy of the calculation is its prediction of the pressure at which "dimpling" of the foil is first seen (i.e., permanent deformation observed on removal from the frame). The 15-3-3-3, 0.6 mil as-rolled material has an enhanced yield strength of 209 ksi and the pressure that can be applied on the 6:1 ellipse rib (with 0.3 cm slot) before this stress is reached anywhere in the foil is 135 psi, according to elastic foil calculations. Experimentally, dimpling is first observed at ~ 115 psi for this material. This is in good agreement with the calculation, indicating, by a different means, that there is a large biaxial yield strength enhancement.

## 5.0 CYCLIC PRESSURE SIMULATION

### 5.1 INTRODUCTION

The central experimental effort in the present program was the design, construction and operation of a novel rig to simulate laser impulsive pressure loading on foils. The nature and approximate magnitude of laser pressure pulses is discussed in Section 3.5, and experimental data is mentioned in Section 7.0. Any simulation has to have an equivalent movement to the ringing motion that follows a sharp pressure transient (Section 3.5). The most direct simulation consists of the application of a pressure jump with a risetime shorter than the ring period. When possible methods of achieving this are considered, only one stands out as being simple in concept and giving complete flexibility in the choice of foil to be tested: pressure generation by the magnetic self-force of a pulsed current-carrying conductor, and its subsequent transmission to the foil through a layer of liquid. The only disadvantage that this suffers from is that the foil ringing frequency is reduced by the liquid loading to approximately 7 times less than it would be in the real gas-loaded situation. An alternative that was seriously considered was to utilize the magnetic force on a current through the foil itself, situated between the magnet poles of a strong electromagnet. This suffered from two principal difficulties: the Ti foil would have had required to be copper, or silver-coated to carry the large currents needed; and cooling of the foil would have been difficult to achieve in the confined space between the magnet poles. In either case, it was not clear that conductive coatings would maintain their integrity under the cyclic fatigue conditions of the test.

In practice, the choice of method has proved to be a success, with continuous day and night operation proving practicable. In the following two sections, we discuss, first, the design of the machine and then its performance. Foil tests are described in Section 5.4 and a correlation with the sinusoidal fatigue data of Section 2 is made in Section 5.5.

## 5.2 DESIGN OF PRESSURE PULSE RIG

The design parameters that we worked to were:

Overpressure	}	amplitude	15 psi
		rise time	10 $\mu$ sec
		duration	20 $\mu$ sec $\gg$ 100 $\mu$ sec
Static Pressure			0 $\gg$ 200 psi
Repetition Frequency			0 $\gg$ 1 kHz
Temperature Range			20°C $\gg$ 200°C
Foil Test Area			25 cm <sup>2</sup>

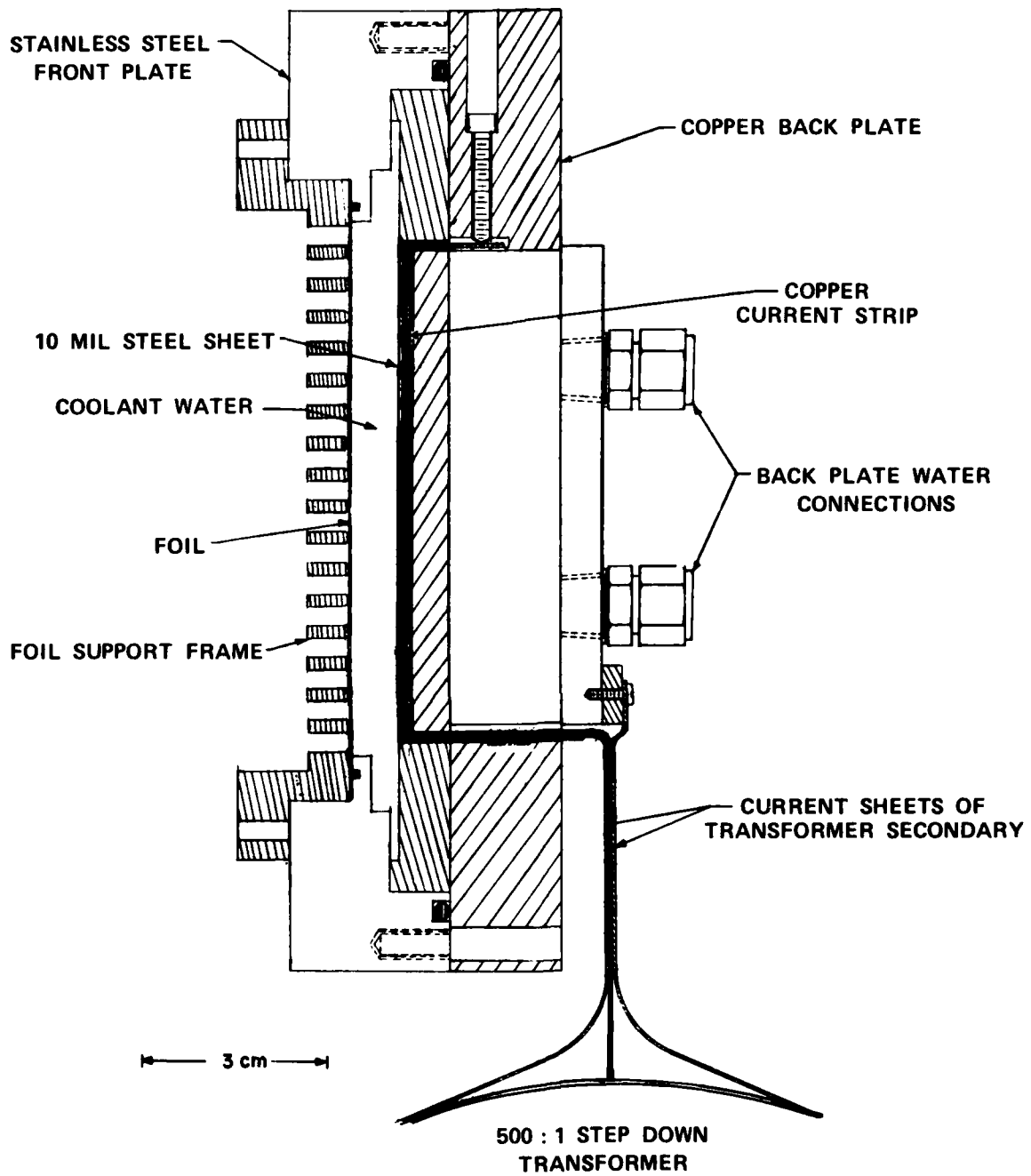
The force per unit area between two infinite current sheets of  $J$  A m<sup>-1</sup> surface current density is

$$F = \frac{\mu_0 J^2}{2} \text{ Nm}^{-2} \quad (9)$$

For 15 psi overpressure, we require  $J=4 \times 10^5$  Am<sup>-1</sup>. In order to have the lowest current, the test area was elongated to a 3:1 aspect ratio, with the current travelling lengthwise, so that a final current-carrying strip of 3 x 8 cm was chosen, implying the need for a 12-kA current pulse.

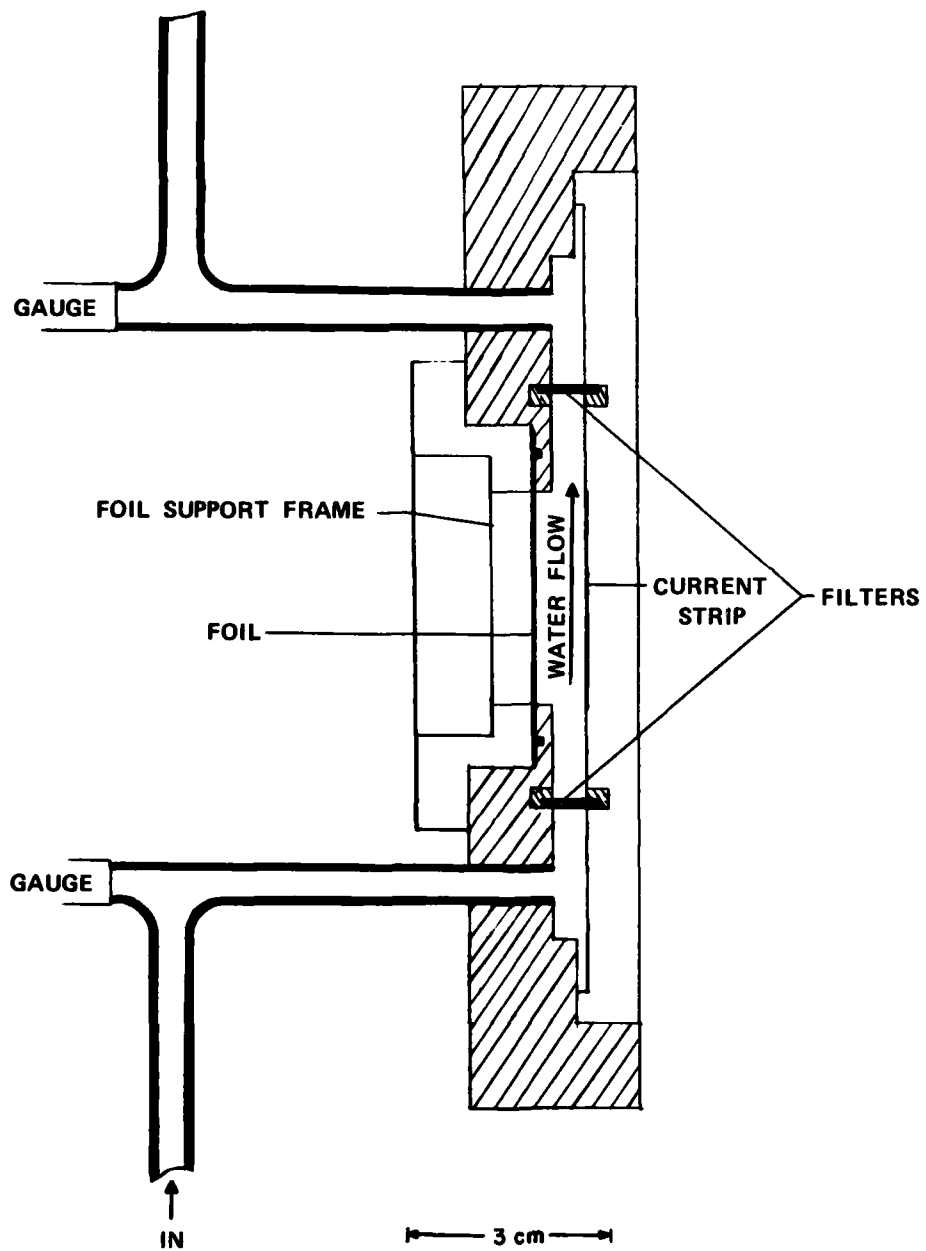
The current-carrying strip was made of 20-mil copper and formed part of the secondary circuit of a pulse transformer, as shown in Figure 37. It was spaced by 20 mil from a solid copper backplate by a fine woven glass ribbon that gave electrical insulation, and was porous so that the  $\sim$  1 mil movement of the current strip was not impeded by the elasticity of air. The copper strip was in direct contact with a 10-mil stainless-steel membrane, which was an integral part of the water jacket, being welded to the interior steel plate (Figure 37). This membrane served to transmit the pressure pulse while keeping water away from the current strip. A horizontal section is shown in Figure 38.

The power dissipation in the transformer secondary, including the current strip, was one of the most important design considerations. This was handled by having a rapid flow ( $\sim$  3 m sec) of cooling water between the foil and the steel membrane. Additional water cooling was applied to the back plate, and water-cooled plates were also clamped around the secondary sheets



K9452

Figure 37. Vertical section of cyclic test rig.



K9453

Figure 38. Horizontal section of cyclic test rig.

with 500 turns of 22 gauge copper wire, and on the secondary with a single copper sheet (20 mil thick). In order to drive the primary current of 25 A through this length of wire, the primary voltage has to be 13 kV. Adequate high voltage insulation is provided between primary and secondary.

The current transformer is driven by a valve modulator, which gates the current from a 1  $\mu$ F storage capacitor. A parallel pair of EIMAC model 3 CPX 1500A7 tubes are used, being switched by the output from a COBER pulse generator (Figure 39). The entire assembly of valves and transformer is mounted in oil for voltage insulation and cooling. The oil is circulated through a heat exchanger, and cool returning oil is directed at the transformer secondary and the valve heads. The operation of this modulator has been completely reliable.

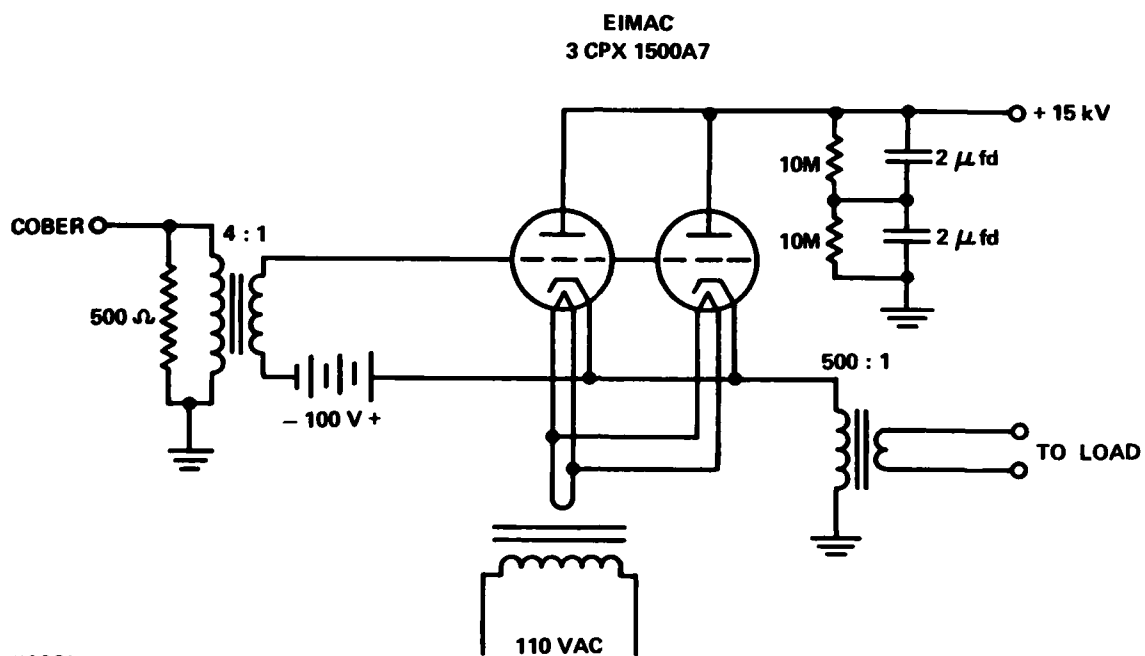
### 5.3 PERFORMANCE OF PRESSURE PULSE RIG

The current and voltage output of the modulator conformed generally to expectation. The secondary voltage waveform is shown in Figure 40, along with the primary current. The secondary current is difficult to measure directly, but in the present circuit is obtainable from the primary current and the turns ratio. The pulse duration was variable between 20  $\mu$ sec and 100  $\mu$ sec, although 50  $\mu$ sec pulses were found to be the most effective in producing large foil deflections.

The effectiveness of the pressure pulser was derived from our measurements of foil deflection. We did not measure the pressure jump directly with a transducer (which might have been possible, although difficult). Rather, we measured foil deflection by interferometry, as described in Section 6.0. The deflection is the most direct indicator of the stress cycle that the foil is subjected to, if the previous modeling apparatus is applied.

Foil midspan displacement was measured at 30 Hz as a function of pulser current for Ti 15-3-3-3 as-rolled foil (Figure 41). The test was on a 6:1 ellipse, 0.2 cm rib and 0.3 cm slot geometry, with a cell static pressure of 75 psi. First, we note that the displacement follows an  $I^2$  law, as it should do for < 1 atm pressure increments above 5 atms (Figure 25). The magnitude of the peak displacement at 12.5 kA would correspond to a static pressure increment  $\Delta p = 3.0$  atm (Figure 25). However, the foil is observed to

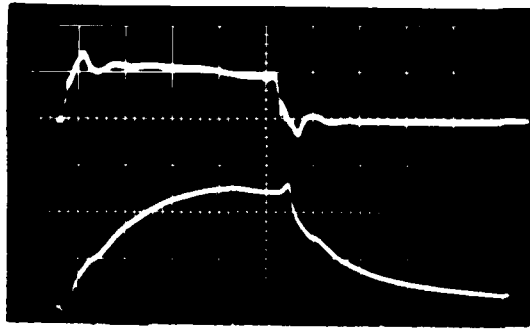
PULSER FOR MAGNETIC FOIL TESTER



K9981

Figure 39. Circuit of cyclic test rig modulator.

CYCLIC TEST STAND VOLTAGE AND CURRENT WAVEFORMS



SECONDARY VOLTAGE  
WAVEFORM

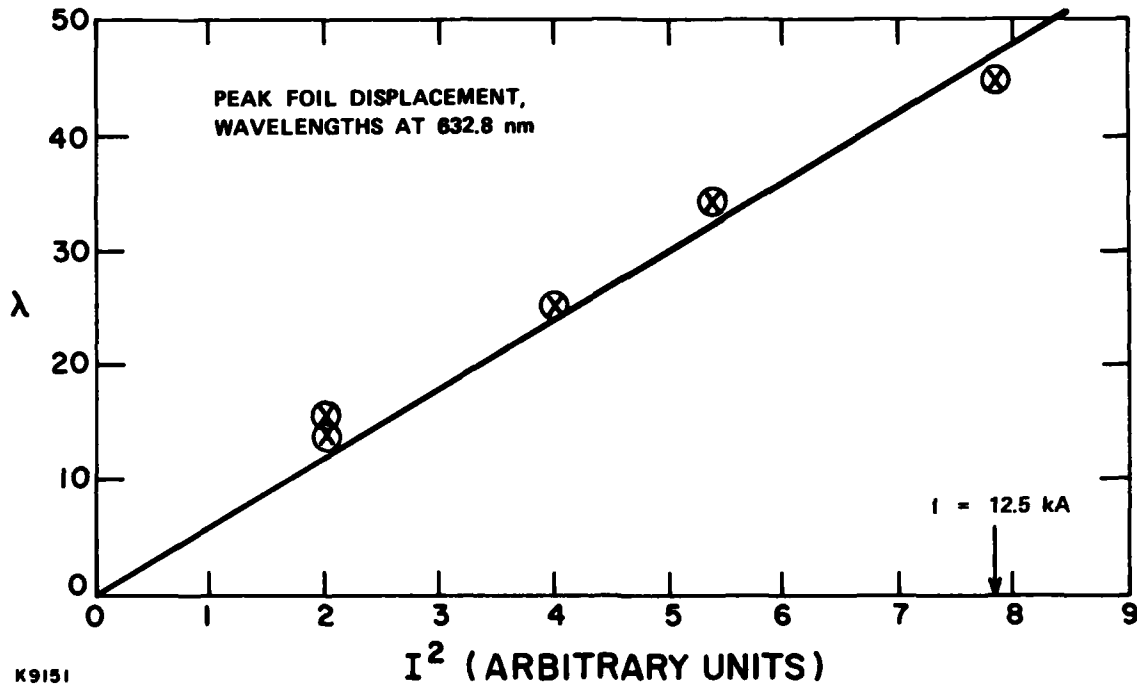
PRIMARY CURRENT  
( $\cong$  5 kA/div ON  
SECONDARY)

TIME  $10\mu$  sec/div  $\rightarrow$

K9131

Figure 40. Current and voltage waveforms on test rig.

DISPLACEMENT OF FOILS ON TEST STAND  
VS. (CURRENT)<sup>2</sup>, 50 μSEC PULSE



K9151

Figure 41. Measured foil displacement as a function of current.

begin a ringing motion (Figure 42) in which the peak deflection can be as much as 2.1 times the final static deflection. The probable static equivalent pressure jump is therefore only  $3.0/2.1 = 1.4$  atm, or 21 psi. Given the many acoustic possibilities for reflections and structural resonances, this figure is in moderately good agreement with the predicted 15 psi overpressure from a 12 kA pulse.

It was noted that the displacement amplitude increased for increasing pulse duration between 20  $\mu$ sec and 50  $\mu$ sec, but ceased to increase beyond 50  $\mu$ sec. This, in addition to the non-sinusoidal foil movement sometimes observed (e.g., Figure 42), indicates that possibly a structural resonance is complicating the response.

In a separate displacement measurement on the 6:1 ellipse, 0.2 cm rib, 0.5 cm slot frame, movements of up to  $55 \lambda$  were observed at 30 Hz, and the foil motion was much more regular (Figure 43). From equation (1) in the elastic regime the foil displacement is proportional to  $\lambda^{4/3}$ , where  $\lambda$  is the free span. Comparison with an applicable code run shows that the movement in Figure 43 corresponds to a pressure increment of 14 psi.

As noted above, the displacement decreased with increasing repetition frequency. The range between 30 Hz and 100 Hz is shown in Figure 44 for two drive voltages (data refers to Ti 15-3-3-3 on 6:1 ellipse, 0.3 cm slot frame). The cause of this decrease was probably increased resistance in the current strip caused by the higher dissipation. Because the effect was almost absent at 7 kV, when the dissipation was four times less, the possibility of the effect being related to acoustics is ruled out. Although this effect is a nuisance, it does not prevent tests with  $\Delta p = 15$  psi at 30 Hz. To improve upon this repetition frequency would require a redesign of the test head and possibly the introduction of cryogenic cooling.

By operation at frequencies lower than 30 Hz, the pressure increment could be increased. At 10 Hz, where some of the following data was taken, and with an increase of the drive voltage to 16 kV, we were able to generate pressure jumps of  $\sim 22$  psi.

Two measurements were made of the decay of the ringing movement. On the 0.3 cm slot frame, the  $1/e$  decay of the displacement amplitude occurred in 9 cycles. On the 0.5 cm slot frame it occurred in 14 cycles. These damping

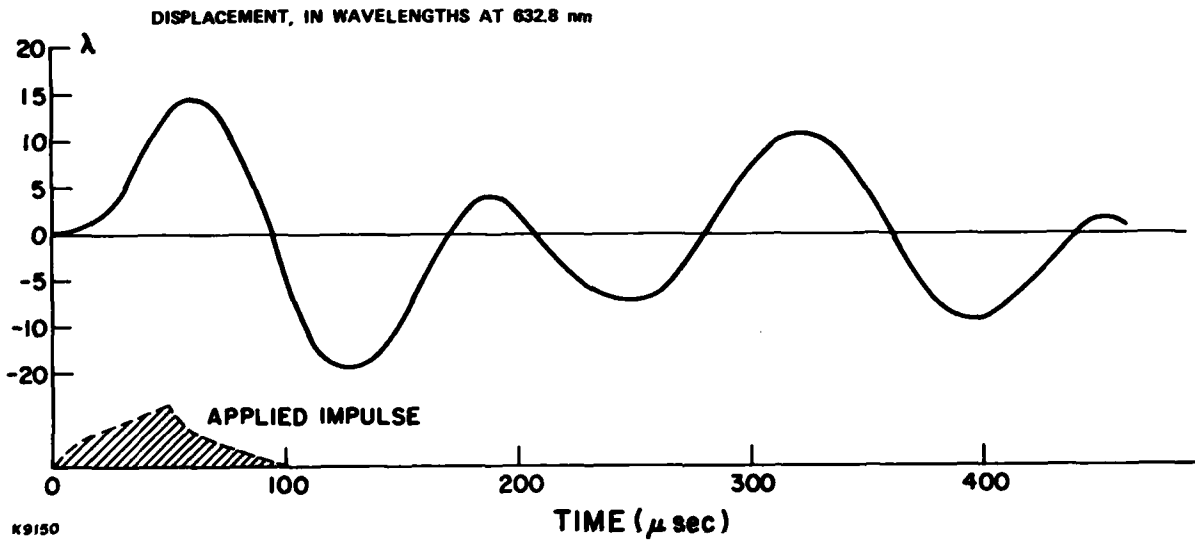


Figure 42. Measured foil displacement as a function of time, 0.3 cm slot.

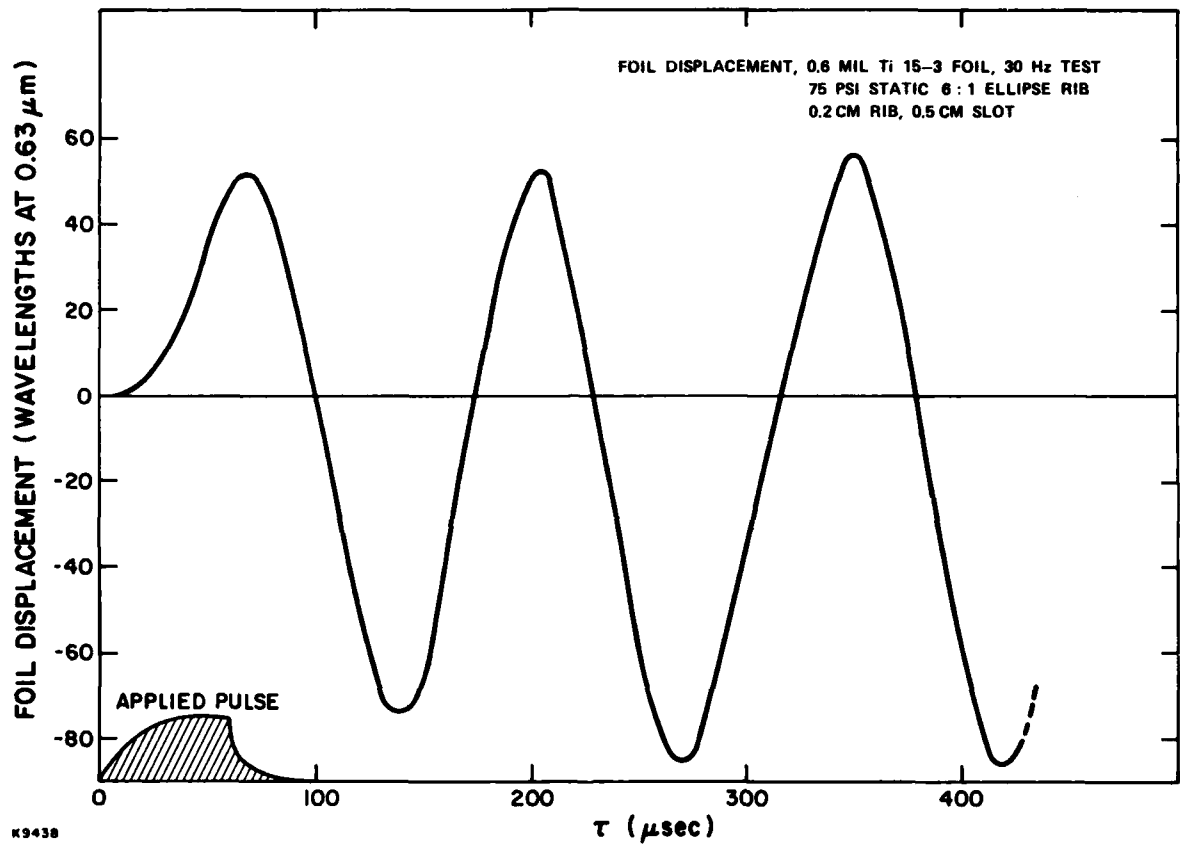


Figure 43. Measured foil displacement as a function of time, 0.5 cm slot.

MEASURED DISPLACEMENT OF 0.6 MIL TI FOIL ON 6:1 ELLIPSE FRAME

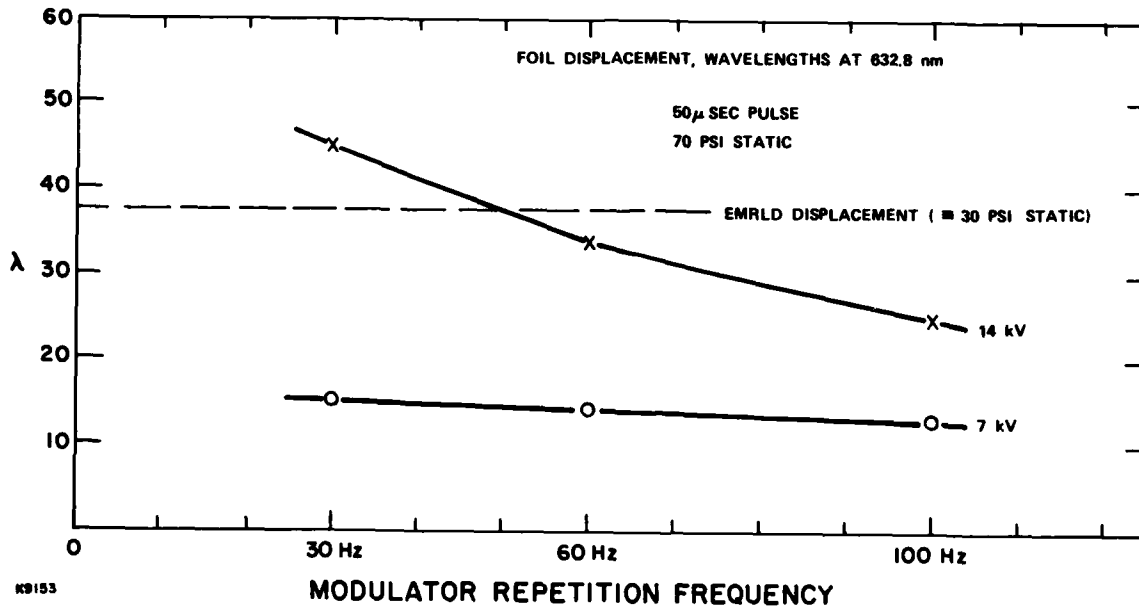


Figure 44. Foil displacement as a function of pulse repetition frequency.

rates are comparable to those in the gas-loaded foil of high-pressure excimer lasers (Section 3.5), but the resemblance is merely coincidental. Although the number of oscillations is similar, the oscillation frequency is about 7 times less in the liquid-loaded case.

#### 5.4 FOIL TESTS ON THE CYCLIC PRESSURE RIG

Initial tests were on the 6:1 ellipse, 0.3 cm slot frame. When it appeared that Ti 15-3-3-3 was exceeding  $10^7$  cycles routinely on this frame the tests were extended to a wider, 0.5 cm, slot. In each case the support rib width was 0.2 cm.

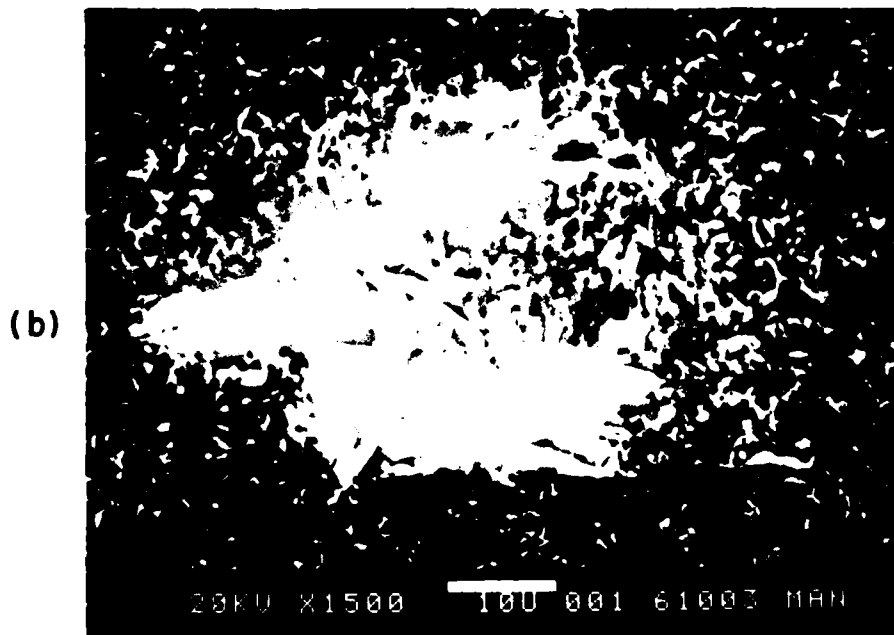
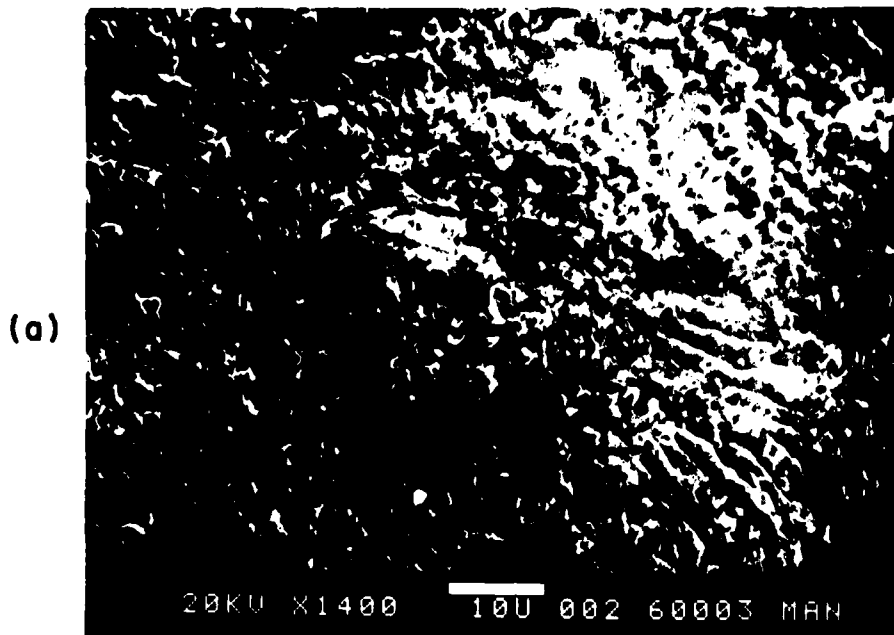
The test data for the 0.3 cm slot is listed in Table 7. Only two failures were observed, both caused by large ( $> 1$  mm) cracks at the point of maximum stress near the rib edge. Failures were not observed in further tests at the same and higher static pressures, although on a number of samples small fatigue "spots," visible to the naked eye, were observed either over the rib or right at the rib edge. These spots have been examined on the scanning electron microscope and constitute areas of  $\sim 100$   $\mu\text{m}$  diameter in which there is a profusion of fatigue cracks on the pressure side and evidence of small ( $< 10$   $\mu\text{m}$ ) grains of  $\text{Al}_2\text{O}_3$  at a damage site directly opposite, on the rib side (Figure 45). They apparently are associated with the presence of abrasive dust particles between the foil and the rib. The crack failures that did occur (tests 1 and 2) showed characteristic "feather-like" fatigue crack growth surfaces, as exemplified in Figure 46.

In tests 1 and 2, particularly, a brown discoloration was noted on the areas of the foil that had been in contact with the support rib, specifically the lines of intermittent contact at the rib edge. The support frame was 304 stainless steel, so that we attribute the discoloration to the presence of iron oxide. Tests 1 and 2 were conducted at a time of high humidity so that it is possible that the water-cooled foil attracted some condensation and that galvanic corrosion was taking place. Later tests showed much less discoloration or none. It is possible, but has not been proved, that, in tests 1 and 2, fatigue was enhanced by corrosion, thus explaining the early failures. An examination of test specimens 1 and 2 revealed small areas of etching in the

TABLE 7. CYCLIC PRESSURE TESTS ON 6:1 ELLIPSE, 0.3 cm SLOT, FRAME

Material: Ti 15-3-3-3 as rolled, 0.65 mil  
 Current pulse duration 50  $\mu$ sec  
 Repetition Frequency 30 Hz  
 Voltage 14 kV  
 Overpressure  $\Delta p = 15$  psi

Test No.	Static Pressure (psi)	Over-Pressure (p.s.i)	Np. of cycles ( $10^7 =$ runout)	Failure Mode	Fatigue Spots (e=edge of rib (r=above rib)
1	95	15	$1.0 \times 10^6$	crack	1e
2	95	15	$9 \times 10^4$	crack	2e
3	95	15	$>10^7$	-	0
4	95	15	$>10^7$	-	1e
5	115	15	$>10^7$	-	1e
6	115	15	$>10^7$	-	1r
7	115	15	$>6 \times 10^6$	-	4e
8	75	15	$>10^7$	-	0
9	75	15	$>10^7$	-	0



L2336

Figure 45. Scanning electron micrograph of a typical fatigue spot: (a) pressure side, (b) rib side, showing alumina particles.



K9444

Figure 46. (a) Fatigue-induced crack on one of the two probable stress-corrosion cases, showing feather-like growth. (b) Detail of a corrosion spot at the rib edge of this case.

discolored zone (Figure 46), which did not resemble the other fatigue spots mentioned above, and indicate that corrosion could have been the cause of early failure in tests 1 and 2. In Figure 47, the corrosion markings at the rib edge are shown for test 1, and position of the failure crack near the rib edge is seen.

Because of the lack of catastrophic foil failures on the 0.3 cm slot frame, testing was begun on the 0.5 cm slot frame, initially under less severe pressure conditions. Tests 10, 11 and 12 (data in Table 8) showed no failure or fatigue spots; therefore, a new and more severe testing condition was employed for tests 13 to 27. By reducing the repetition frequency to 10 Hz and increasing the drive voltage to 16 kV, an overpressure of 22 psi (extrapolated) could be applied. The reduced test frequency would have necessitated 12 days for each  $10^7$  cycle runout, so a  $10^5$  cycle runout was adopted, taking 2.8 hours per test. Reference to the room temperature fatigue data of Section 2.0 shows that for all materials the  $10^5$  cycle fatigue strength is less than 10 percent greater than the  $10^7$  cycle strength, so that a very good indicator of  $10^7$  cycle performance is obtained at  $10^5$  cycles (provided that the mechanism is similar between the present fatigue and the 30 Hz sinusoidal fatigue of Section 2.0 - a point further discussed below).

Tests 13 to 17 showed no sign of fatigue in Ti 15-3-3-3, but tests 18 and 19, which extended the same conditions to  $10^6$  cycles, showed small fatigue spots at the rib edge and above the rib.

In tests 20 to 23, the pressure conditions were unchanged but the material was changed to CP Ti(4). This material tended to fail in  $< 10^5$  cycles by starting to leak water slowly at a pinhole-like location.

In tests 24 to 27, Ti 3-2.5 was employed and survived  $10^5$  cycles in all cases, but did show a number of fatigue spots.

Altogether, of the 22 fatigue spots observed over all the tests, 16 were at the edge-of-rib position ( $\pm 0.02$  cm) and 6 were elsewhere above the rib. None was in the free-span location. This distribution correlates very well with the computed region of maximum stress (and maximum stress cycling) in this geometry.

For each of the static pressure and overpressure conditions listed in Tables 7 and 8, the stress distribution was computed, using the methods of

AD-A146 420

PULSED ELECTRIC DISCHARGE LASER TECHNOLOGY ELECTRON  
BEAM WINDOW FOIL MATE. (U) AVCO EVERETT RESEARCH LAB  
INC EVERETT MA M W MCGECH ET AL. JAN 84

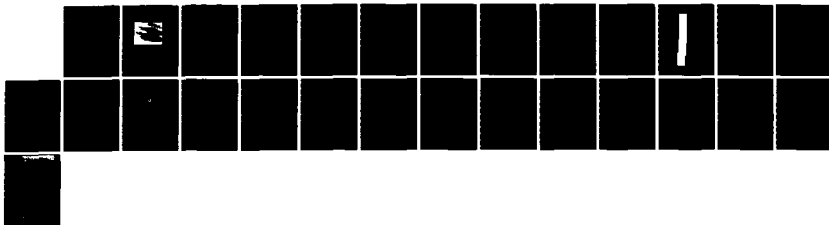
2/2

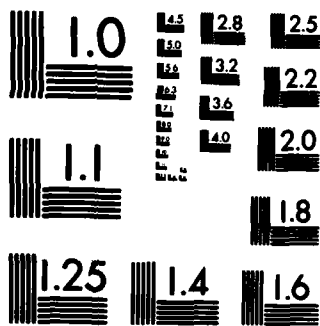
UNCLASSIFIED

DRSMI/RH-CR-84-13 DAAH01-82-D-A013

F/G 20/5

NL





COPY RESOLUTION TEST CHART



K9441

Figure 47. Position of the crack in Figure 46 relative to the rib edges, which show corrosion lines.

TABLE 8 CYCLIC PRESSURE TESTS ON 6:1 ELLIPSE, 0.5 cm SLOT, FRAME

Test No.	Static Pressure (psi)	Over-Pressure (psi)	Material	No. of Cycles	Failure Mode	Fatigue Spots e=edge of rib r=above rib
10	75	15	Ti 15-3-3-3 as rolled, 0.65 mil	$>10^7$	-	0
11	75	15	"	$>10^7$	-	0
12	75	15	"	$>8 \times 10^6$	-	0
13	90	22	"	$>10^5$	-	0
14	90	22	"	$>10^5$	-	0
15	90	22	"	$>10^5$	-	0
16	90	22	"	$>10^5$	-	0
17	90	22	"	$>10^5$	-	0
18	90	22	"	$>10^6$	-	2e
19	90	22	"	$>10^6$	-	3r, 1e
20	90	22	CP Ti(4) 0.5 mil	$3.7 \times 10^4$	pinhole	1r
21	90	22	"	$2.1 \times 10^4$	pinhole	1e
22	90	22	"	$5.9 \times 10^4$	pinhole	1e
23	90	22	"	$>10^5$	-	0
24	90	22	Ti 3-2.5, 0.6 mil	$>10^5$	-	1r, 1e
25	90	22	"	$>10^5$	-	0
26	90	22	"	$>10^5$	-	1e
27	90	22	"	$>10^5$	-	0

Section 3.0, for a 0.65 mil elastic foil of modulus  $15 \times 10^6$  psi. The results are shown in Figure 48, where the data is plotted as MEDIAN stress against ALTERNATING stress in a form of Goodman diagram. Here we define

$$\text{MEDIAN STRESS} = (\sigma_p + \sigma_{p+\Delta P})/2 \quad (10)$$

$$\text{ALTERNATING STRESS} = (\sigma_{p+\Delta P} - \sigma_p)/2 \quad (11)$$

in which  $\sigma_p$  and  $\sigma_{p+\Delta P}$  are the peak foil stresses, at pressures P and P+ $\Delta P$ , respectively. Also on Figure 48 is the measured uniaxial fatigue data (30 Hz, sinusoidal, A = 0.81,  $10^7$  cycles) from Section 2.0, and a linearly scaled biaxial strength curve.

In the calculation of the peak foil stresses, we have allowed for the factor of 2 enhancement in alternating stress because of foil ringing. As noted above, the foil typically rings for ~ 10 cycles at ~ 7 kHz. In a real situation, with gas-loading, the foil rings a similar number of cycles, but at ~ 50 kHz.

The test data taken at points A...E is listed in Tables 7 and 8. At point A, the Ti 15-3-3-3 as-rolled foil shows no fatigue spots at  $10^7$  cycles. The same is true of point D, although it has higher mean and alternating stresses. Point B had the two early failures, which have been discussed above in the context of possible corrosion. The other two runs at point B generated 1 fatigue spot in  $10^7$  cycles. At point C, there were four fatigue spots in  $10^7$  cycles whereas, in the longer runs for point E ( $10^6$  cycles), there were 6 fatigue spots. However the  $10^5$  cycle performance at point E was perfect.

Taken together, the data shows that  $10^7$  cycle foil life is achieved below the biaxial strength line but that fatigue spots are more frequent as the line is approached. Further data would be desirable in order to have statistical information for large area foil applications. Because the test conditions required to induce fatigue were about two times higher in stress than those anticipated at the outset of the program, testing has had to proceed at repetition rates reduced from these originally planned. As a result, in spite of more than 1,000 hr of continuous running (41, 24-hr days), the data is still much less plentiful than desired.

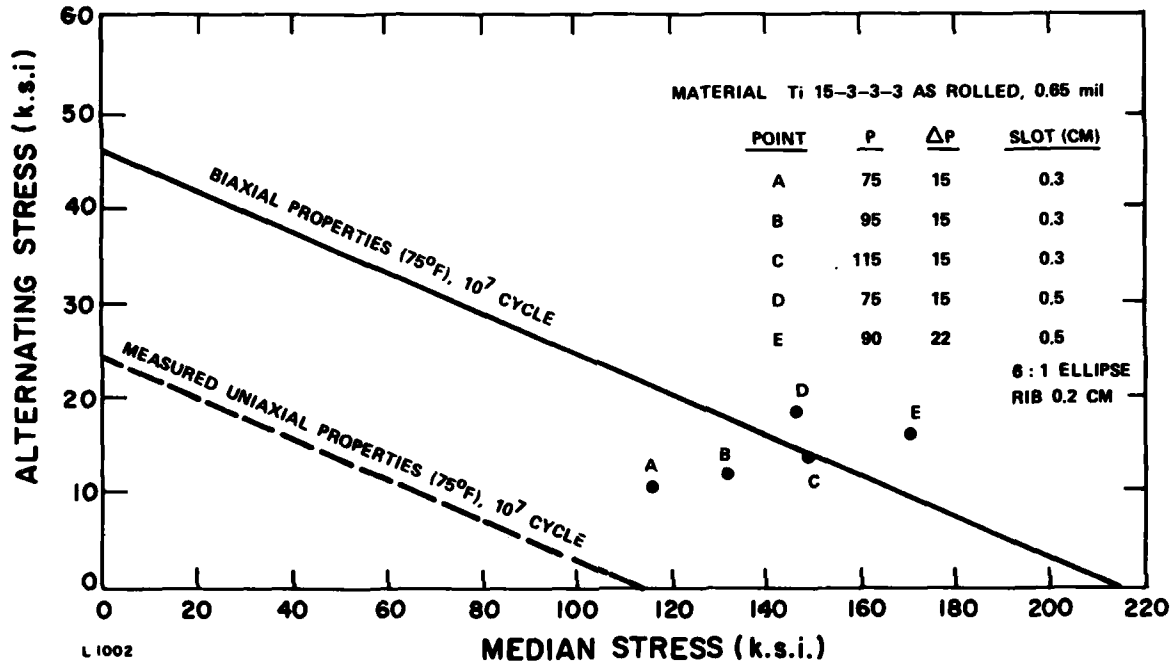


Figure 48. Goodman plot of test data on 0.65 mil, as-rolled Ti 15-3-3-3, showing the biaxial strength enhancement applied to measured properties.

When CP Ti(4) and Ti 3-2.5 were tested under the severe load conditions applying to point E, failures and fatigue spots were more common (Table 8), even at  $< 10^5$  cycles. This is not a direct comparison with Ti 15-3-3-3 because the CP Ti(4) was 0.55 mil thick, as opposed to 0.65 mil. However, this result, in combination with the burst test scatter for CP Ti(4), shows that it is a less uniform material than the as-rolled Ti 15-3-3-3.

Of six fatigue spots in Ti 15-3-3-3 given detailed examination, five showed evidence that abrasive dust particles had been between the rib and the foil. The sixth showed what appeared to be a small protrusion toward the rib, consisting of the same material as the foil, as verified by EDAX. This latter feature only showed one clearly developed fatigue crack, and was probably caused by a material defect.

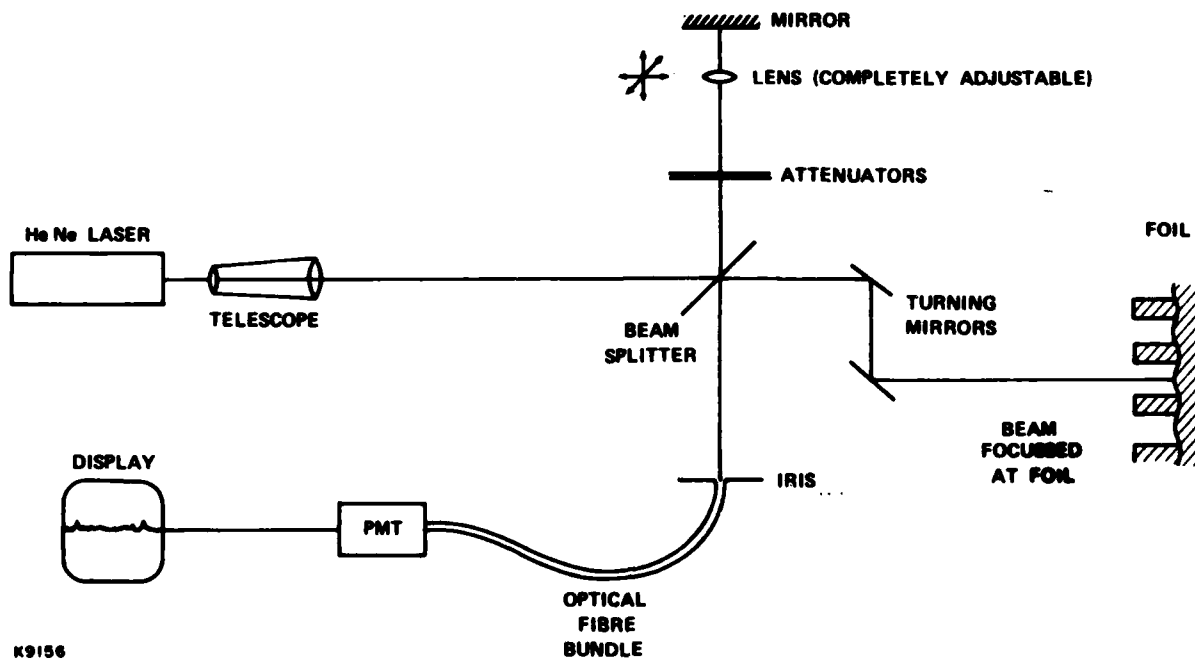
It is clear that in future work precautions will have to be taken to eliminate dust between the foil and the rib, beyond the solvent wash that was applied in the present work.

## 6.0 INTERFEROMETRIC MEASUREMENT OF FOIL MOVEMENT

A simple Michelson interferometer was used to measure foil movement on the test rig. Because the geometry employed was unusual, a description of this interferometer will be given. The requirement was to follow the foil motion - of amplitude up to  $100 \lambda$  at 633 nm - in real time. At the 7 kHz oscillation frequency of the test rig foils, the required fringe-counting rate was 1.5 MHz. In addition, it was desirable that no reflectors should be attached to the foil (which might affect the stress distribution) and that no special foil surface polishing should be required (which might affect foil mechanical properties, and which, in any case, would be time-consuming). The solution adopted was to use a single speckle in the reflected pattern from a focused laser beam as the reference signal for the interferometer. This is illustrated in the schematic of Figure 49.

Typically, the output from a He-Ne alignment laser was expanded 10x in a telescope and focused on the foil at a distance of  $\sim 80$  cm. The spot size was estimated to be about  $50 \mu\text{m}$ . Reflected from the convex foil surface was a speckle pattern that consisted of about  $10^3$  speckles in a cone of  $\sim 10^{-2}$  sterad. The number of speckles was minimized by adjusting the telescope finely so that the focused beam waist coincided with the foil surface. Part of the beam was split off and reflected from a reference mirror and lens combination (Figure 49). Adjustment of the position of this lens, both in the plane of the mirror and normal to it, allowed the reference beam to be given the correct radius of curvature and tilt for interference with one of the speckles. A single speckle was selected by means of an adjustable iris, behind which was a light guide leading to a photomultiplier.

The adjustable lens was an essential element of the system. It gave the reference arm a geometric length equal to that of the signal arm when the reference beam was exactly focussed on the mirror. A plane mirror was used, whereas the foil was a curved, cylindrical surface of radius  $\sim 3$  cm. Small lens adjustments were needed in order to match the curvature and tilt of the



K9156

Figure 49. Schematic of interferometer.

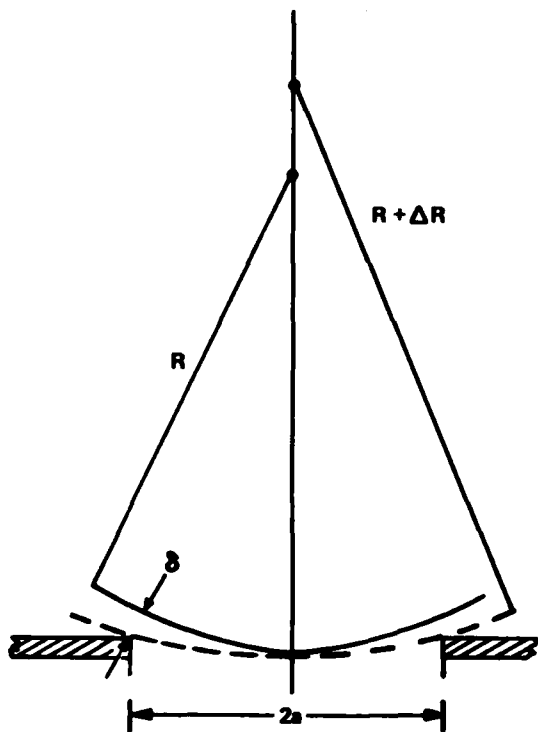
reflected speckle. The sensitivity of the curvature and tilt matching is illustrated in Figure 50, where their dependence on the detection aperture (2a) is given. In the example given, the radius must match to within  $\pm 3$  cm and the tilt to within  $0.6 \times 10^{-4}$  rad.

In setting up the interferometer, a large speckle is chosen and the reference beam intensity is adjusted to be similar to that of the speckle by the insertion of ND filters. The lens adjustments are then made while the detector output is being monitored on an oscilloscope. When the curvature match is obtained, there is a sudden increase in signal fluctuation, and a regular pattern may be observed on the screen if the foil is being mechanically driven and the oscilloscope is synchronously triggered. In order to increase the frequency response of our interferometer, an emitter follower circuit was built which had a current gain of  $\sim 10^3$  and response to  $\sim 2$  MHz.

The full time-dependent foil movement could be recorded over an extended number of cycles by recording successively delayed sweeps of the oscilloscope trace. Figure 51 is a montage of such photographs, being the first quarter cycle of a series of about 14 oscillations of the foil. The turning points of foil motion can be easily seen as reductions in the fringe frequency. Each fringe represents  $\lambda/2$  motion of the foil. Continued measurements at larger delays allowed the movement (Figure 43) to be plotted, and similar measurements were made in the analysis of the test rig performance described in Section 5.0.

In conclusion, a useful technique has been developed for the remote sensing of the movement of quasi-smooth surfaces. The typical surface appearance of these foils may be seen under S.E.M. as, for example, in Figure 45. The roughness horizontal scale is  $\sim 3 \mu\text{m}$ , which explains the large number of speckles obtained from a  $50 \mu\text{m}$  focal spot.

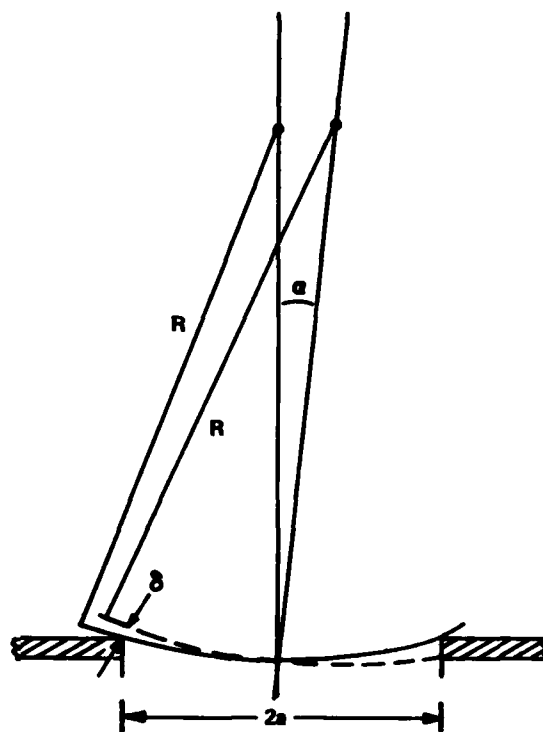
As one of the tests on the cyclic pressure rig the movement of the foil support frame was measured. No difficulty was experienced in performing interferometry off its machined stainless steel surface. The cyclic movement of the frame was  $\sim 2 \lambda$  under load conditions of 90 psi static with 15 psi pulsed overpressure.



(a) MATCHING RADIUS

$$\text{FOR } \delta = \frac{\lambda}{10}, \Delta R \doteq \frac{\lambda R^2}{5a^2}$$

E.G.  $R = 50 \text{ cm}$ ;  $a = 0.1 \text{ cm}$ ;  $\lambda = 632.8 \text{ nm}$   
 $\Rightarrow \Delta R = 3.1 \text{ cm}$



(b) MATCHING INCLINATION

$$\text{FOR } \delta = \frac{\lambda}{10}, \alpha \doteq \frac{\lambda}{10a}$$

E.G.  $\lambda = 632.8 \text{ nm}$ ;  $a = 0.1 \text{ cm}$   
 $\alpha = 0.63 \times 10^{-4} \text{ rad}$

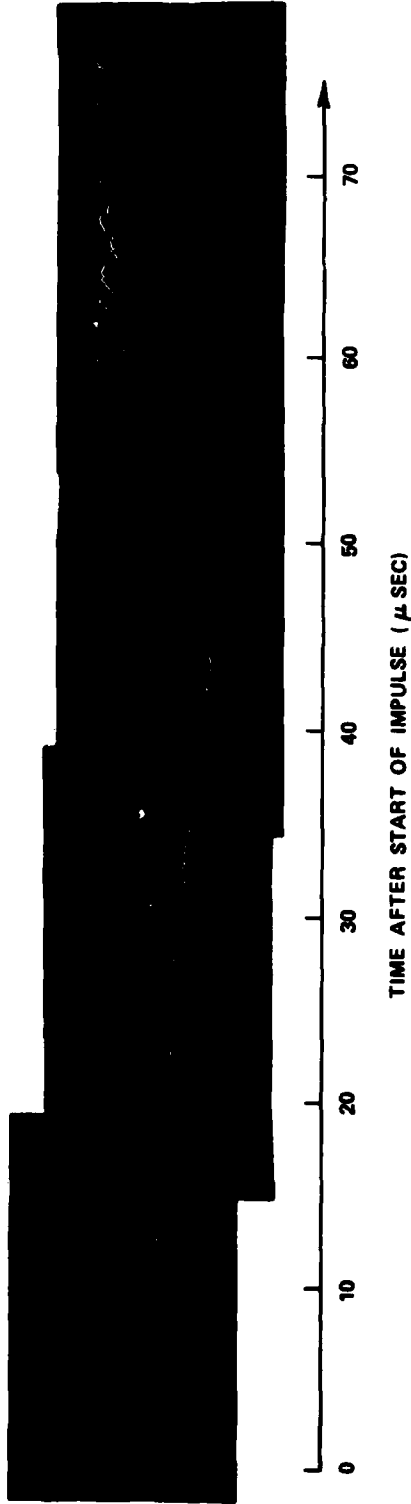
L2279

Figure 50. Illustration of curvature and tilt matching in the interferometer.

POSIT                      TERFEROMETRY, TEST RIG

WAVELENGTH 0.63  $\mu$  m, 2  $\mu$  sec / div,

0.6 MIL Ti FOIL, STATIC PRESSURE 75 PSI, 0.2 cm RIB, 0.5 cm SLOT, 6 : 1 ELLIPSE



K9454

Figure 51. Initial part of interferometer output used to plot Figure 43, showing the first quarter cycle.

## 7.0 SINGLE PULSE MEASUREMENT OF FOIL MOTION

### 7.1 INTRODUCTION

As a verification of the simulated laser pressure conditions used in Section 5.0, a measurement was performed of foil deflection in a real laser situation. For this purpose, an electron-beam-pumped laser was modified so that foil movements could be measured by interferometry from the vacuum side of the foil, and the cavity side was partly filled to avoid spurious acoustic reflections.

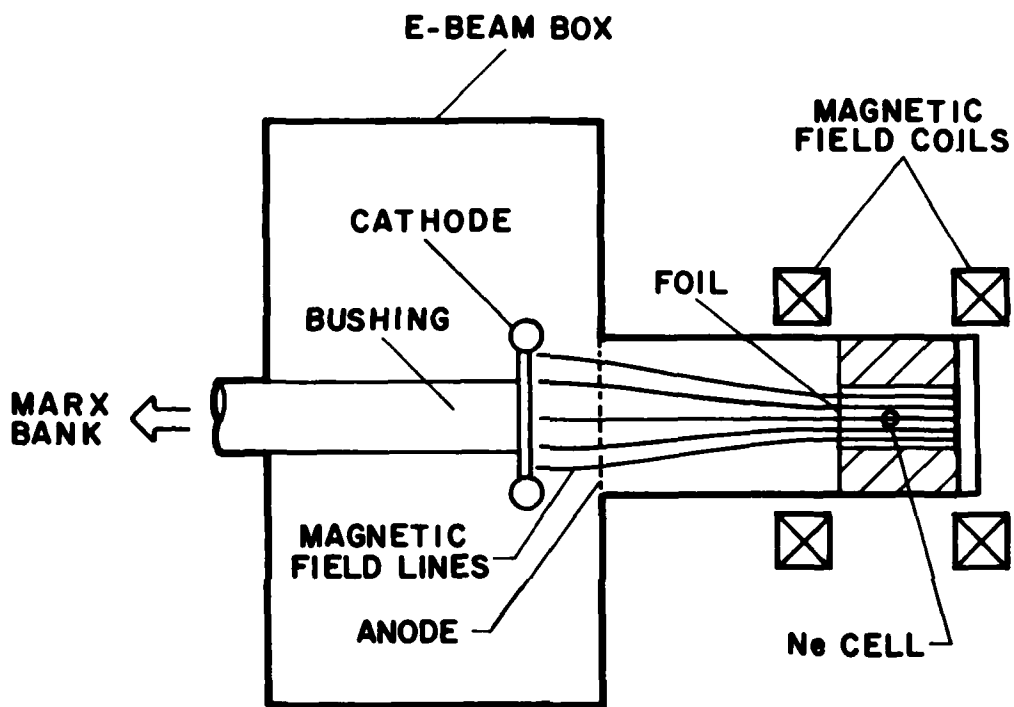
### 7.2 EXPERIMENTAL ARRANGEMENT

An electron-gun was used which had the following measured parameters:

Voltage	275 kV
Current density (before foil)	11 A cm <sup>-2</sup>
Magnetic guide field	1 kG
Pulse duration	0.6 μsec > 1.2 μsec
Total available foil aperture	4 x 100 cm
Foil aperture used	4 x 15 cm

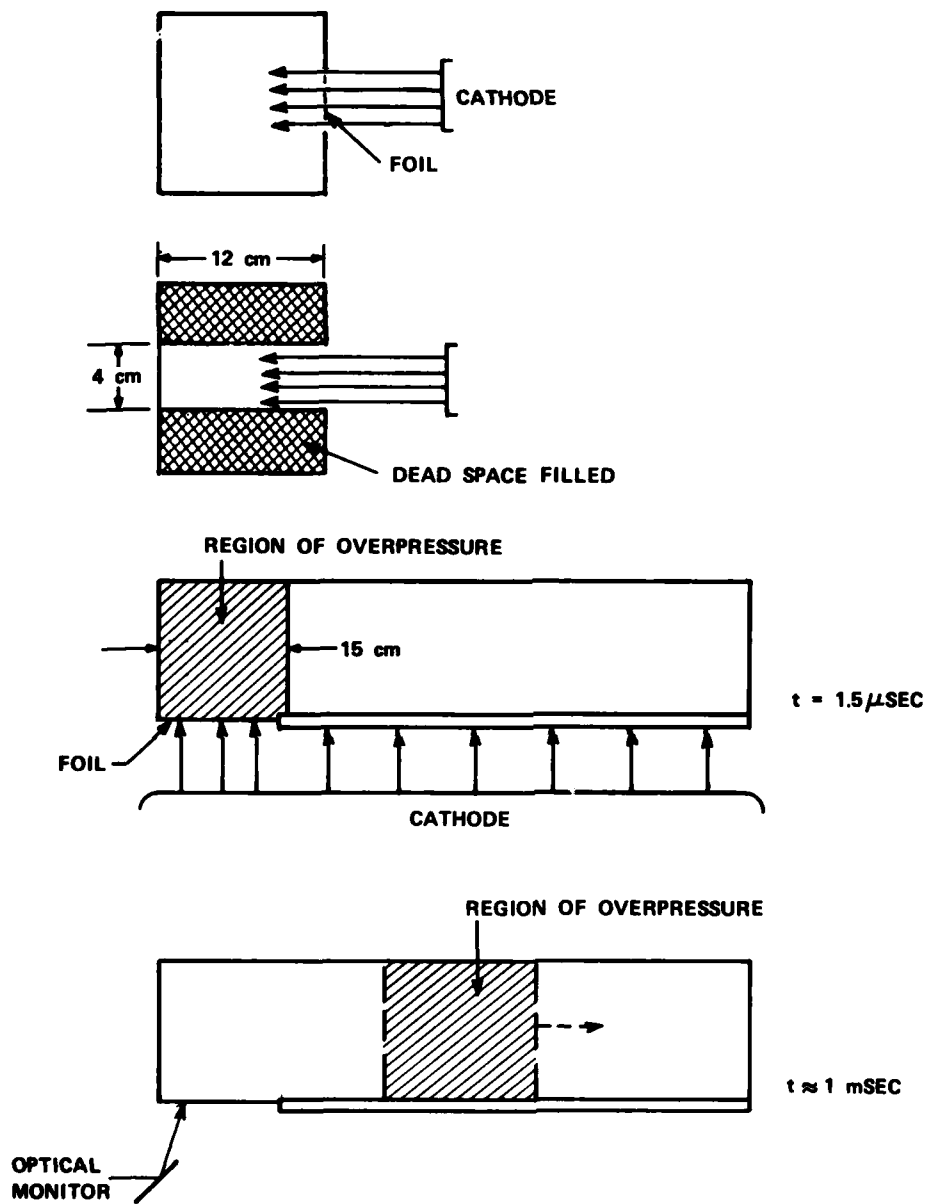
The gun is shown schematically in Figure 52. In order to create an overpressure time history characteristic of a laser with an aperture of 30 cm, the electron beam was restricted to an aperture of 4 x 15 cm as shown in Figure 53. In the 4 x 15 cm aperture was a foil support structure with rib 0.2 cm, slot 0.3 cm and rib contour 6:1 ellipse. After the foil, the electron beam entered a gas, which was either Ar or Ne, inside a cell of propagation depth 12 cm. Within the cell the electrons deposited their energy in a volume 4 x 15 x 12 cm deep volume, whose boundaries were defined by an aluminum block that filled the dead spaces above and below the beam and at one end of the cavity. The overpressure was allowed to form an expansion wave down the body of the cavity.

Foil movement was monitored by the interferometer described in Section 6.0 above, modified optically to allow access to the vacuum side of the foil.



H 7883

Figure 52. Schematic of electron gun used in single pulse experiment.



K7797

Figure 53. Illustration of single pulse pumping geometry, showing blocked regions.

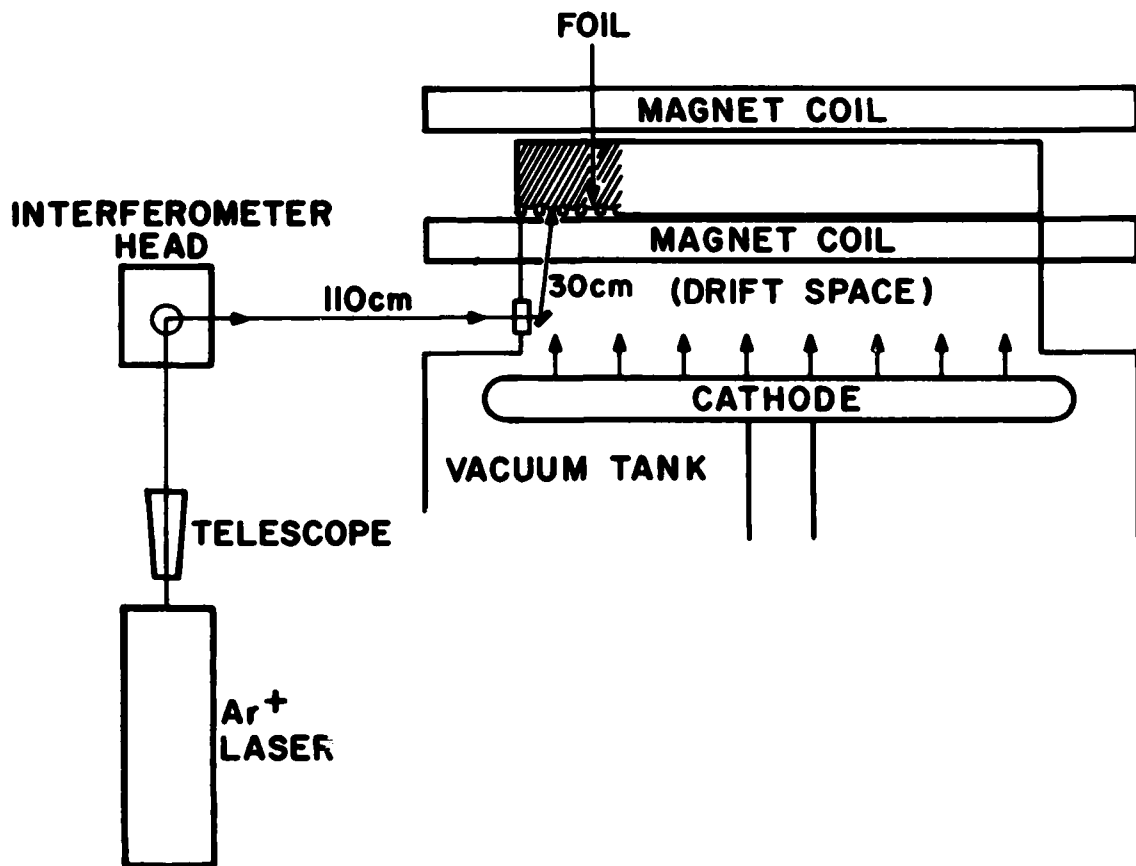
The optical arrangement is shown in Figure 54. Because the magnet coils and drift space required an extension of the interferometer signal arm to ~ 140 cm, increased laser intensity was required to compensate for the reduced intensity of the speckle pattern (~ 10 times reduced because of the additional length). An argon ion laser was employed, capable of 1-W output on the stronger lines. It was found, however, that the ion laser had to be operated just above threshold, at ~ 100 mW, in order to obtain the coherence length of ~ 300 cm, which was necessitated by the long signal arm. Alignment of the interferometer was straightforward and greatly helped by the presence of low-frequency (< 1 kHz) room vibrations, which gave strong signals once the curvature and angle matching were achieved.

### 7.3 MEASUREMENTS OF FOIL MOVEMENT

By variation of the electron gun pulse duration, the overpressure was varied at constant gas fill pressure. In order to have the most direct relevance to laser applications, most of our data was taken with a gas fill of 75 psi Ne. Although we also took data with 30 psi Ar, the fringe count rate for that case exceeded the interferometer bandwidth, and the resulting poor signal-to-noise ratio made the interpretation of foil oscillatory motion difficult.

Unlike the data obtained on the cyclic test stand, the foil motion on the electron gun could not readily be deciphered during the first few half cycles following the current pulse of the gun. It was realized that the direct heating of the foil by the passage of electrons was contributing a substantial movement of the foil because of thermal expansion. It is possible that the readjustment of the foil to its new thermal equilibrium was leading to higher-order membrane modes being excited, which confused the interferometer signal. An estimate of the expansion effect will be given below in Section 7.4.

In the case of Ne at 75 psi, the foil oscillatory motion could be resolved after a delay of about 10  $\mu$ sec from the gun pulse. The period of oscillation was 21  $\mu$ sec, somewhat longer than the approximate estimate of 15  $\mu$ sec for a gas-loaded foil given in Section 3.5. This discrepancy could be



L2700

Figure 54. Optical path layout for single pulse experiment.

caused by either an underestimate of the effect of the mass of the gas moved by the foil, or a lower membrane stress than the computed one due to a small degree of foil slippage at the edge of the foil support frame.

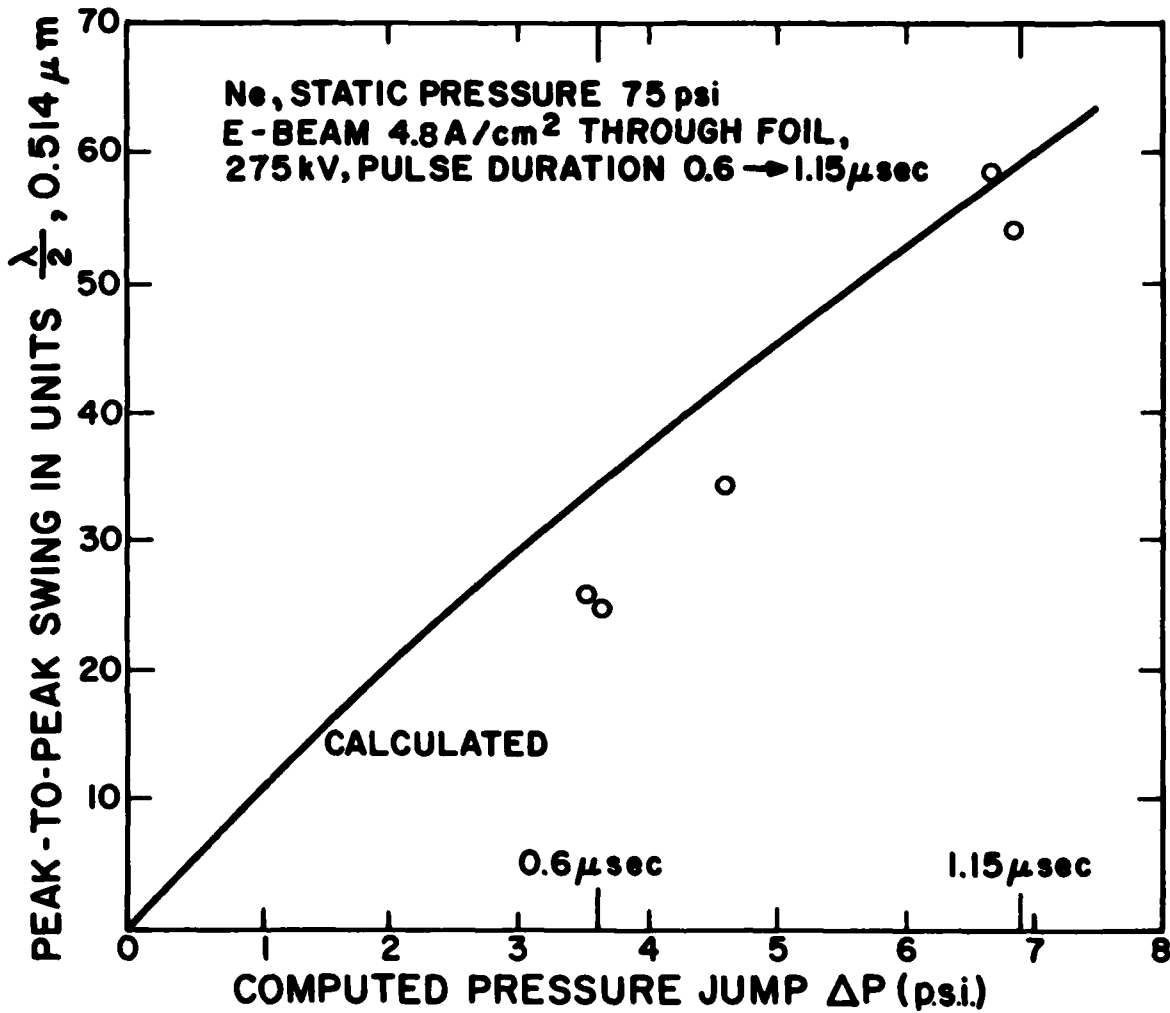
The measured amplitudes of oscillation are plotted in Figure 55, for a range of electron gun pulse durations. Also in that figure is the calculated foil movement for those experimental conditions. The test foil for this data was 0.5 mil CP Ti(4), chosen because it had the shiniest surface and hence gave the best interferometer signal-to-noise ratio. The calculation will be discussed in the following section.

An interesting additional observation was made in both the Ar and Ne cases. The foil had a constant low amplitude oscillation, which we refer to as the background oscillation, present even when the gun was not fired. The peak-to-peak amplitude of this background oscillation was between  $10\lambda/2$  and  $18\lambda/2$  in each gas and its period was 21  $\mu$ sec. Presumably this oscillation was being excited by harmonics of room vibrations, although it was still present when the rotary pumps to the vacuum chamber and laser cell were switched off. Possibly a chance coincidence existed between the foil period and one of the gas cell acoustic modes. During the experiment we did not use any acoustic absorbers in the gas cell, reasoning that our measurement would be over before any reflected acoustic waves could return from the far end of the gas cell.

#### 7.4 CALCULATION OF FOIL MOVEMENT

We consider first the thermal expansion of the foil in response to heating of the foil material by the electron beam. At 275 kV incident energy the electrons lose on average 22 kV passing through a 0.5 mil Ti foil. Although the average current after the foil is 4.8 A/cm<sup>2</sup>, the actual current density that impinges on  $\sim 0.22$  cm out of the 0.3 cm free aperture is 11 A/cm<sup>2</sup>. When a calculation is performed, we find that the foil expansion factor, averaged over the free span, is  $4.6 \times 10^{-4}/1 \mu$ sec of electron beam pulse, corresponding to a temperature rise of 80°C at the foil midspan position.

In order to compute the pressure jump, an existing AERL code was used to calculate electron-beam deposition as a function of depth into the gas. The average deposition for 75 psi of Ne was 0.061 J/cm<sup>3</sup> per  $\mu$ sec, leading to a



L2707

Figure 55. Measured and calculated foil peak-to-peak movement for 75 p.s.f. Ne single pulse experiment.

pressure jump ratio  $\Delta P/P=0.081/1 \mu\text{sec}$ , of the electron beam pulse. From Figure 25, we may read the deflection computed for each pressure jump condition, taking into account the 2x overshoot for transient loading (Section 3.5) and doubling to obtain the peak-to-peak motion. The results are plotted as a line in Figure 55. The accuracy of this calculation, involving so many steps, cannot be better than  $\pm 20$  percent. However, it is in good agreement with the measured movement and hence serves to verify the amplitudes used in the cyclic tests of Section 5 (which corresponded to larger overpressures).

The thermal expansion factor of  $4.6 \times 10^{-4}/1 \mu\text{sec}$  pulse leads to an initial foil movement 31 percent as great as the peak-to-peak oscillation, for the 75 psi Ne case. It is, therefore, not surprising that the initial movement of the foil is irregular, as described above. Although this thermal expansion is not included in the simulation of Section 5.0, it does not contribute nearly as much to the stresses as the pressure pulse; hence, its neglect is not a serious matter.

#### 7.5 CONCLUSION

Although a good measurement of single pulse foil movement was only obtained in the case of the Ne gas fill, the result was encouragingly in line with expectation, and thereby confirmation was made of the applicability of the cyclic test results to real laser stress-cycling conditions.

## 8.0 SUMMARY

The following comments may be made regarding the data presented in the previous sections of this report:

1. The tensile strength measurements performed on Ti alloy ribbon showed that foil samples were as strong as or stronger than the bulk material in all cases (Section 2.2, Table 6).
2. The  $10^7$  cycle fatigue test on ribbon samples showed trends similar to those observed in bulk Ti. However, there was a large decrease in the  $10^7$  cycle fatigue strength of aged Ti 15-3-3-3 tested at 600°F, relative to 75°F. Such a decrease was not observed in Ti 3-2.5 (Table 4). This data underscores the fact that Ti 15-3-3-3 is an outstanding low temperature alloy, but that at temperatures much above 600°F in fatigue it is probably not much better than Ti 3-2.5. Further data is needed on this important point.
3. The crystal structures revealed in scanning electron microscopy show that there is not a direct relationship between the size of the crystal grains (relative to foil thickness) and the foil strength (Section 2.4).
4. An experimental measurement of the membrane strength of Ti alloy foils (Section 4.0) showed that their strength under biaxial stress loading was much greater than the uniaxial strength measured on ribbon samples. The largest enhancement factor, 1.89, was obtained for Ti 15-3-3-3 (as rolled). The causes of this enhancement are not known.
5. In the cyclic pressure impulse tests (Section 5.4) the fatigue performance of foils could be correlated quite well with the measured uniaxial fatigue properties scaled up by the measured biaxial strength enhancement factor. The fatigue stress waveforms were different in each case, with the cyclic pressure pulse including much higher frequencies (7 kHz as opposed to 30 Hz). However, we recommend the use of scaled 30 Hz fatigue data as a safe design basis.

6. In a number of the higher pressure pulsed tests we observed small fatigue "spots" above the foil support rib. These spots, when examined under the scanning electron microscope with EDACS analysis, turned out to be areas of fatigue crack growth on the pressure (higher stress) side, directly opposite to small alumina particles embedded in the foil on the rib side. The value of clean-room preparation of foil assemblies is emphasized, particularly when the calculated stresses approach the fatigue limit.
7. The single-pulse measurement of foil movement gave foil oscillation amplitudes in good agreement with those calculated (for Ne at 75 psi). This result confirmed the correctness of the test conditions in Section 5.0, where the overpressure was deduced only from the measured motion of the foil.
8. A finite-element computational model of the foil was developed which allowed stresses and strains to be calculated from arbitrary input material properties. Because of the enhanced yield strength under biaxial loading conditions, most of the calculations were performed for an assumed elastic Ti material. The extension to specific measured material properties was only carried out in the modeling of the membrane strength test for Ti 3-2.5, in connection with a determination of its biaxial strength enhancement factor.
9. The model was used to predict the actual stresses in the pressure cycling experiment, and also to optimize the rib support shapes. Out of the generic class of elliptical support shapes stress minima were demonstrated for ellipticity of 8:1 (minor axis perpendicular to foil). An additional finding with the computer model of a plastically deforming foil showed that "pre-forming" could reduce the foil peak stress (section 3.4) by useful amounts, although the practical scope for this is limited by low foil ductility.
10. A useful interferometer design was devised for the measurement of foil movement at velocities up to  $200 \text{ cm sec}^{-1}$  (Section 6.0). The foil surface required no preparation, as the reflected speckle pattern could be used for the signal beam. The same principle is of general applicability in the remote measurement of vibrations where a quasi-smooth surface is available.

11. Future work is necessary on the uniformity of large foil samples, particularly in relation to material defects. In the burst test data of Section 4.0 the as-rolled Ti 15-3-3-3 exhibited much less scatter than any other foil type, indicating that its properties are extremely uniform over areas of hundreds of square centimeters. This could be a consequence of its superb cold-rolling properties. Further work is desirable on the quality of large area ( $> 10^4 \text{ cm}^2$ ) samples of Ti 15-3-3-3.

DISTRIBUTION

	<u>Number of Copies</u>
Director Defense Advanced Research Projects Agency ATTN: Directed Energy Office (Dr. J. Mangano) Directed Energy Office (LTC R. Benedict) 1400 Wilson Boulevard Arlington, VA 22209	1 1
Director OUSDRE (R&AT) ATTN: Directed Energy Office The Pentagon Washington, DC 20301	1
Commander Headquarters AFSC (DLCAM) ATTN: CPT T. J. Dyble Andrews AFB Washington, DC 20334	1
Commander AF Wright Aeronautical Laboratories Aero Propulsion Laboratory ATTN: POOC-3 (D. A. Garscadden) Wright-Patterson AFB, OH 45433	1
Commander Air Force Weapons Laboratory ATTN: AR (COL John G. Rich) AL (Dr. L. A. Schlie) ARAY (Mr. J. O'Loughlin) Kirtland AFB, NM 87117	1 1 1
Commander Air Force Space Division ATTN: YND (COL H. A. Shelton) P.O. Box 92960 Worldway Postal Center Los Angeles, CA 90009	1
Commander US Army Electronics and Devices Laboratory ATTN: DELET-BG (Mr. Wright) Fort Monmouth, NJ 07703	1
Commander Ballistic Missile Defense Advanced Technology Center ATTN: BMDATC-O (Mr. Lavan) P.O. Box 1500 Huntsville, AL 35807	1

DISTRIBUTION - Continued

	<u>Number of Copies</u>
Director Central Intelligence Agency ATTN: Mr. Grey Bock Washington, DC 20505	1
Director Defense Intelligence Agency ATTN: Mr. Seymour Berler Washington, DC 20301	1
Director Department of Energy ATTN: DP23 (Dr. Richard Schriever) Washington, DC 20545	1
Commander Naval Research Laboratory ATTN: Code 112 (Dr. N. Djeu) Code 112 (Dr. S. Searles) Washington, DC 20375	1 1
Commander Office of Naval Research ATTN: Code 402 (Dr. R. Behringer) 1030 E. Green Street Pasadena, CA 91106	1
Commander Naval Sea Systems Command Department of the Navy ATTN: PMS-405 (CPT A. Skolnick) Washington, DC 20362	1
Commander Naval Ocean Systems Center ATTN: Code 8113 (Mr. G. Beagler) 271 Catalina Boulevard San Diego, CA 92152	1
Aerospace Corporation ATTN: Dr. R. Hoffland P.O. Box 92957 Los Angeles, CA 90009	1
AVCO Everett Research Laboratories ATTN: Dr. J. Daugherty 2385 Revere Beach Parkway Everett, MA 02149	1

DISTRIBUTION - Continued

	<u>Number of Copies</u>
Beta Development Corporation ATTN: Mr. Gary Loda 6557 Sierra Lane Dublin, CA 94556	1
The Boeing Company ATTN: Mr. Weisbach P.O. Box 3999, M.S. 8C16 Seattle, WA 98124	1
Hughes Aircraft Company ATTN: R. Hill Centinela and Teale Streets Culver City, CA 90230	1
Lawrence Livermore National Laboratory ATTN: Code L470 (Dr. J. R. Murray) Code L470 (Dr. L. Pleasance) P.O. Box 5508 Livermore, CA 94550	1 1
Los Alamos National Laboratory ATTN: Dr. C. Fenstermacher (M.S. 527) Dr. W. Leland (M.S. 532) P.O. Box 1663 Los Alamos, NM 87545	1 1
Mathematical Sciences Northwest, Inc. ATTN: Dr. Peter H. Rose P.O. Box 1887 Bellevue, WA 98009	1
Maxwell Laboratories, Inc. ATTN: Dr. A Kolb 8835 Balboa Avenue San Diego, CA 92123	1
Northrop Corporation Research and Technology Center ATTN: Dr. M. Baumik One Research Park Palos Verdes Peninsula, CA 90274	1
Physics International Company ATTN: Dr. M. Kolpin 2700 Merced Street San Leandro, CA 94577	1

DISTRIBUTION - Continued

	<u>Number of Copies</u>
Poseidon Research ATTN: Dr. S. Crow 11777 San Vincente Boulevard Los Angeles, CA 90049	1
R&D Associates ATTN: Dr. J. Colbert 6400 Uptown Boulevard, NE Albuquerque, NM 87110	1
R&D Associates ATTN: Dr. Dominick Conte 301A S. West Street Alexandria, VA 22314	1
Riverside Research Institute ATTN: Space Laser Library 1701 North Fort Myer Drive Arlington, VA 22209	1
Rockwell International Rocketdyne Division ATTN: Mr. Richard Johnson 6633 Canoga Avenue Canoga Park, CA 91304	1
Sandia Laboratories ATTN: J. Gerado P.O. Box 5800 Albuquerque, NM 87115	1
W. J. Schafer Associates, Inc. ATTN: Dr. J. Reilly 607 N. Avenue, Door 14 Wakefield, MA 01880	1
W. J. Schafer Associated, Inc. ATTN: Dr. T. Norwood 1901 North Fort Myer Drive, Suite 803 Arlington, VA 22209	1
Stanford Research Institute ATTN: Dr. D. Huestis Menlo Park, CA 94025	1
GTE Sylvania, Inc. Electronic Systems Group - Western Division ATTN: Dr. S. Guch P.O. Box 188 Mountain View, CA 92042	1

DISTRIBUTION - Continued

	<u>Number of Copies</u>
TRW Defense and Space Systems Group ATTN: Mr. R. Foster 2030 M. Street NW, Suite 800 Washington, DC 20036	1
TRW Defense and Space Systems Group ATTN: Mr. R. Aprahamian Building R1, Room 1196 One Space Park Redondo Beach, CA 90278	1
United Technologies Research Center ATTN: Dr. W. Brown 400 Main Street East Hartford, CT 06108	1
Western Research Corporation ATTN: Mr. R. Hunter 8616 Commerce Avenue San Diego, CA 92121	1
Department of Electrical Engineering State University of New York at Buffalo ATTN: Dr. W. J. Sarjeant 4232 Ridge Lea Road Amherst, NY 14226	1
Defense Technical Information Center Cameron Station Alexandria, Va 22314	1
US Army Materiel System Analysis Acitivity ATTN: DRXSY-MP Aberdeen Proving Ground, MD 21005	1
DPSMI-R (Dr. McCorkle)	1
-R (Dr. Roahdes)	1
-RHA (Ms. J. Hancock)	10
-RHS (Dr. G. Dezenberg)	1
-RHS (Dr. J. C. Walters)	1
-RAS (Dr. Frank Haak)	1
-LP (Mr. Voigt)	1
-RPR	1
-RPT (Record Copy)	1

END

FILMED

1-84

DTIC